INVESTIGATION OF THE ENVIRONMENTAL INFLUENCES RELATED TO THE PRECIPITATION STRUCTURE OF SUPERCELL THUNDERSTORMS AND THEIR EVOLUTION

by

Richard Sirico

A thesis submitted to the faculty of
The University of North Carolina at Charlotte
in partial fulfillment of the requirements
for the degree of Master of Science in
Earth Science

Charlotte

2020

Approved by:

_____
Dr. Casey Davenport

_____
Dr. Matthew Eastin

_____
Mr. Terry Shirley

©2020
Richard Sirico
ALL RIGHTS RESERVED

ABSTRACT

RICHARD SIRICO. Investigation of the environmental influences related to the precipitation structure of supercell thunderstorms and their evolution. (Under the direction of DR. CASEY DAVENPORT)

The precipitation structure of supercell thunderstorms (e.g., low-precipitation (LP), classic (CL), high-precipitation (HP)) has been associated with differing severe weather threats (wind, hail, or tornadoes) to the public, thus motivating work examining the causes for these supercell categories. Previous research has demonstrated that the precipitation structure of these storms is impacted by both the kinematic and thermodynamic profiles within their inflow environments; in particular, it has been hypothesized via analysis of a set of observed supercells across the precipitation spectrum that the upper-level wind profile is of paramount importance, due to the ability of these winds to transport hydrometeors close to (i.e., weak winds leading to HP) or farther away (i.e., strong winds leading to LP) from the updraft (Rasmussen and Straka 1998). However, a recent idealized modeling study conducted by Warren et al. (2017) has found the opposite association, which suggests additional investigation is necessary.

The present study uses an automated tracking algorithm to identify and classify 104 supercell thunderstorms into either LP/CL or HP categories; 66 were identified as LP/CL and 38 as HP. Model-derived soundings were then used to describe the inflow environments of these storms throughout their lifetimes. Distributions of numerous thermodynamic and kinematic parameters were created to compare the two dominant supercell categories using statistical significance tests. Following these statistical

comparisons, it was clear that a number of differences were present between LP/CL and HP environments. In particular, the kinematic profiles of LP/CL supercells tended to contain stronger bulk shear, storm-relative helicity, and stronger upper-level winds compared to HP supercells, consistent with the prior observational study of Rasmussen and Straka (1998). However, the LP/CL wind profiles also contained veering winds aloft, which did provide consistency with Warren et al. (2017). Along with these kinematic differences, variations in the thermodynamic profile also proved to be important; HP storms exhibited significantly higher lifted condensation level (LCL) and level of free convection (LFC) heights, in addition to lower convective available potential energy (CAPE).

Many of the key inflow environmental differences could be tied to the synoptic set-up for each of the given precipitation modes. Notably, LP/CL storms often find themselves in much stronger synoptically forced environments, evident at multiple levels in the atmosphere (e.g., jet-level [300 hPa], 500 hPa, surface). Overall, the broader consistency of the present study with other prior observational studies, as opposed to the recent modeling studies, suggests that additional work is still needed to better understand the interplay of variations in kinematic and thermodynamic profiles in producing varying precipitation structures within supercells.

ACKNOWLEDGEMENTS

I would like to say thank you to Dr. Casey Davenport for not only motivating me to work to my full potential, but also in guiding me seamlessly through my research in what has become a very interesting piece of work that I am extremely proud of. A special thanks to the rest of my committee, Dr. Matthew Eastin and Mr. Terry Shirley for working with me through my crazy schedule between work and school. To everyone in the meteorology office space, I would like to thank each and every one of you for making me a more well-rounded meteorologist and for giving me the breaks I needed from my crazy life, especially during our lunch hour (or two). I would like to specially recognize Matt Gropp, thanks for both your help with coding and other severe weather expertise. Finally, I would like to thank my family for being there every step of the way with your love and emotional support that I needed.

TABLE OF CONTENTS

LIST OF TABLES viii

LIST OF FIGURES ix

CHAPTER I: INTRODUCTION 1

CHAPTER II: BACKGROUND. 4

a) Supercell Structure and Dynamics 4

b) The Supercell Spectrum 8

i) CL Characteristics 8

ii) LP Characteristics 9

iii) HP Characteristics 13

c) Modeling Studies 14

i) Kinematic 14

ii) Thermodynamic 15

d) Semi-Objective Storm Tracking 17

e) Concluding Remarks and Hypothesis 20

CHAPTER III: DATA AND METHODS 42

a) Datasets 43

i) Severe Storm Reports 43

ii) Radar Data 44

iii) Model Data 46

iv) Reanalysis Data 47

b) Methods 48

i) Cell Tracking 48

ii) Objective Identification of Precipitation Mode 50

iii) Tracking Algorithm Sensitivity Testing 53

iv) Sounding Acquisition 54

v) Synoptic Environment 56

CHAPTER IV: RESULTS AND DISCUSSIONS 67

a) Comparing Tracking Algorithms 67

b) Climatology 70

c) Inflow Environment Comparisons 72

i) Thermodynamic Comparisons 73

ii) Kinematic Comparisons 76

d) Sensitivity Testing 81

e) Summary 82

CHAPTER V: SUMMARY AND FUTURE WORK 111

a) Synoptic Environment and Climatology 111

b) Thermodynamic Comparisons 112

c) Kinematic Comparisons 114

d) Future Work 117

REFERENCES 119

LIST OF TABLES

TABLE 1: List of a few significant and insignificant variables related to LP storms and other supercell storms, namely CL/HP. The parameters with an asterisk denote significance at the 95% confidence level. Adapted from Bluestein and Parks (1983). 41

TABLE 2: An idealized representation of a case where one cell was identified as having more than one mesocyclone. 66

LIST OF FIGURES

FIGURE 1: A schematic of a supercell's reflectivity at three different levels, adopted from Browning (1964). 22

FIGURE 2: A schematic diagram of the updraft and downdraft structure of a supercell. Adopted from Lemon and Doswell (1979). 23

FIGURE 3: A schematic diagram representing the flow into, out of and around a supercell. Adopted from Lemon and Doswell (1979). 24

FIGURE 4: Simplified depiction of the lifting of streamwise (b) and crosswise (a) vorticity along an isentropic surface. Adapted from Davies-Jones (1984). 25

FIGURE 5: A schematic diagram that depicts the splitting of one cell into right and left moving cells in a westerly sheared environment. Adapted from Klemp (1987). 26

FIGURE 6: A schematic diagram representing the vertical pressure gradient force that is created in a vertically sheared environment where the winds veer with height. Adopted from the Markowski and Richardson (2014) Mesoscale Meteorology Textbook. 27

FIGURE 7: Low-level radar depiction of a CL supercell overlaid on the cloud features associated with the storm. The updraft region is also labeled. Adopted from Doswell and Burgess (1993). 28

FIGURE 8: Same as in figure 7, but for the LP supercell. Adopted from Doswell and Burgess (1993). 29

FIGURE 9: Same as in figure 7, but for the HP supercell. Adopted from Doswell and Burgess (1993). 30

FIGURE 10: Updraft profiles for a pre-split (a), more LP like supercell and a post-split (b), more HP-like supercell. Adapted from Bluestein and Woodall (1990). 31

FIGURE 11: Storm relative flow for LP, CL and HP storms ranging from top to bottom, respectively. Adapted from Rasmussen and Straka (1998). 32

FIGURE 12: The shear magnitudes for each of the precipitation modes, with the black, gray and white bars representing HP, CL and LP storms respectively. Adapted from Rasmussen and Straka (1998). 33

FIGURE 13: Composite hodographs for LP, CL and HP cases. The hodographs were rotated to the 0-4km bulk shear vector such that it is pointing in the positive x-direction. Adapted from Rasmussen and Straka (1998). 34

FIGURE 14: Different wind profiles that were testing in the Warren et al. 2017 modeling study. Adopted from Warren et al. (2017). 35

FIGURE 15: The 5km updraft swath (left) and accumulated rainfall (right) for each of the storms with increasing upper level shear (top-bottom). Adopted from Warren et al. (2017). 36

FIGURE 16: The thermodynamic profiles for the simulations ran in Grant and Van Den Heever (2014). Adopted from Grant and Van Den Heever (2014). 37

FIGURE 17: The total precipitation rate (a) for each of the simulated storms, which shows a stark difference between the control simulation and any of the dried simulations. The updraft velocity (b), which remained relatively unchanged for all but the M50 simulation. The updraft area at 6km AGL where the upward velocity exceeded 15 ms-1 (c), again smaller in each of the dried simulations when compared to the control. Adopted from Grant and Van Den Heever (2014). 38

FIGURE 18: A schematic diagram of the rain rate centroid (R_{cx}, R_{cy}) displacement relative to the storms motion (c). Adopted from Beatty et al. (2009). 39

FIGURE 19: The rain rate centroid displacement for HP, labeled as a black '+' and CL/LP labeled as a red 'X'. Adopted from Beatty et al. (2009). 40

FIGURE 20: Study area for the given research. All reports presented occurred from March - June. The study domain consists of latitudes from 24°N to 58

50°N and longitudes from 106.5°W to 90°W. Blue, green and red dots represent wind, hail and tornado reports reported to the SPC.

FIGURE 21: Severe reports for Storm 287. Green and red dots represent hail and tornado reports, respectively. 59

FIGURE 22: A flowchart of the methodology used in tracking supercell using Level III radar data, specifically the NMD (labeled Mesocyclones) and the NSS (labeled Storm Locations) products. 60

FIGURE 23: A conceptual diagram of a supercell that is superimposed on a set of axes in which its propagation is labeled in the up direction. 61

FIGURE 24: The distribution of the core displacement for the HP and LP/CL storms which were subjectively identified. 62

FIGURE 25: A schematic diagram depicting how the angle of the reflectivity core location was calculated. 63

FIGURE 26: A schematic diagram denoting the location of the inflow point in the model given the storm location that represents the storms location that is closest to an hourly observation. 64

FIGURE 27: A schematic diagram denoting how an area averaged sounding was acquired. 65

FIGURE 28: A representation of what was identified as being within the CL precipitation regime as analyzed by the tracking algorithm developed herein. 84

FIGURE 29: Same as in figure 28 but representing an HP supercell. 85

FIGURE 30: Same as in figure 28 but representing an LP supercell. 86

FIGURE 31: The core displacement for each storm mode identified by the tracking algorithm in a) the one developed herein and b) the one developed by Beatty et al. (2009), where b) was adopted from. 87

FIGURE 32: The number of each supercell precipitation archetype with LP/CL storms amalgamated due to their lacking discrepancies within the tracking algorithm. 88

FIGURE 33: The spatial distribution of supercells that fall into the LP/CL regime (blue) and the HP regime (red). 89

FIGURE 34: Cumulative frequency graph representing the relative frequency occurrence of LP/CL and HP storms in blue and red, respectively. 90

FIGURE 35: The distribution of supercells within the period of interest for this study (March – June). 91

FIGURE 36: Represented here is the average forward motion of each supercell regime as a violin plot. 92

FIGURE 37: Composite synoptic map at 300hPa over the contiguous United States. The top graphics represent LP/CL storms and the bottom graphics represent HP storms. On the left, standardized anomalies are presented whereas on the right, the geopotential height and wind speed are presented. 93

FIGURE 38: Same as in figure 37, but for the 500hPa surface. 94

FIGURE 39: As in the right half of figure 37, but regarding the mean sea-level pressure. 95

FIGURE 40: Composite sounding for both supercell groups. 96

FIGURE 41: Total precipitable water within the sounding for LP/CL storms and HP storms. Beneath the graph are the respective student t-statistic and p-value, KS-statistic and p-value, LP/CL normality test, HP normality test and spread of the data for each of the violin plots, specifically, the 25th, 50th and 75th percentiles as well as the range of the 25th-75th percentiles (IQR). The bolded text represents the test that is most appropriate given the distribution of the data. 97

FIGURE 42: Same as in figure 41, but for SBCAPE (a), MLCAPE (b) and MUCAPE (c). 98

FIGURE 43: Same as in figure 41, but for LCL Height. 99

FIGURE 44: Same as in figure 41, but for LFC Height. 100

FIGURE 45: Same as in figure 41, but for 1 – 3 km RH. 101

FIGURE 46: Same as in figure 41, but for the effective layer depth (a) and the effective layer PWAT (b). 102

FIGURE 47: Composite hodograph for LP/CL and HP storms, in blue and red, respectively. The numbers on the lines themselves represent the height of the observation AGL in kilometers. 103

FIGURE 48: Same as in figure 41, but for 0 – 1 km SRH (a), 0 – 3 km SRH (b) and effective layer SRH (c). 104

FIGURE 49: Same as in figure 41, but for the bulk shear magnitude from the boundary layer to 9 km AGL (a) and the bulk shear magnitude from 4 km to 10 km AGL (b). 105

FIGURE 50: Same as in figure 41, but for the u-component of the 4 – 10 km bulk shear vector (a) and the v--component of the 4 – 10 km bulk shear vector (b). 106

FIGURE 51: Same as in figure 41, but for the storm relative winds at 7 km AGL (a) and the normalized bulk shear from 3 km – 7 km AGL (b). 107

FIGURE 52: Same as in figure 41, but (a) the 0 – 1 km bulk shear magnitude, (b) the 0 – 3 km bulk shear magnitude and (c) the 0 – 4 km bulk shear magnitude. 108

FIGURE 53: The magnitude (top), u-component (middle) and v-component (bottom) of the storm relative flow, all of which have been rotated to the 0-4 km bulk shear vector. 109

FIGURE 54: The phase space diagrams for each of the shifts of in the threshold between LP/CL and HP storms as compared to the current threshold 110

(c). The minus 2 (a), minus 1 (b) and plus 2 (d) graphics are shown for comparison.

CHAPTER I: INTRODUCTION AND MOTIVATION

Supercell thunderstorms are prolific in the production of multiple forms of severe weather, including heavy rain, damaging winds, tornadoes (some large and violent), and even destructive hail, resulting in significant property damage and loss of life (e.g., MunichRe 2017; Gunturi and Tippett 2017; Lepore et al. 2017). Beyond this, supercell thunderstorms are also very unique in their structure when compared to that of other types of moist convection, such as single or multicell convection. Notably, one of the main distinguishing features is the quasi-steady rotating updraft that is a direct result of the interactions of the updraft with the shear present in the environmental wind profile (e.g., Rotunno and Klemp 1985). The appearance of this rotating updraft can differ both visually and on radar; the precipitation structure of a supercell can be classified as either low-precipitation (hereafter denoted as LP), classic (hereafter denoted as CL) or high-precipitation (hereafter denoted as HP; Rasmussen and Straka 1998).

As a result of the structural differences between these storms, there are variations in the types of severe weather produced. For example, CL storms are more prone to the production of hail and tornadoes, while HP storms are more prone to producing strong straight-line winds and flooding (e.g., Doswell et al. 1990; Moller et al. 1994). Therefore, being able to hone in on the environmental characteristics associated with each precipitation mode will enhance short-term forecasting and promote awareness of the potential severe weather hazards.

The facts of structural differences between these supercell precipitation types are well documented, but modeling and observational studies fail to agree upon environmental conditions that are required for each. For example, the observational study by Rasmussen and Straka (1998) indicate that the magnitude of the upper-level storm-relative flow is key; weak storm-relative winds were associated with HP storms, while LP storms were associated with stronger storm-relative upper-level winds. Rasmussen and Straka (1998) hypothesized that slower upper level flow allows for more hydrometeors to be ingested into the updraft, resulting in an HP structure; in contrast, stronger upper level flow transports hydrometeors away from the updraft, producing an LP appearance. However, more recently, Warren et al. (2017) conducted an idealized modeling study that found the opposite association; simulations demonstrated that surface precipitation significantly increased with stronger upper-level shear. This discrepancy presents an opportunity to dig deeper into the role of the environment in determining the structure of supercell thunderstorms. Indeed, given that the different precipitation structures of supercells are associated with differing storm hazards, such an understanding would promote improved short-term forecasts and warnings of supercell thunderstorms.

With regard to the project as a whole, the majors goal set herein include the use of an expansive dataset to help investigate the contrary findings among observational vs. modeling studies (e.g. Rasmussen and Straka 1998 vs. Warren et al. 2017) as well as observational vs. observational studies (e.g. Bluestein and Parks 1983 vs. Rasmussen and Straka 1998). In addition, trying to identify any other potential variables that may signify

shifts in precipitation mode will be featured. To achieve said goals, a semi-objective tracking of a large number of observed supercells needs to be carried out with storm precipitation mode identified for each, which will follow pieces of the tracking algorithm developed in Beatty et al. (2009). Additionally, model initialization data will be obtained for use as near storm environmental conditions.

CHAPTER II: BACKGROUND

a) Supercell Structure and Dynamics

Owing to the destructive nature of supercell thunderstorms, much research has explored these storms, beginning with the earliest documentation in the 1950's and 1960's (e.g., Newton and Kats 1958; Browning 1964). For example, Browning (1964) described a "Severe Right" storm, which later became more commonly known as a right-moving supercell. One of the features associated with a supercell is a well-defined area of low reflectivity, referred to as the vault (Browning 1964), more commonly known as the bounded weak echo region (BWER). The BWER is spatially correlated with the supercell's updraft and a distinct hook echo which generally surrounds the vault at low levels. The hook echo is also where the rotating updraft (i.e., the mesocyclone) is found (Fig. 1).

Our current understanding of supercell thunderstorms was not yet born until the advent of Doppler radar, which allowed for more detailed examination of such storms, including the identification of distinct features such as the hook echo and BWER. For example, Lemon and Doswell (1979) described the evolution of a storm into a supercell, beginning with the development of a mid-level echo overhang and accompanying BWER; the authors noted that the BWER is a direct result of a strong and persistent updraft along with strong divergence at the top of the updraft. Next, due to the persistence of the updraft, a mid-level mesocyclone forms near 5-8 km above ground level (AGL); indeed, the presence of an updraft within an environment with strong vertical wind shear was later demonstrated to be key in producing mid-level rotation (e.g., Rotunno and Klemp

1985). The size of the mesocyclone is approximately 5-10 km across and generally has a quasi-solid core circulation (Lemon and Doswell 1979). Later, as the supercell dissipates and the mesocyclone weakens, the BWER accordingly “fills in” as reflectivity values increase in this region.

Another notable finding from Lemon and Doswell (1979) was the presence of two distinct downdrafts, namely the forward flank downdraft (FFD) and the rear flank downdraft (RFD; see Fig. 2). The FFD is generally weak and discontinuous at the surface and occurs at the forward and right flanks of the storms’ radar echo. The storm may begin to develop a quasi-stationary boundary along the right flank of the radar echo as it propagates (Fig. 2). The RFD contains potential temperatures compatible with that of mid-level ambient air, divergence and strong pressure excesses in the storm’s rear flank, immediately aft of the trailing hook echo (Lemon and Doswell 1979). This air is mostly distinguishable from that of the FFD because it is drier, denser and cooler. Note that the canonical Lemon and Doswell (1979) schematic is relevant to the mature stage of the supercell, though the features may dissipate and reinvigorate subject to the persistence of the storm as illustrated in Figure 3. Additionally, as will be discussed later in this chapter, the features shown by Lemon and Doswell (1979) are consistent with those of a classic supercell.

As the number of observations of supercells increased, so did our understanding of the fundamental processes which govern these storms. The dynamics of supercells are unique when compared to that of ordinary convective storms. Beginning in the early development stages, updraft rotation ensues as a direct result of the sheared

environment in which it is born into. This rotation is in the form of counter-rotating vortices along the flanks of the vertically rising air (Wilhelmson 1974). These counter-rotating vortices result from the lifting of crosswise vorticity by the updraft, indicating that the storms mean flow is perpendicular to that of the environmental shear, forcing the vortices to be on the flanks of the updraft as in this case (Davies-Jones 1984; Fig. 4a). In contrast, a storm which ingests purely streamwise vorticity will only produce a single rotating vortex, which will be lined up with the upward motion; this is a result of a storm's mean flow being in line with the environmental shear vector (Fig. 4b). The generation of this vorticity, in both cases, is in the form of both horizontal and vertical components and can be expressed in mathematical terms (Klemp 1987) as:

$$\frac{d\omega_h}{dt} = \omega \cdot \nabla v_h + \nabla \times \left(B\hat{k}\right) + F_h', \quad (1)$$

$$\frac{d\zeta}{dt} = \omega_h \cdot \nabla w + \zeta \frac{\delta w}{\delta z} + F_\zeta', \quad (2)$$

From (1), there are three terms that related to horizonal vorticity (ω_h), they include the tilting and stretching term ($\omega \cdot \nabla v_h$), the baroclinic generation term ($\nabla \times \left(B\hat{k}\right)$) and the mixing term ($F_h'$). From (2), there are three terms that feed into generation of vertical vorticity (ζ) which include the tilting of the horizonal vorticity ($\omega_h \cdot \nabla w$), the stretching of that tube ($\zeta \frac{\delta w}{\delta z}$) and finally mixing ($F_\zeta'$). It is important to note that, in most cases, the mixing terms of both equations are negligible in terms of their contributions to vorticity. The resulting application of these two equations means that strongly sheared

environments, particularly near the surface, are prime for the production of rotating updrafts.

Following the development of a rotating updraft, a supercell may split into two distinct cells, though this process is sensitive to the environmental wind profile. There are copious studies that relate to the splitting of supercells into two cells, one with a cyclonically and the other with an anti-cyclonically rotating updraft, with limited dynamical information regarding the splitting process (e.g., Fujita and Grandoso 1968; Achtemeier 1969; Fankhauser 1971). One of the most marked of these papers is Klemp (1987). Precipitation produced by the storm is responsible for creating a downdraft within the cloud by creating negative buoyancy. In environments with weaker vertical wind shear, this process is detrimental to a storm's longevity. However, in strongly sheared environments that supercells form in, storm longevity is enhanced due to two factors: easterly storm-relative inflow, as well as pressure perturbations along northern and southern flanks of the updraft. The combination of these correlate to a splitting of the original cell into a right-moving and left-moving cell, having cyclonically and anti-cyclonically rotating updrafts, respectively (Fig. 5). The research presented in this study focuses solely on right-moving supercells, as they tend to dominate in the Great Plains of the U.S. (see Data and Methods for further discussion.) The favoring of right-moving supercells in curved hodograph cases (i.e., when the environmental wind shear veers with height) is related directly to the vertical pressure gradient forces that set up in such environments. The upwardly directed pressure gradient force on the south flank of the storm is in the same quadrant as the positive vertical vorticity (Fig. 6).

b) The Supercell Spectrum

Thus far, supercells have been described by their broad structure and key features (i.e., the rotating updraft, BWER, and hook echo). However, numerous studies have indicated three distinct categories related to the structure of precipitation found in supercells, described as classic (CL; Fig. 7), low-precipitation (LP; Fig. 8), and high-precipitation (HP; Fig. 9) storms. The key similarities and differences among these supercell classifications, both visually and environmentally, as well as the different severe hazards associated with each, will be described in more detail next.

i) CL Characteristics

Classic supercells are, as the name implies, the canonical version of a supercell. Since the Supercell Dynamics and Structure section focused mainly on the structure CL supercells, here will only represent a brief overview of the visual appearance of CL supercell structure as well as specific environmental conditions that tend towards this archetype over the others.

The iconic paper presented by Lemon and Doswell (1979) denote, with great detail, the structure and evolution of a CL supercell (Figs. 2-3). On radar, a CL supercell has a defined hook echo near the mesocyclone. The mesocyclone itself resides within the region of the hook echo and results in the BWER evident on radar. In this case, the heaviest precipitation remains ahead of the mesocyclone and updraft area and as a result stays out of the hook region of the echo (Fig. 7). As will become evident in subsequent discussions, a CL supercell lies in the middle of the precipitation spectrum (e.g., Bluestein

and Parks 1983; Rasmussen and Straka 1998) due to the fact that such features are clearly and easily identified both visually and on radar.

Regarding the specific environmental conditions that are ripe for the existence of this archetype, it was found that the level of free convection (LFC) tends to be significantly lower in CL storms compared to other supercell archetypes (Rasmussen and Straka 1998). This then implies that either the convective inhibition (CIN) is weaker and/or the lapse rates are greater above the lifting condensation level (LCL). Additionally, the precipitable water in environments associated with CL supercells is significantly lower than that of HP environments, but does not differ from that of LP environments (Rasmussen and Straka 1998). The deep layer shear magnitude for CL storms generally sits in the middle when compared to the other archetype and there is an inverse relationship associated with deep layer shear and precipitation production (Rasmussen and Straka 1998).

ii) LP Characteristics

The term LP stems from the radar presentation of this storm type, since most, if not all, of the precipitation is displaced from the updraft region; as evident in Fig. 8, no visual hook echo or BWER is evident in the radar signature. Visually, little to no precipitation appears to fall in the rear flank of the storm (e.g., Beatty et al. 2008).

LP storms are usually rarer in nature as they are generally confined to the regions where there are lower levels of moisture such as near a dryline and in the western portions of the Great Plains (Bluestein and Parks 1983; Moller et al. 1994). They are also harder to identify on radar due to their lack of precipitation and lower-reflectivity values; they are exceptionally unique in their precipitation structure when compared to other

classifications of supercells. There have been a number of observational studies dating back to the 1970's relating to their unique structure. In Burgess and Davies-Jones (1979), they included a summary of eyewitness observations related to a tornado producing thunderstorm. It was noticed that there was only reports of a brief shower or a few large raindrops falling from the base of the cloud with the tornado being strikingly visible from pretty much all angles. This relates to the definition of a low-precipitation supercell, though usually there are only funnels being produced from the mid-levels of the mesocyclone.

The synoptic set-up for such storms is equally as important as the structure of the storm itself. Knowing where and which environments these types of nearly precipitation void storms have their beginnings are not only interesting, but necessary for their study. LP supercells have very low precipitation efficiency, implying that other types of supercells are thus likely to be more efficient at producing precipitation (Bluestein and Parks 1983). Foote and Fankhauser (1973) note that precipitation efficiency decreases with an increase in vertical shear, specifically for High Plains storms. Synoptically, these storm types tend to form near a dryline (e.g., Rasmussen and Straka 1998), though that is not always the case. Bluestein and Parks (1983) found no relationship between upper-level jet streaks and LP storms, which argues the fact that LP storms do not form in the same fashion as that of classic supercells. Additionally, there wasn't even an outflow boundary apparent in synoptic data to help initiate the storms, again leading to their unique formation patterns/locations.

Related to the environmental parameters of LP storms versus other supercells, there are a few that are important related to moisture, thermodynamic and kinematic parameters. The significant variables are summarized in Table 1 and include precipitable water (PWAT), the mean mixing ratio in the lowest kilometer of the atmosphere, mean RH (relative humidity) of the sounding, the LCL, the convective condensation level (CCL) and the speed of the mean tropospheric wind vector. LP storms do not differ, however, in the depth of the moist layer, the quantity of maximum buoyancy nor the deviation of the storm speed or direction from that of the mean tropospheric wind (Bluestein and Parks 1983), which physically makes sense as both still reside in the supercell spectrum and should deviate from the mean wind in a very similar manner. However, Rasmussen and Straka (1998) found no significant difference among the supercell classifications with regards to LCL height as their values for LCL height were more representative of the large scales environment rather than the conditions specific for the supercell, which can vary greatly as a result of mesoscale fluctuations in both low-level moisture and temperature.

In another study, Bluestein and Woodall (1990) analyzed LP storms via radar observations as well as their transition over time. Many of the storms studied began along a dryline exhibiting LP-like characteristics, with at least one storm splitting and the right-moving storm became more HP-like in its precipitation structure. Thus, it should be noted that storms can evolve from one precipitation structure into another; keeping in mind that the precipitation structure did not evolve until after the splitting of the original cell. The vertical velocity profile for the LP storm had a much shallower updraft with a peak in intensity around 5-6 km AGL where the post-split HP-like supercell had a much stronger

updraft with peak intensities much closer to a lifted parcels equilibrium level (EL) (Bluestein and Parks 1983; Bluestein and Woodall 1990; Fig. 10). For further details related to HP storms, the reader is directed to the HP Characteristics subsection later in this chapter.

Rasmussen and Straka's (1998) study also signify that LP storms have a rather strong, storm relative upper-level outflow when compared to other supercell precipitation modes, particularly for winds above 8 km AGL (Fig. 11). In addition, above this level, the storm relative flow backs quite strongly. Furthermore, the BL – 9 km (33 ms^{-1} for LP) and 4 – 10 km (22 ms^{-1} for LP) storm relative shear magnitudes were found to be significantly higher for LP storms when compared to HP storms with most of this difference accruing above 4 km AGL (Fig. 12).

Physically, the combination of backing winds with stronger upper-level flow in LP storms results in precipitation falling further to the left of the storm path. This is particularly striking in comparison to HP storms, where upper-level winds have been shown to veer (Fig. 13), resulting in more precipitation falling closer to the updraft. It is hypothesized that storm motion may play the largest role in determining these upper-level profiles, especially what would constitute a veering or backing profile (Rasmussen and Straka 1998).

Regarding hazards associated with LP storms, they are generally weaker than that of other precipitation modes. Due to a lack of precipitation, they are largely void of any strong outflow that would otherwise be precipitation-driven among others in the supercell spectrum (Bluestein and Parks 1983; Bluestein and Woodall 1990). In addition,

while tornadoes can be produced, they are generally weak. Finally, regarding their hail production, LP storms are able to produce large hail, which can help to explain their relatively high reflectivity values aloft (Davies-Jones et al. 1976).

iii) HP Characteristics

The radar characteristics of HP storms makes them unique visually as well as in their production of severe weather. On radar, they generally have a kidney bean shaped appearance (Fig. 9) as precipitation is wrapped around the updraft in the low levels. Consequently, reflectivity values are higher immediately adjacent to the rotating updraft. Accordingly, tornadoes that do occur are typically less frequent and less violent in comparison to CL storms. In addition, because of the higher reflectivity values associated with these storms, they are generally more likely to produce flooding, resulting in strong precipitation-driven outflow and intense straight-line winds (Lemon and Burgess 1993; Lemon and Parker 1996).

HP storms have also had significant documentation over the years in observational studies and are easiest to compare and contrast with that of LP supercells. Accordingly, the HP regime generally exhibits higher values of PWAT (Bluestein and Parks 1983; Rasmussen and Straka 1998). In addition, there is a unique wind profile associated with HP storms as several shear parameters differed compared to LP storms.

The wind profile is of major importance when dealing with HP storms. As found by Rasmussen and Straka (1998), HP storms are associated with veering winds near 7 km, as well as weaker upper level flow (Figs. 11 and 13). This weakness in upper level flow is hypothesized to transport hydrometeors a shorter distance from the updraft, which

allows for recirculation of more hydrometeors into the updraft from the forward flank, thus resulting in increased precipitation in the rear flank and a kidney bean shaped hook echo (Fig. 9).

Expanding on the importance of the wind profile, BL – 9 km (26 ms^{-1} for HP) and 4 – 10 km (15 ms^{-1} for HP) shear vector magnitudes are significantly lower compared to LP storms (Fig. 12) and between 5 and 9 km AGL, 9 of the 13 HP storms identified in Rasmussen and Straka's (1998) study showed a veer in this layer for storm relative winds. In addition, the HP cases propagated more in line with the BL-4 km environmental shear vector, lending to reduced upper-level storm relative flow.

c) Modeling Studies

Modeling studies have been useful in determining the sensitivity of supercell morphology to various aspects of the storm's environment, including thermodynamic (e.g., McCaul and Cohen 2002; Grant and Van Den Heever 2014; Honda and Kawano 2015) and kinematic (e.g., Warren et al. 2017) shifts. However, as described below, these findings are not always consistent with the observations, which thus motivates additional investigation.

i) Kinematic

One of the key observational studies of supercell classifications, Rasmussen and Straka (1998), indicated that the upper-level wind profile was an important characteristic producing the varying storm morphologies. Warren et al. (2017) went on to test whether this could be reproduced within an idealized model. In this study, various configurations of the upper levels of the wind profile (6-12 km) were tested (Fig. 14). The main finding

of this study was that as the upper level shear increased, the simulated storms became more outflow dominant and a more HP-like structure to the cells was observed, in direct contrast to the findings of Rasmussen and Straka (1998). It is also noted that the simulated storms' ground speed also increased with increasing upper level shear. This increase in the forward speed allowed for stronger storm relative flow near the surface, thus increasing the low-level inflow of higher θ_e (equivalent potential temperature) air. A more HP-like structure would indicate an increase in precipitation at the surface and is exactly what was observed in Warren et al. (2017) in all but the US30 case (Fig. 15). In addition, the updraft width also increased with the increasing shear in all but the US30 case (Fig. 15). This increase in updraft width allows for an increase in mass flux as well as condensate production (Warren et al. 2017), both of which help to increase precipitation production.

Regarding the veering and backing profiles, storms acquired heavier precipitation in their rear flank with backing winds and veering winds helped to elongate the updraft and precipitation shield, which promotes a more LP-like structure to the cells (Warren et al. 2017). Again, this finding is in stark contrast to that found in Rasmussen and Straka's (1998) study. However, it is worth noting is that the Warren et al. (2017) study only focused on a single moist thermodynamic profile; thus, it is possible that their results were biased towards HP supercells.

ii) Thermodynamic

Relating to the thermodynamic environment, changes in the temperature and moisture profiles determine specific structuring of storms, a lack of moisture and/or an

insufficient temperature and storms will not have the necessary ingredients for their existence or sustainability. More specifically, if an environment is warm enough, but the moisture at say a mid-level in the atmosphere is sub-ideal, then precipitation structure and storms longevity is to be altered as a result (Grant and Van Den Heever 2014; Honda and Kawano 2015).

In a modeling study carried out by Grant and Van Den Heever (2014), introduction of dry air within different levels of the environment were analyzed; dry air was introduced at three different central locations, 2.0, 2.5 and 3.5 km AGL with varying intensities to investigate the sensitivities of supercell evolution to the vertical distribution of dry layers, hence the three dry layer central locations implemented in their study (Fig. 16). Dry air introduced at lower levels produced much more profound effects on precipitation production than that of dry air at higher levels, though a difference is still noted in all dried simulations when compared to the control. In addition, the area of the updraft also shrunk when increasing the dryness of the air at a given level. This in combination with the relatively unchanged updraft velocity peak yields the conclusion that an increased intensity of a dry layer decreases the upward mass flux and thus the precipitation production of a supercell thunderstorm (Fig. 17). The decreased upward mass flux yielding less precipitation at the surface is consistent with Warren et al. (2017). It is also noted that changes in RH within the well-mixed boundary layer have much more profound implications on precipitation characteristics related to the storm then when the dry layer is above such a well-mixed boundary layer (Grant and Van Den Heever 2014).

This also consistent with findings from McCaul and Cohen (2002) as well as Bluestein and Parks (1983).

Honda and Kawano (2015) also conducted a study where mid-level tropospheric air was introduced into a sounding and the evolution of the storms in such environments was observed. Dry air at higher levels (2.7 – 5.2 km AGL) in the atmosphere concluded a longer sustained supercell than the same magnitude of dry air closer to the surface (1.7 – 4.2 km AGL). With the drier air further aloft, the entrainment of air with such dry characteristics into the updraft because it may be more difficult of the further aloft to reach the surface (Honda and Kawano 2017) and it has been shown that the maximum updraft entrainment occurs near the base of cumulonimbus clouds (Cohen 2000). This concludes that the co-location of the LCL with dry air in the atmosphere will have profound impacts on a storms strength and precipitation structure as a result.

d) Semi-Objective Storm Tracking

The tracking of supercells and their precipitation structure on radar has traditionally been done subjectively with the analyzer's knowledge put to work trying to identify the precipitation mode of a given cell. While the human eye can detect subtleties useful for identification, the idea of taking the subjectivity out of this identification will allow for a much larger dataset to be analyzed in hope to leading to a better and more complete understanding of the environments that relate to each of the precipitation modes within the supercell spectrum.

The idea of a semi-objective identification method for tracking of supercells has been developed using radar (Beatty et al. 2009). Their approach begins with an estimation

of the precipitation core location using a rain rate centroid. The instantaneous rain rate was calculated using a reflectivity-rain rate (or Z-R) relationship as (Vieux and Bendiet 1998):

$$Z = 0.01R^{0.833} \tag{3}$$

where the consideration of reflectivity values that fall specifically in the range from 10 – 53 dBZ (inclusive) are considered, as values below may reflect variations in the index of refraction (Knight and Miller 1993) and values above this range may be a result of a bias created by hail (Vieux and Bendiet 1998). It's worth noting that this relationship is specific for current generation of radar (WSR-88D). Using the calculated rain rate, a centroid of a given cell could be identified, assuming the boundaries of the cell are known (see Fig. 18 for a schematic of a rain rate centroid relative to a cells motion and speed). The storm's average motion and speed was identified using a least squares regression of the rain rate centroid at every location of its existence.

Beyond this, knowing the characteristics of a supercell would denote the importance of a quasi-steady rotating updraft. Finding its location is important for the tracking of such cells; specifically, the low-level updraft, so a side-by-side comparison with that of the central rain rate location can be made and ultimately define the semi-objective method for the identification of a supercell's precipitation mode. The problem is being able to determine the low-level updraft. In Beatty et al. (2009), a combination of methods was used to identify the updraft location at different levels within the atmosphere and ultimately the tilt of the updraft such that its location can be extrapolated to the low-levels at the same height as the rain-rate data, which was acquired from the base scan of

the radar. There were three methods used to identify the updraft location at varying levels. One, the identification of the BWER in the mid-levels is defined as a sufficient, but not necessary condition for the identification of a mature and organized updraft (Browning 1978). Two, the BWER is overlain by elevated values of reflectivity, which can be used to identify the updraft location at upper levels (Lemon 1977). The third method is through a minimum in spectrum width as the core of an updraft has been, in previous studies, identified as being mainly non-turbulent (Lemon and Burgess 1993; Lemon and Parker 1996). This attribute is generally evident through multiple scan elevations.

The semi-objective nature to this tracking method is evident mainly in the mesocyclone tracking, where the BWER and location of the heighted reflectivity values at the top of the BWER are hard to program as an algorithm. In addition, the rain rate centroid is also related to the boundary of the storms reflectivity signature. If a storm was interacting with another storm or splitting into right and left moving cells, for instance, or not isolated for any other reason, then the extent of the storm needed to be identified subjectively (Beatty et al. 2009).

In all, with the implication of the tracking algorithm defined in Beatty et al. (2009), there was an important conclusion to draw from their study, which was that only two distinct precipitation modes were able to be identified (Fig. 19). Of these two modes, it was evident that storm identified as HP had a more leftward bias to the rain rate centroid displacement location. The other category combined CL and LP together, with a more rightward bias is evident in the displacement of the rain rate centroid. However, given the limited number of cases analyzed (6), further analysis of a large number of supercells

is needed to determine whether the original precipitation spectrum (CL vs. LP vs. HP) is an accurate reflection of reality.

e) Concluding Remarks and Hypothesis

There have been a multitude of studies both observational and modeling based that have looked towards the issue of supercell evolution, both dynamically and tangibly. The observational studies (e.g., Bluestein and Parks 1983; Bluestein and Woodall 1990; Rasmussen and Straka 1998) have investigated almost any variable that may differ between the different supercell regimes. Often times, they have contradicted each other, which may be a result of one person identifying cells as one precipitation mode versus another, which can easily be done; subjectivity is the biggest contributor to this potential error. The modeling studies (e.g., Grant and Van Den Heever 2014; Honda and Kawano 2015; Warren et al. 2017) have generally been consistent in their findings among each other, though contradictions occur when relating their findings to the observationally based studies. The development, therefore, of a tracking algorithm that can take as much of the subjectivity out of the identification of the precipitation mode related to supercells is necessary for the best understanding of these unique storms. Beatty et al. (2009) developed an algorithm that is semi-objective in nature but will not suffice for large datasets spanning the course of multiple years. It is therefore the due diligence of this research to help develop a tracking algorithm that takes as much of the objectivity out of storm cell tracking as possible such that a large dataset can be examined for the most fortified results regarding the atmospheric conditions related to each precipitation mode within the supercell regime.

Aside from the implementation of a mostly non-objective tracking algorithm for use in an expansive dataset, a hypothesis needs to be drawn as something to work towards. The hypothesis presented here is that observationally based studies provide a better insight into the actual environments, both on a meso and synoptic scale, that govern each of the supercells in the spectrum when related to modeling studies. While modeling studies use microphysics schemes and they do a pretty good job at modeling the atmosphere, they have their limitations and may ultimately produce skewed results and thus inconsistent conclusions. In the end, the goal of this research is to use an expansive dataset and try to identify environmental influences that skew the precipitation mode of supercells into their respective categories and ultimately compare and contrast the results with smaller studies, both modeling and observationally based, that have been conducted in the past.

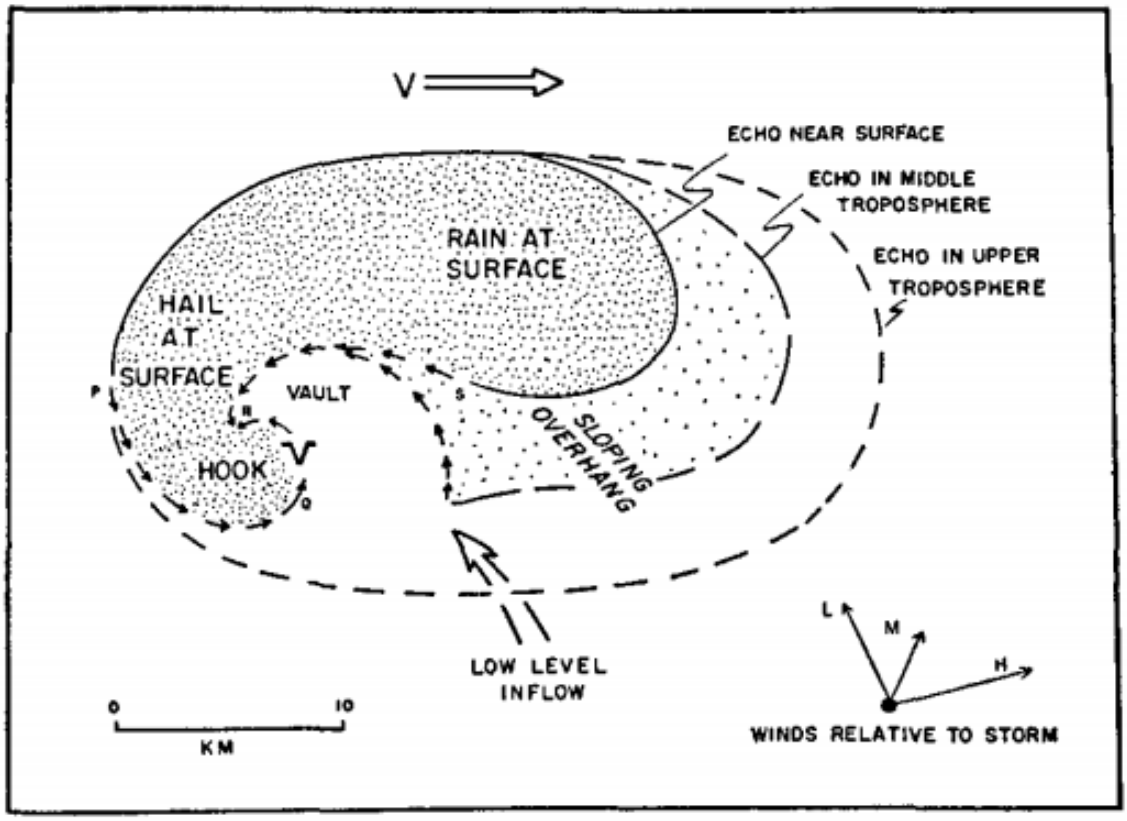

Figure 1 - A schematic of a supercell's reflectivity at three different levels, namely near to the surface, the middle troposphere and the upper troposphere. In addition, the location of the hook near the surface as well as the vault is labeled. Figure adopted from Browning (1964).

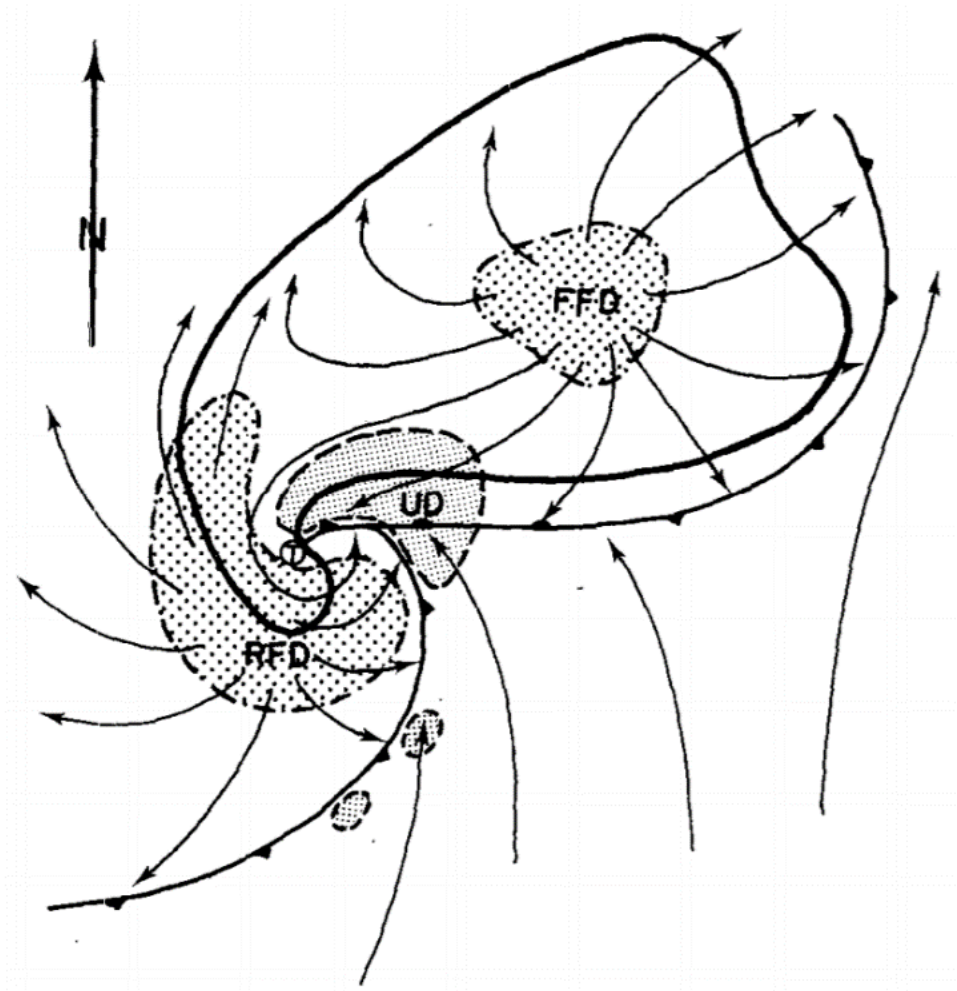

Figure 2 - A schematic diagram of the updraft and downdraft structure of a supercell. RFD, FFD and UD refer to the rear flank downdraft, the forward flank downdraft and the updraft, respectively. Additionally, the gust front structure related to the downdrafts is shown, which corresponds to the cold, warm and occluded fronts. The thick line corresponds to the echo at low-levels. Image adopted from Lemon and Doswell (1979).

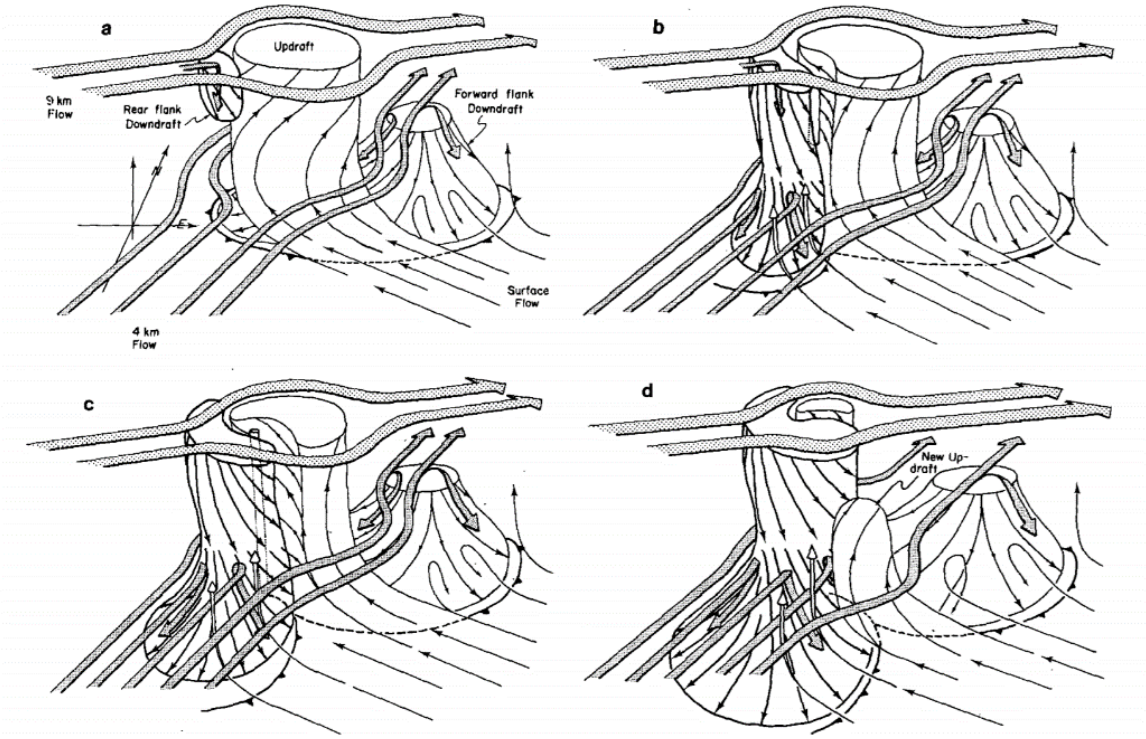

Figure 3 - A schematic diagram representing the flow into, out of and around a supercell. In addition, the cycling of the updraft and downdrafts are shown chronologically (a-d). The progression of the gust fronts is also shown. Adopted from Lemon and Doswell (1979).

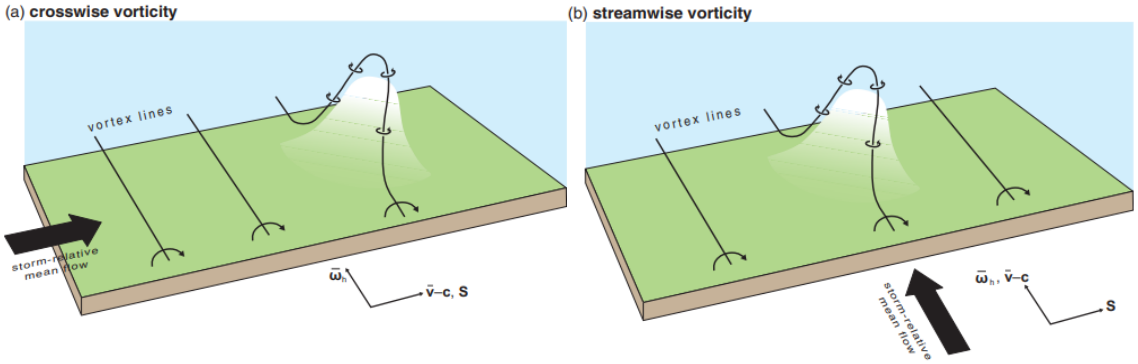

Figure 4 - Simplified depiction of the lifting of streamwise (b) and crosswise (a) vorticity along an isentropic surface. (a) The purely crosswise vorticity being tilted into the vertical results in a couplet of vortices that are in no way correlated with the perturbation in vertical motion. (b) The tilting of purely streamwise vorticity results in a couplet of vortices that is in direct correlation with the area of rising (sinking) motion on the uphill (downhill) side of the isentropic surface. Adapted from Davies-Jones (1984).

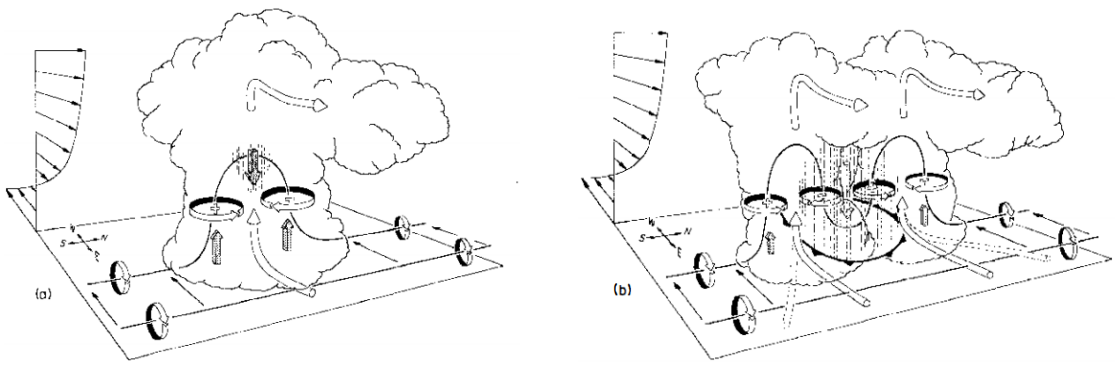

Figure 5 - A schematic diagram that depicts the splitting of one cell into right and left moving cells in a westerly sheared environment. Adapted from Klemp (1987).

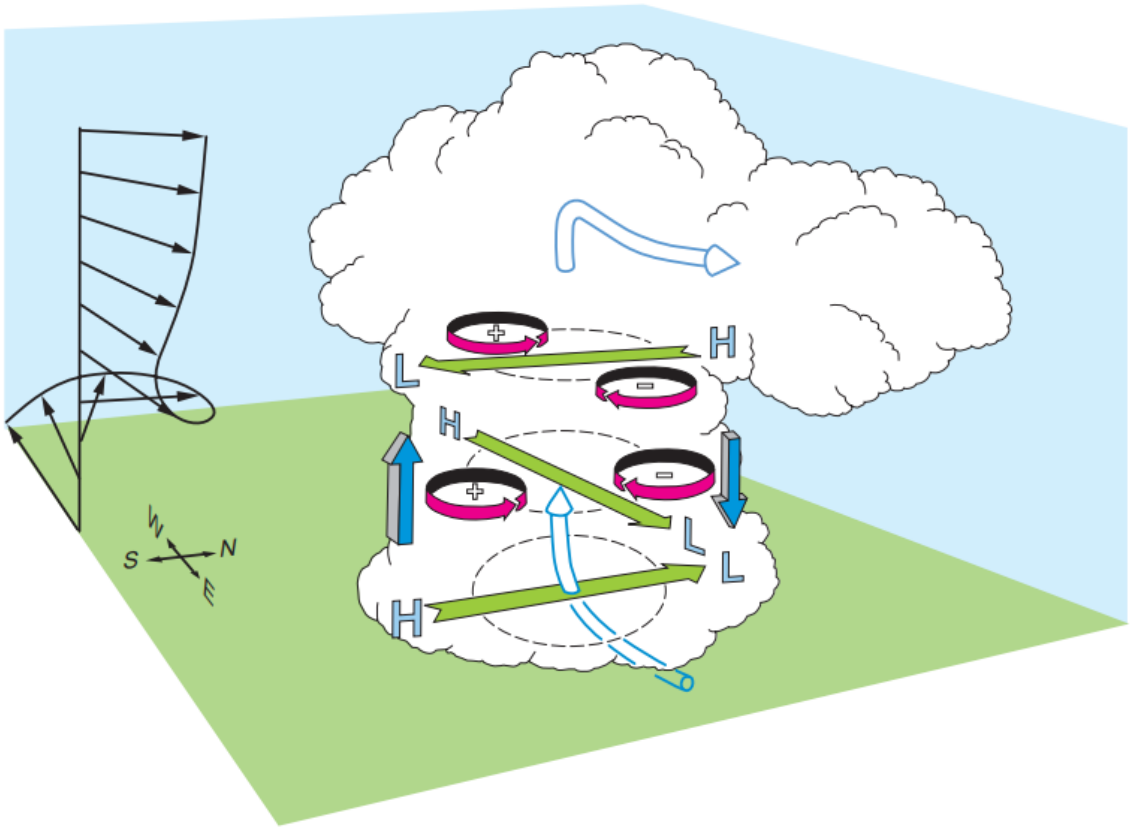

Figure 6 - A schematic diagram representing the vertical pressure gradient force that is created in a vertically sheared environment where the winds veer with height. The upward directed pressure gradient force on the southern flank of the storm favors right-moving supercells. Adopted from Markowski and Richardson (2014) Mesoscale Meteorology Textbook.

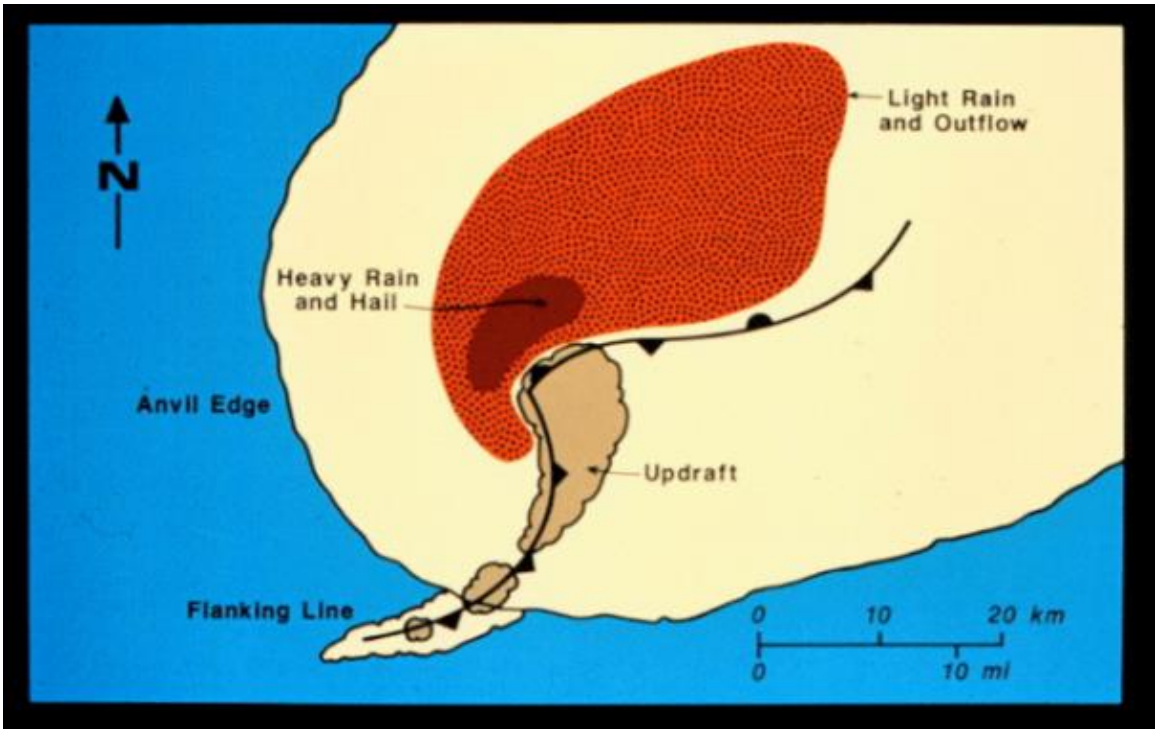

Figure 7 - Low-level radar depiction of a CL supercell overlaid on the cloud features associated with the storm. The updraft region is also labeled. Adopted from Doswell and Burgess (1993).

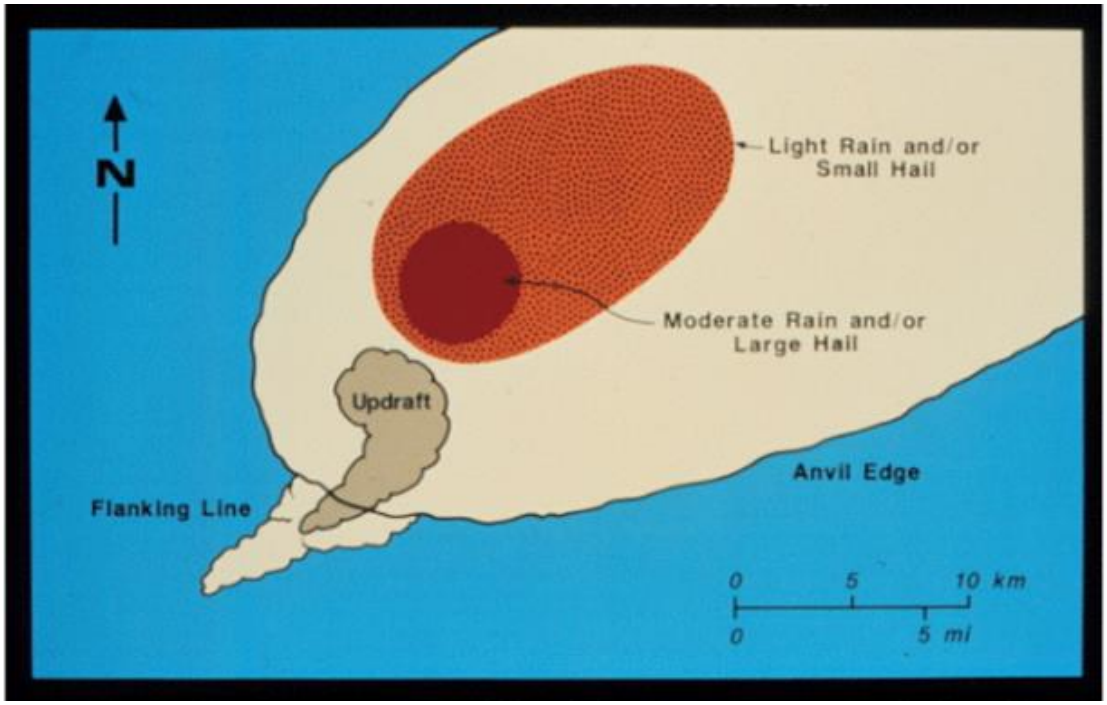

Figure 8 – Same as in figure 7, but for the LP supercell. Adopted from Doswell and Burgess (1993).

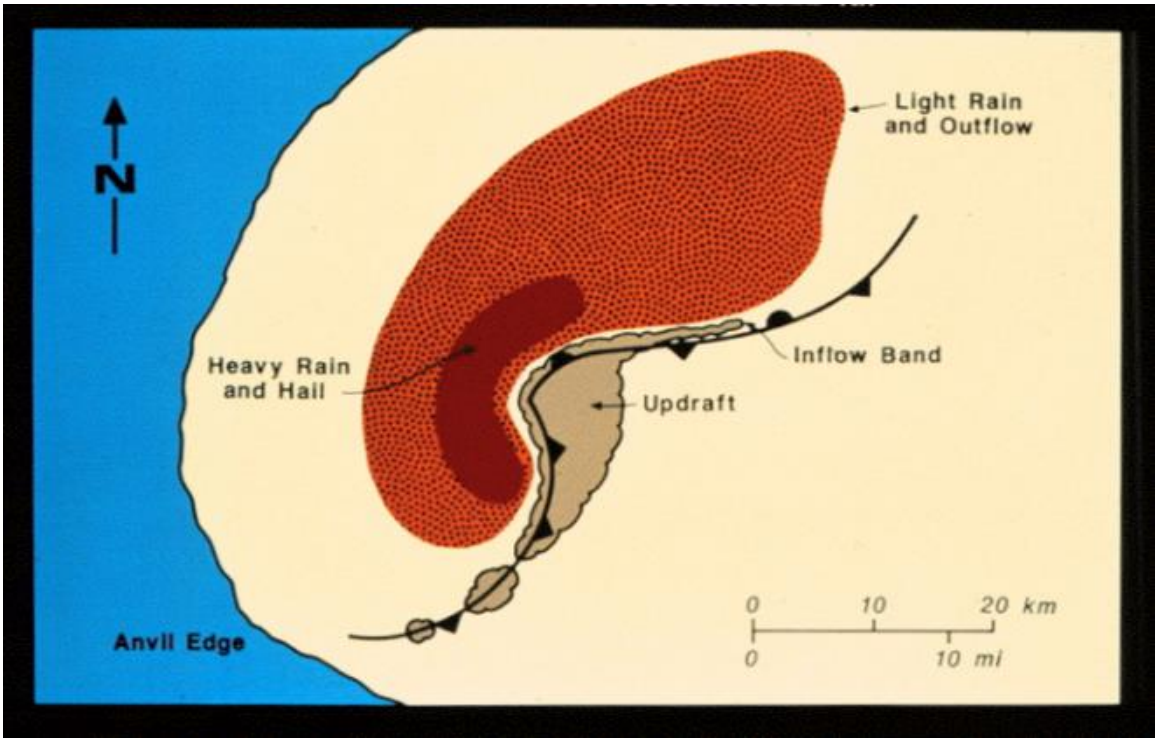

Figure 9 - Same as in figure 7, but for the HP supercell. Adopted from Doswell and Burgess (1993).

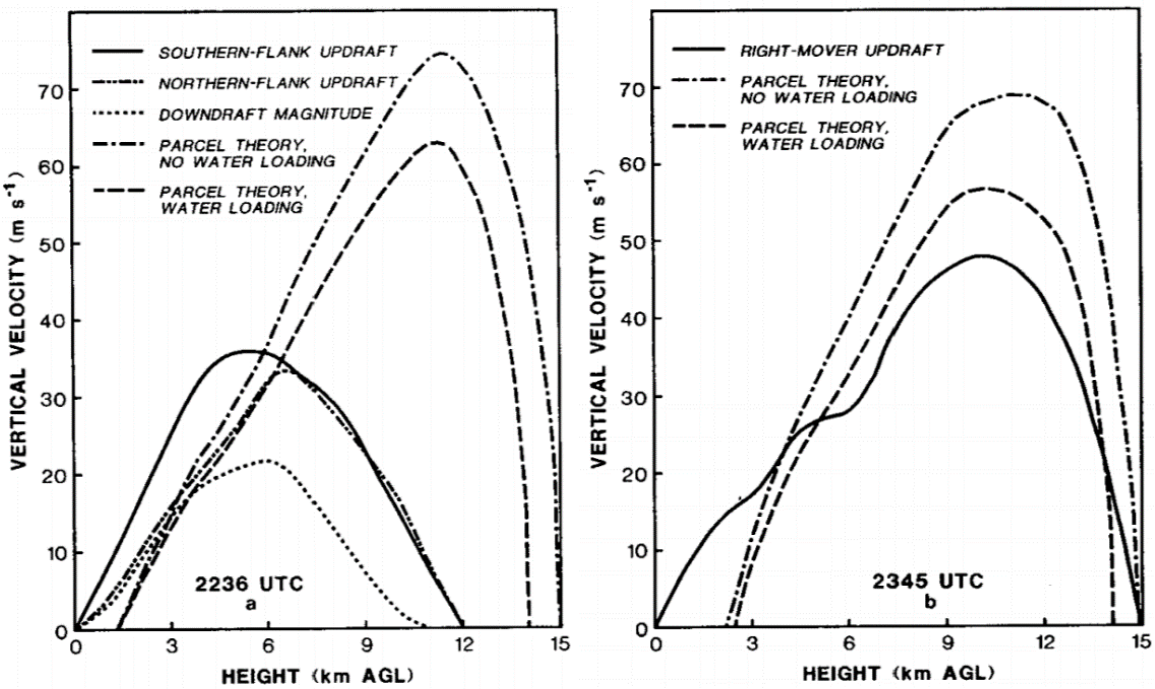

Figure 10 - Updraft profiles for a pre-split (a), more LP like supercell and a post-split (b), more HP-like supercell. Adapted from Bluestein and Woodall (1990).

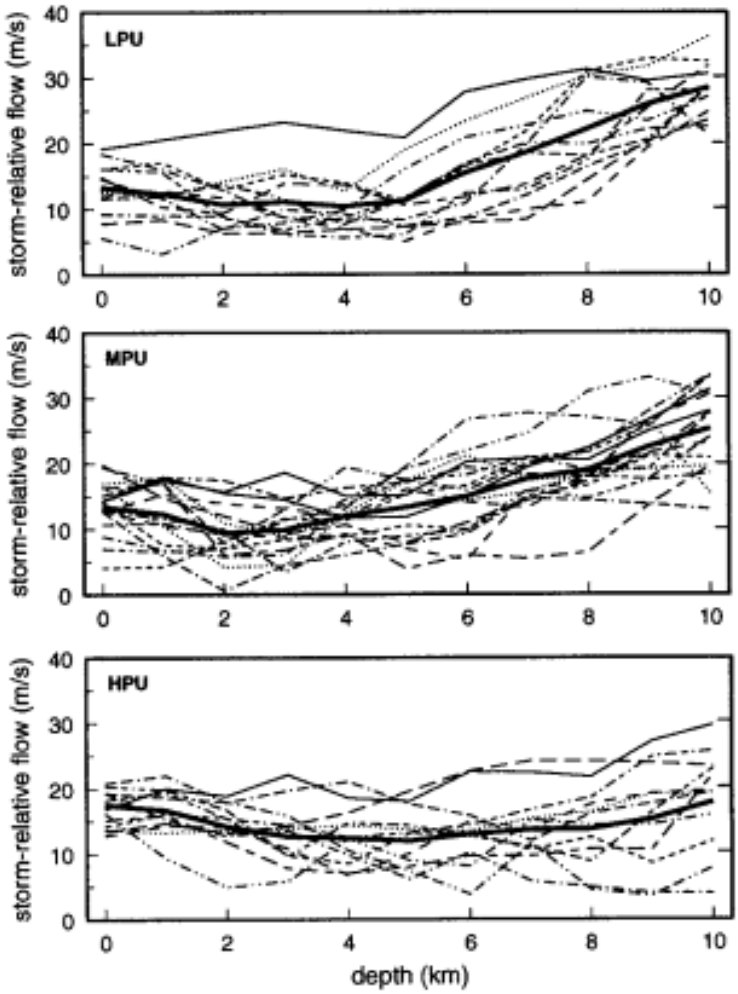

Figure 11 – Storm relative flow for LP, CL and HP storms ranging from top to bottom, respectively. The solid black curves represent the mean for each of the precipitation modes. Adapted from Rasmussen and Straka (1998).

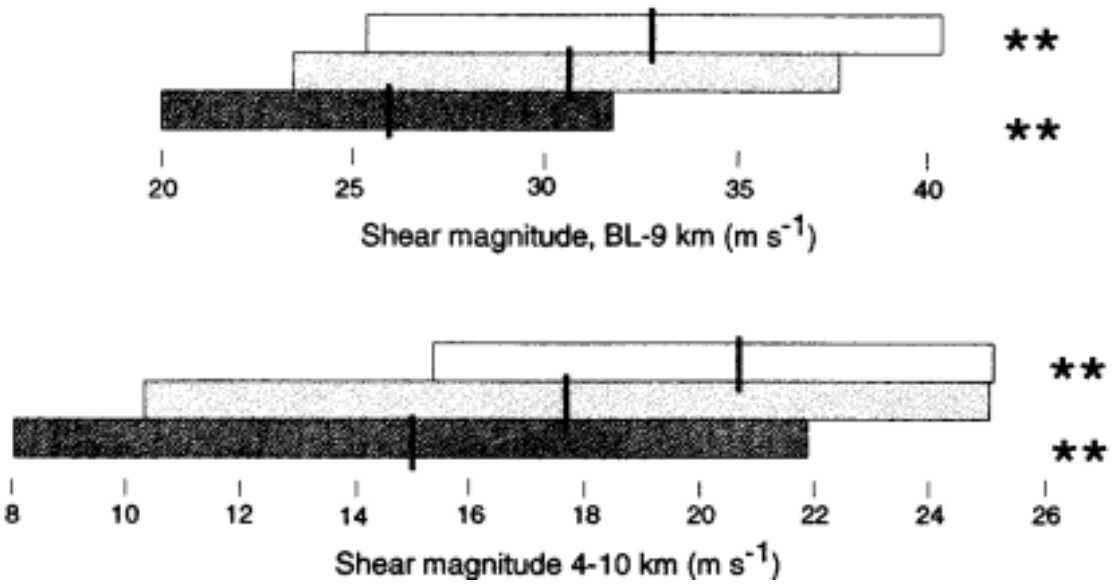

Figure 12 – The shear magnitudes for each of the precipitation modes, with the black, gray and white bars representing HP, CL and LP storms respectively. The black vertical marker represents the mean and the width of the bar represents ±1 standard deviation from the mean. Finally, the double asterisks demarcate significance at the 98% confidence level. Adapted from Rasmussen and Straka (1998).

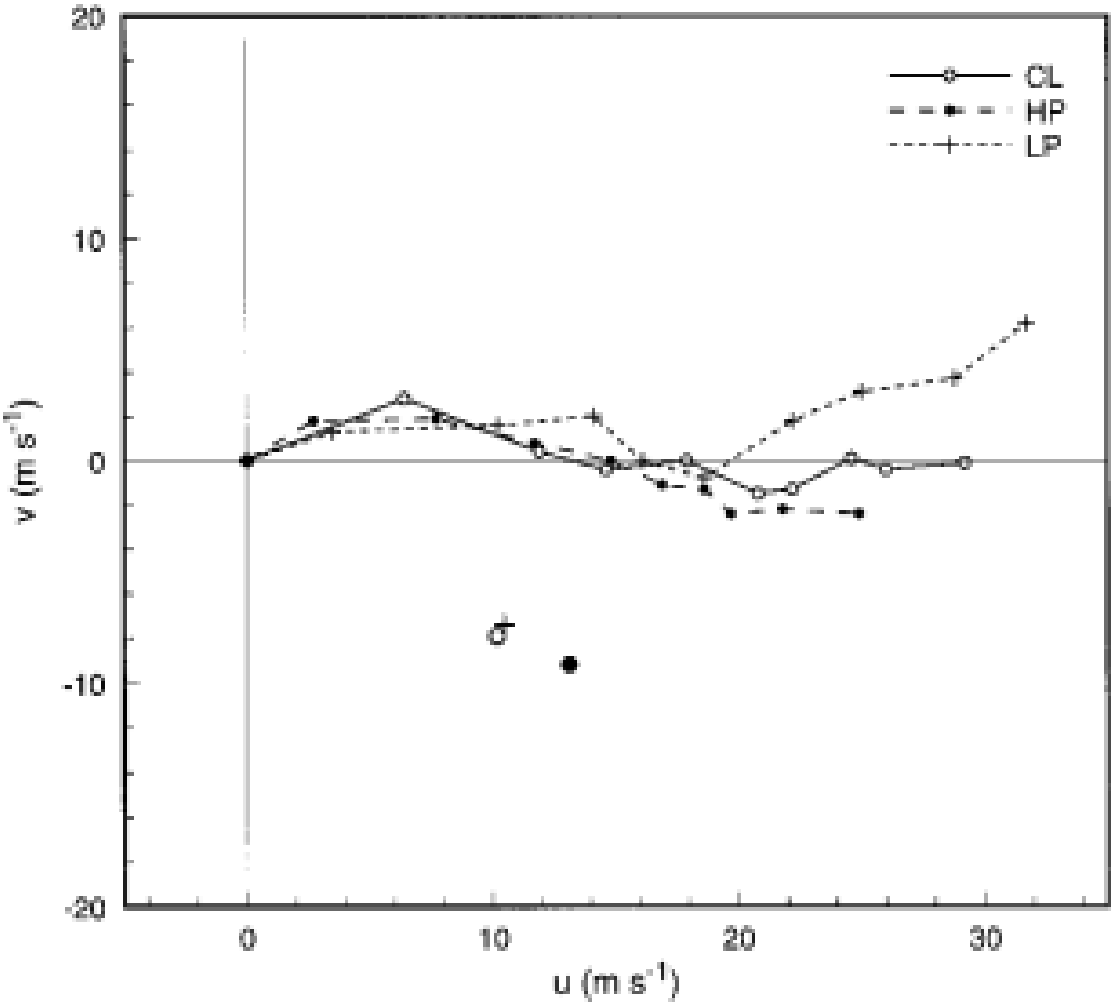

Figure 13 – Composite hodographs for LP, CL and HP cases. The hodographs were rotated to the 0-4km bulk shear vector such that it is pointing in the positive x-direction. Additionally, the boundary layer mean wind is represented as the origin. Both steps were taken prior to compositing. Adapted from Rasmussen and Straka (1998).

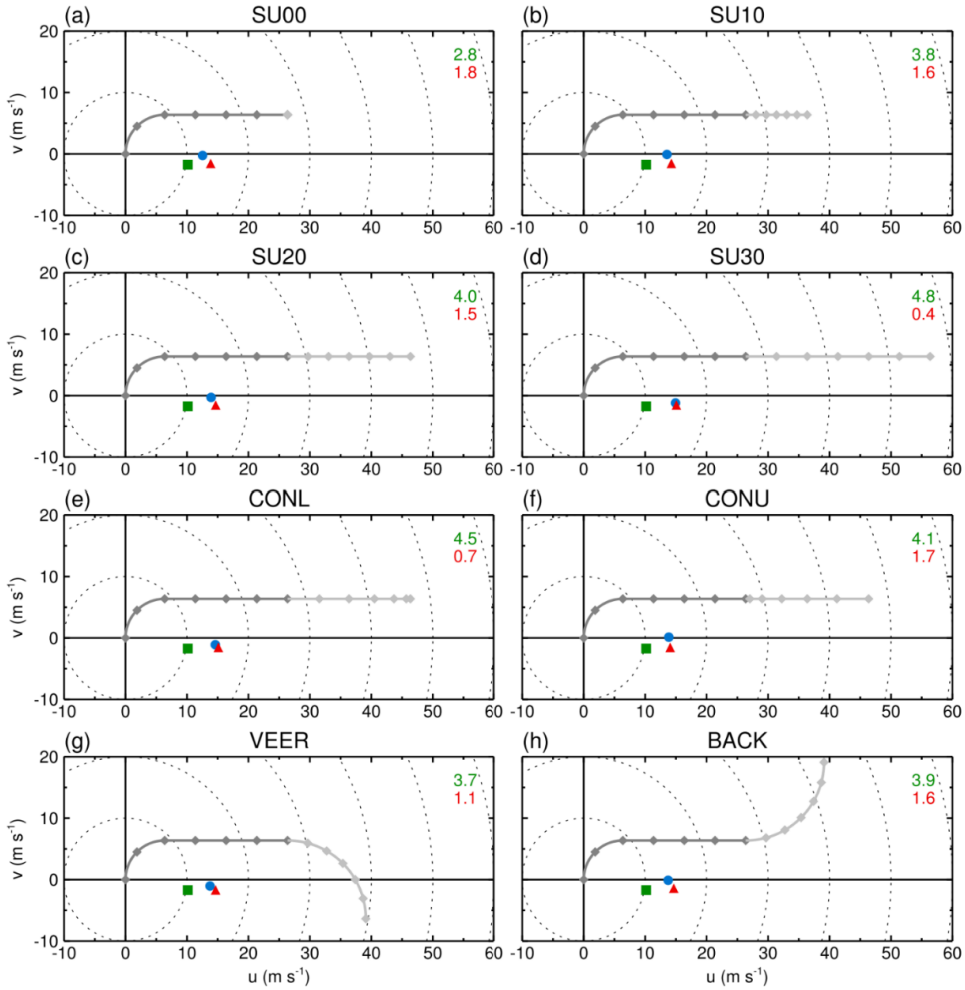

Figure 14 - Different wind profiles that were testing in the Warren et al. 2017 modeling study. All of the wind profiles represent the same low- and mid-level environment, whereas the wind profile above this level (6-12km) was varied in each of the simulations. An increasing wind shear is added to simulations a-d. The wind shear was concentrated in the lower (upper) section of the upper-levels in e (f). The wind profile was veered (backed) in simulations g (h). Adopted from Warren et al. (2017).

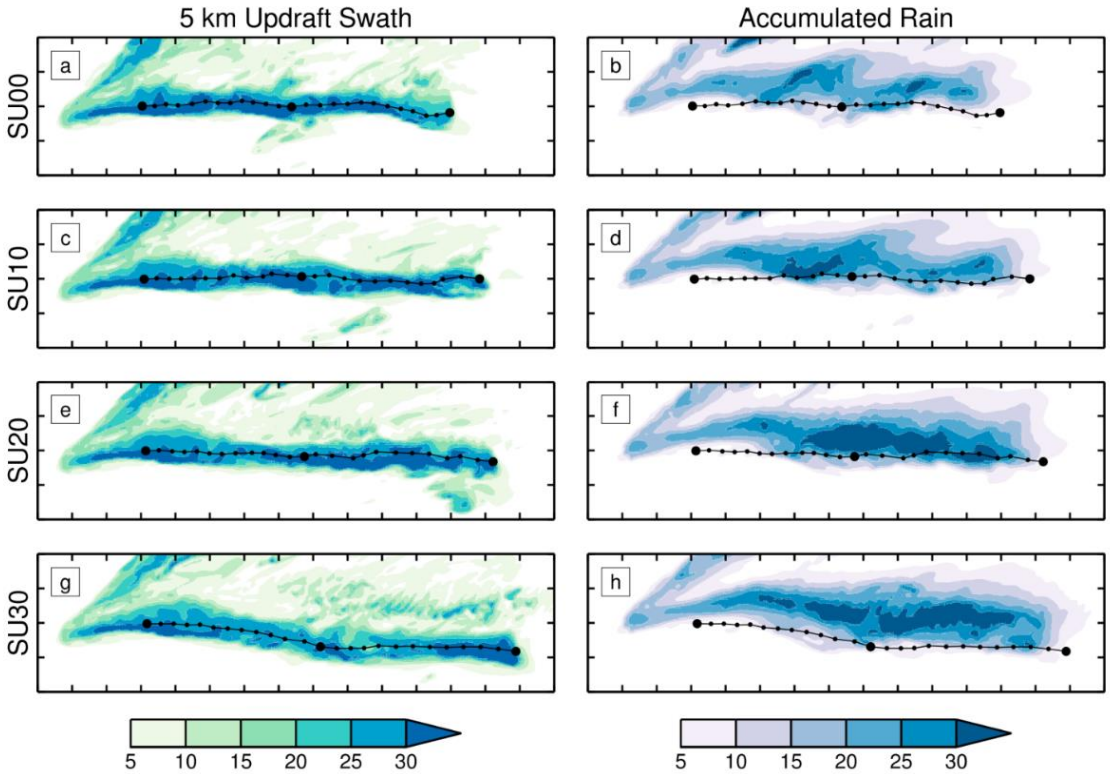

Figure 15 - The 5km updraft swath (left) and accumulated rainfall (right) for each of the storms with increasing upper level shear (top-bottom). Precipitation production increased with increasing upper level shear as did the 5km updraft swath in all but the SU30 case. Adopted from Warren et al. (2017).

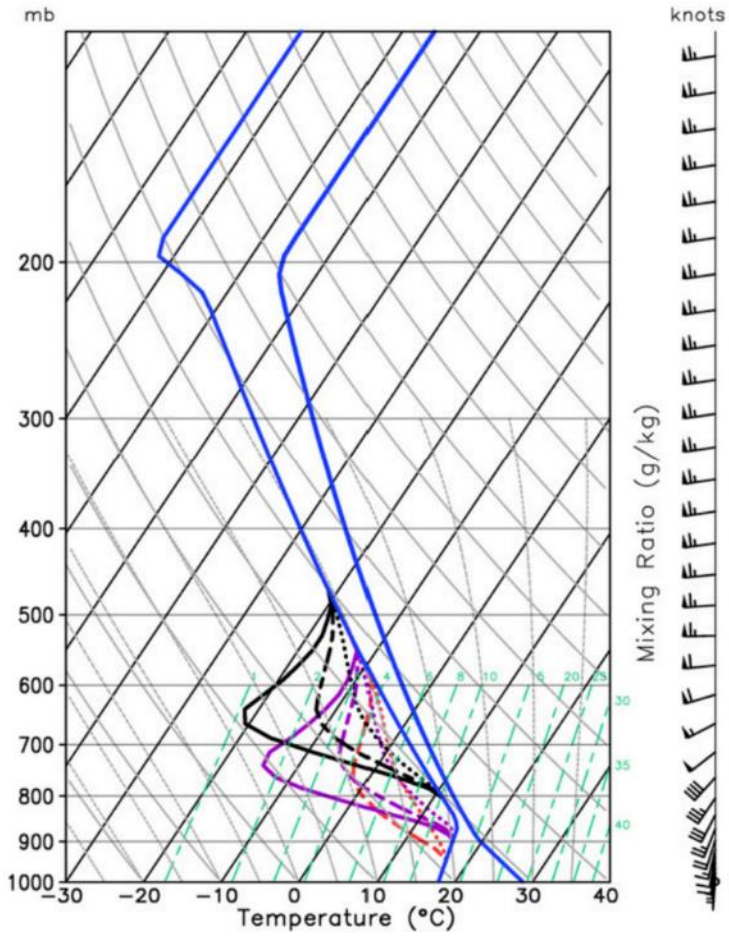

Figure 16 - The thermodynamic profiles for the simulations ran in Grant and Van Den Heever (2014). The black lines represent the highest dry air at a central location of 3.5km AGL, labeled with an 'H' in the subsequent diagram. The purple lines represent the middle dry air centered at 2.5km AGL and labeled with an ‘M’ in the subsequent diagram. Finally, there are the lowest level simulations, with the dry air centered at 1.5km AGL and labeled with an ‘L’ in the subsequent diagram. Adopted from Grant and Van Den Heever (2014).

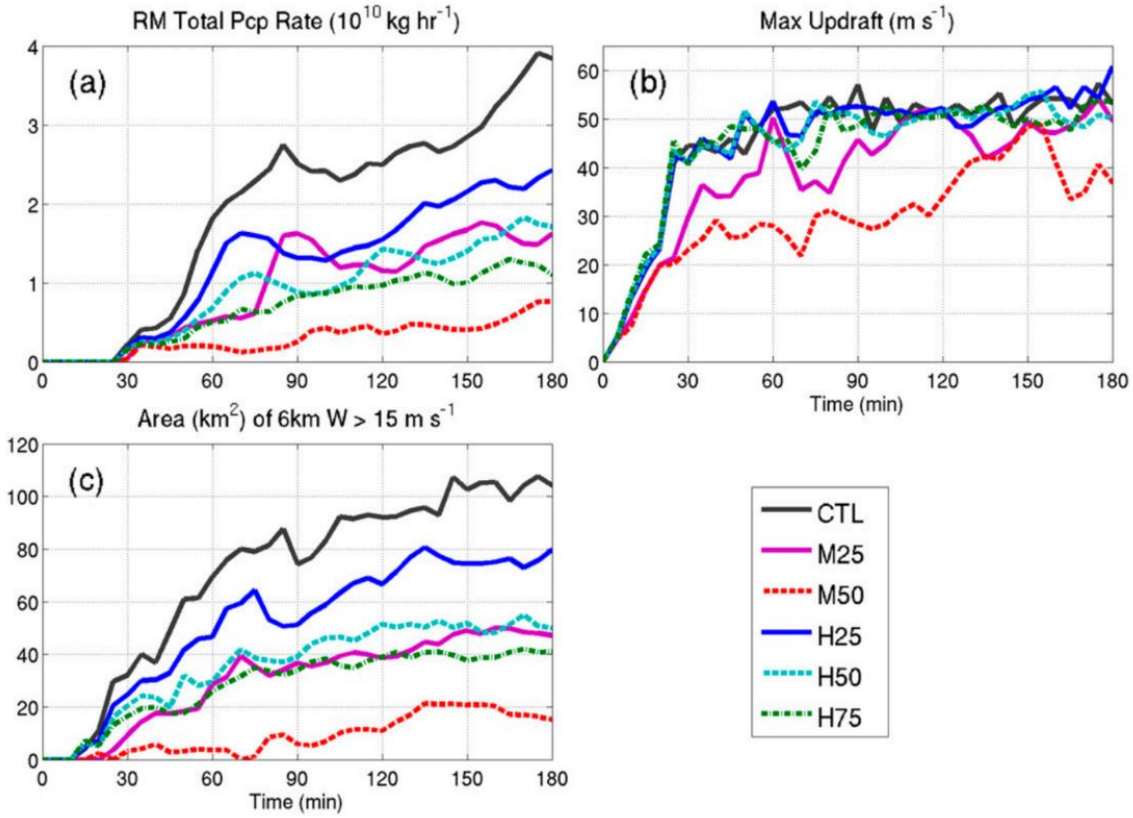

Figure 17 – The total precipitation rate (a) for each of the simulated storms, which shows a stark difference between the control simulation and any of the dried simulations. The updraft velocity (b), which remained relatively unchanged for all but the M50 simulation. The updraft area at 6km AGL where the upward velocity exceeded 15 ms^{-1} (c), again smaller in each of the dried simulations when compared to the control. The numeric labels for each of the lines represent the intensity of the drying (e.g. 25 indicates a 25% reduction in vapor mixing ration compared to the control). Adopted from Grant and Van Den Heever (2014).

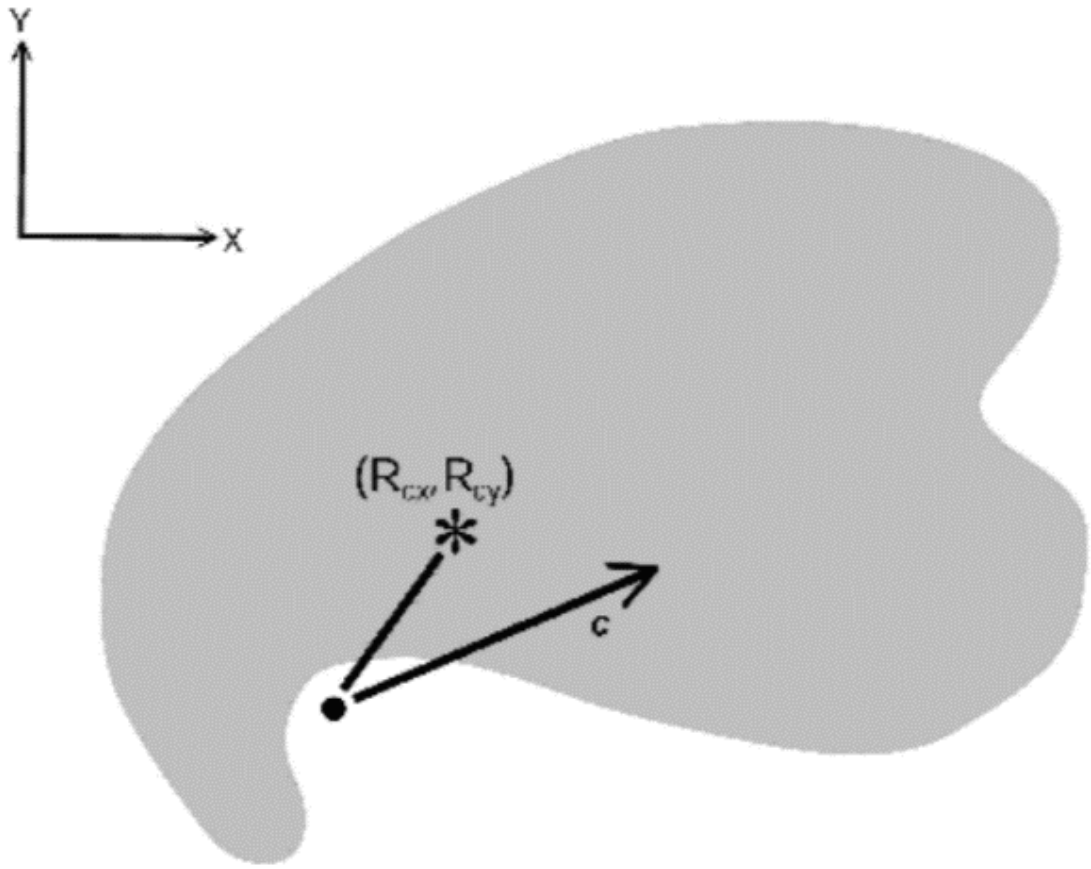

Figure 18 - A schematic diagram of the rain rate centroid (R_{cx},R_{cy}) displacement relative to the storms motion (c). Adopted from Beatty et al. (2009).

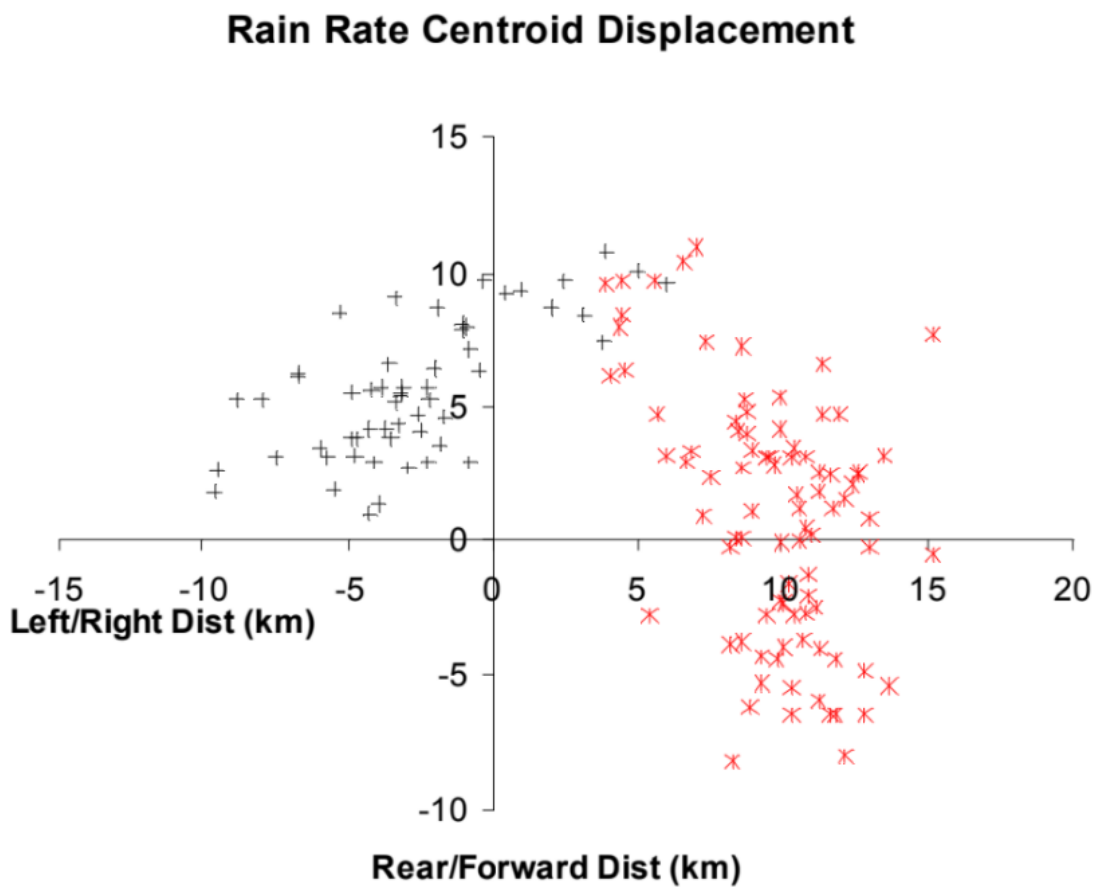

Figure 19 - The rain rate centroid displacement for HP, labeled as a black '+' and CL/LP labeled as a red 'X'. The centroids are relative to the updraft location (i.e. (0,0) on graph represents the location of the updraft). Adopted from Beatty et al. (2009).

Table 1 - List of a few significant and insignificant variables related to LP storms and other supercell storms, namely CL/HP. The parameters with an asterisk denote significance at the 95% confidence level. Adapted from Bluestein and Parks (1983).

	LP Storms	Supercell Storms	Student-t variable
Moisture Parameters			
*Precipitable water (cm)	2.8	3.3	2.43
*Mean humidity	0.59	0.67	3.42
*Mean water vapor mixing ratio in lowest km (g kg^{-1})	11.9	13.5	2.73
Thermodynamic Parameters			
*Lifting condensation level (km AGL)	1.8	1.4	2.97
*Convective condensation level (km AGL)	2.1	1.5	3.6
*Level of maximum buoyancy (km AGL)	5.6	6.5	3.4
Wind Parameters			
*Speed of mean tropospheric wind vector (m s^{-1})	14.2	20.5	4.16
*Mean tropospheric wind speed (m s^{-1})	16.8	21.7	4.52
Mean subcloud shear magnitude (10^{-3} s^{-1})	11.8	11.6	0.28
*Mean subcloud hodograph curvature (deg km^{-1})	52.9	70.5	2.83

CHAPTER III: DATA AND METHODS

The goal of this research is to identify the environmental characteristics that separate LP, CL and HP supercells into their specific categories; importantly, this effort seeks to address the discrepancies of observational (e.g., Rasmussen and Straka 1998) and modeling-based studies (e.g., Warren et al. 2017) through examination of a large observational dataset. As described in the previous chapter, there are many factors that potentially play a role in the precipitation structure of supercells. Using a large observational dataset and examining how the environmental factors co-evolve along with the storm's precipitation structure over the lifetime of a supercell, are key to enhancing our understanding of supercells, their structure, and their potential hazards. The goals of this section are to:

1) Introduce the datasets used for identifying days in which supercell's were most likely to have formed as well as their locations.
2) Objectively identify supercell precipitation archetype using similar conventions to Beatty et al. (2009).
3) Identifying appropriate locations for and analyze soundings related to the supercells of interest.
4) Determine the synoptic environments surrounding each of the supercell archetypes.
5) Identify the robustness of the tracking algorithm.

a) *Datasets*

i) Severe Storm Reports

The dataset used in this study represents a subset of the one compiled by Warren et al. (2018), which was designed as an extension of the data utilized in Thompson et al. (2012). In Thompson et al. (2012), a large number of significantly severe (hail larger than 2 inches in diameter, wind gusts greater than 65 knots, or a tornado) thunderstorm events from across the contiguous United States (CONUS) were identified. For each storm report, near-storm environmental information was collected from the Rapid Update Cycle (RUC) model mesoanalysis grids from the Storm Prediction Center (Bothwell et al. 2002) using the closest prior analysis time. The Warren et al. (2018) study limited this dataset to only right-moving supercells, interpolated the Thompson et al. (2012) soundings to a regular height grid (every 100 m between the surface and 14 km), and removed instances of soundings with low tops (lower than 14 km), missing data, low convective available potential energy (CAPE < 100 J/kg), or high convective inhibition (CIN > 250 J/kg).

In the present study, additional limitations were applied to keep the investigation tractable. Notably, the storm reports were filtered to focus on the Great Plains region of the CONUS, between 24°N and 50°N latitude and 106.5°W and 90°W (Fig. 20). This geographic limitation was applied to mitigate effects of significant topography found to the west and east of the Great Plains. Additionally, we focus only on reports from the months of March through June, when supercells are most frequent. For this study, only storms that produce a high number of reports (at least 4) were analyzed. These are selected as the ‘strongest’ events; altogether, this resulted in an initial dataset consisting

of 50 separate supercell events (i.e., dates where supercells produced a high number of reports).

ii) Radar Data

The precipitation structure of the supercells explored in this study will be identified using Next-Generation Radar (NEXRAD) Weather Surveillance Radar (WSR-88D) data. Accordingly, for the purposes of this research, only the volume coverage patterns (VCP) where precipitation was identified were used. Regarding the events identified above using filters, the radar data described below (level II and III) were grabbed for each individual event. How the data was selected varied based on the type of data being exploited and is explained in further detail below.

The level II radar data here were acquired from the National Centers for Environmental Information's (NCEI) big data archive. Their data is originally in radial form and the use of a converter tool, specifically the weather and climate toolkit (WCT) was used to convert the radial files into a gridded format for easier display and analysis of the data later. The dates and radar locations were generated as a result of storm reports in the area of interest thanks to the severe storm reports data. Level II radar data includes reflectivity, mean radial velocity and spectrum width, though only reflectivity and mean radial velocity are used here. Here, the data was acquired based on the time and location that the severe reports occurred for each event. For example, if an event lasted from 1800 UTC – 2200 UTC, then the level II data was acquired from the nearest WSR-88D between 1700 UTC – 2300 UTC so that the entirety of the event (including all storms within radar range) was captured, at least based on when severe weather was reported.

In addition to the level II data, level III data were also acquired. While level III data offers a vast range of products, there were only two distinct products necessary here. They include the storm structure (NSS) and mesocyclone (NMD) records. Within the NSS record are attributes of the storm, which include, but are not limited to its global location (latitude, longitude), its location relative to the radar (range, azimuth) and the ID number for the storm. As far as the NMD record is concerned, attributes of a mesocyclone are recorded such as its global position, its location relative to the radar, a mesocyclone ID, the ID of the most storm it is related to and a mesocyclone intensity index. The native from of these files is binary, so again the WCT was handy in converting this information into csv files for easy access to the information when tracking supercells. The data here was collected in a bit of a unique way when compared to the collection method for the level II data. For this data, it was easier to acquire the entire day's data and thus, this method was implemented. As an example, if a given event lasted from 2200 UTC on one day until 0200 UTC on the next, then the entire day's data for both dates was acquired.

The tracking of the individual storms in the level III data is done using the Storm Cell Identification and Tracking Algorithm (SCIT) as designed in Johnson et al. (1998). While not a perfect storm tracker, it is worth noting that this algorithm correctly identified and tracked greater than 90% of all storm cells correctly. As it relates to the identification of the mesocyclone, detection is a little degraded compared to that of the SCIT algorithm; however, the detection of only cyclonic vortices is applied in the algorithm (Stumpf 1998). Thus, only right-moving supercells are detected by the algorithm, which is important to keep in consideration through the methods as well as the results and discussions section.

iii) Model Data

Between 2008 and 2015, several iterations of storm-term numerical models were available to help describe the near-storm environments of the supercells in this study. Such models include the Rapid Update Cycle (RUC) 20-km model, the RUC 13-km model, as well as the Rapid Refresh (RAP) 13-km versions 1 and 2, which were relevant to the study from March 2008 to October 2008, October 2008 to April 2012, May 2012 to February 2014 and February 2014 to the end of dataset (June 2015), respectively. This led to some hardships when extracting relevant data from the models.

Additionally, the storage method for this data also changed throughout the timeframe from grib1 files to grib2 files, which ultimately changed the name of the variables within the data itself. Finally, in 2014, the RAP 13-km model was updated in February to version two of the model, which again changed the structure of some variables while deleting others. From a programming standpoint, this made it very difficult to extract data from the respected file as names and structures of variables frequently changed.

All the models included 37 sigma levels ranging from 1000 hPa up to 100 hPa in 25 hPa increments. At each sigma level, data such as geopotential height, temperature, relative humidity, the zonal wind component and the meridional wind component were recorded. In addition, surface information of these specific variables was also recorded at each grid point. Other calculated variables also exist within the models which include various forms of Lifted Index (LI), CAPE and CIN, among others, though most variables necessary for analysis were calculated following the capture of soundings as specified grid

points. Finally, as implied in the names of the models discussed earlier, the spatial resolution of the models ranges from 13-20 km, while not the best for mesoscale analysis, it is the highest resolution available for the given dates.

iv) Reanalysis Data

In order to understand the synoptic patterns that correspond with each precipitation archetype, additional data was needed. While it is relatively straightforward to create a simple average composite map for the supercells in each identified precipitation category, the fact that the supercell events span over four months (March – June) and that synoptic patterns lend themselves to shifts over this timeframe, anomaly maps would produce a cleaner and more appropriate map for interpretation. An anomaly is simply the deviation of a value based on what is expected from the given base period. More details regarding the composite anomaly maps will be discussed in the methods section under the synoptic environment sub-section of this chapter.

To create these anomaly maps, the ERA5 reanalysis dataset (Hersbach and Dee 2016; Copernicus Climate Change Service 2017) was used to identify a base period for the anomalies to be calculated from. This dataset has a temporal resolution of an hour making it ideal to use since it lines up with the temporal resolution of the RUC and RAP model data. Since the hourly ERA5 data goes back to 1979, the base period was identified as being from 1979 – 2007, which is outside the range of the severe storm reports dataset. The data that is important here are the days and hours in which a supercell was ongoing to get the most accurate comparisons for the anomaly maps. For the purposes of this study, only the geopotential height at 300 hPa, 500 hPa, 700 hPa and 850 hPa was

obtained, which are common mandatory levels in soundings. With regard to horizontal resolution, this dataset is on a 0.25° x 0.25° grid, making it relatively the same scale as the lower resolution, 20 km RUC and RAP models. The format of such data is grib2, allowing for similar coding convections as the RUC and RAP model data to be used.

b) Methods

Following identification of the 50 events for analysis, the raw severe storms data over the previously determined geographic and temporal domains (Fig. 20) needed some type of structure added to it to pick out individual supercell storms. The idea for the events was to try and find the reports that were clustered in some way that may resemble a supercell storm track. To do this, the raw severe storm report data was grouped such that all the reports that landed within 75 km of each other and were an hour or less apart were considered a storm (Fig. 21). While this is far from a sophisticated approach it was able to provide a general idea of which dates to look at in which storms were frequently being reported as severe, hence the previous identification of these storms as the 'strongest' storms within the dataset.

i) Cell Tracking

With all the event dates identified via the storm track, it was time to use the appropriate data and try and track supercells. For each of the events, the same tracking method was used, and it included using a combination of level III NSS and NMD data. The information in each of these datasets was defined as having a storm ID which is the key linking feature between the two, level III products. Before any tracking could begin though, only data that lay inside 125 km from the radar location were kept as to keep the

base scan from exceeding 2.0 km AGL, as in Beatty et al. (2009). While this limited the range of storms that could be tracked, it ensured that only the low-level precipitation structure would be examined for proper identification. An overview of the tracking algorithm is illustrated in Fig. 22.

Identifying which storms were supercells was the next important task. This was aided by linking features related to the storm id and mesocyclone id level III products. Note, however, that a particular storm can be identified as having many mesocyclones not only over the course of its lifetime, but also within the same analysis time. Table 2 shows an example of this issue in a glorified version of the data and in this case, one particular storm was identified as having three possible mesocyclones. Knowing this could not be the case, it was necessary to pick the most likely mesocyclone for this particular storm at this time. To do this, the mesocyclone that was the strongest, via the mesocyclone intensity (MSI) column, and the closest to the storm of interest, but no greater than 15 km, using the great arc distance between locations of the mesocyclone and storm was used.

If a given SCIT id was not listed in the NMD product, then it was not tracked since it was lacking one of the most important characteristics of a supercell, the rotating updraft. In this case, that SCIT id was just simply passed by at that time. Only products with the same time were used simultaneously so that there was no confusion in tracking. However, once a storm was identified as a supercell, it was added to an archive with its respective data. This process was continued for all the times within the current event.

To account for any potential cycling of the mesocyclone (e.g., Burgess et al. 1982), a buffer time of 30 minutes was used in case a lack of a mesocyclone was identified at intermediate times throughout a supercell's lifecycle. In addition to this, if a SCIT id was re-used later for a given event, then this buffer time helped to distinguish two separate cells. In the end, only cells lasting at least an hour were used to allow for multiple model times to be used for environmental data, this way an evolutionary standpoint could be implemented for each storm.

After running the tracking algorithm across all 50 event dates, a total of 104 individual supercells were identified, which again all had a duration of at least one hour. This led to a total of 330 analysis hours across all the supercells tracked.

ii) Objective Identification of Precipitation Mode

At this point, supercells were identified via their SCIT id and mesocyclone id but did not have any association as to what type of supercell they most likely were (LP/CL/HP). This stage required a multi-step process, first identifying the reflectivity core location relative to the storm's mesocyclone, then taking a subset of the tracked cells and objectively identifying them as a specific precipitation mode. The final step was to identify patterns in the objectively identified precipitation modes and correctly label the other tracked cells in their respective categories.

In the identification of a storm's reflectivity core location relative to that of its mesocyclone, a process like the one found in Beatty et al. (2009) was used. First, a linear regression of the reflectivity centroids was used to identify an average track bearing and speed. This included only the times in which a supercell was identified as having a

mesocyclone; the in-between stages, when a cell did not have an associated mesocyclone, were not kept. The biggest difference between Beatty et al. (2009) and this method is the identification of the reflectivity centroid. Note that Beatty et al. (2009) used only the base scan and an arbitrary storm boundary to find their reflectivity centroid, whereas the present study makes use of the NSS product, which uses the SCIT tracking algorithm and utilizes multiple elevation scans to more accurately identify cells, particularly their location. Regarding the linear regression, this was used as the average forward motion and is important later for the identification of a storm's precipitation mode.

To identify a storm's reflectivity centroid location relative to the mesocyclone, the average bearing of the storm found via a linear regression was used and 'attached' to the mesocyclone (see Fig. 23 for a conceptual model). This put all the storms in the same reference frame so that they can easily be identified together. For locating the reflectivity core locations on such a diagram, the distance between the mesocyclone and reflectivity location had to be calculated, broken down into their x- and y-components and finally, rotated to the bearing of the cell, thus all storms fit on this conceptual layout (Fig. 23) while remaining in the same reference frame.

Due to the imperfect nature of the identification of the mesocyclone and reflectivity locations by the NMD and SCIT algorithms, respectively, as well as scan-to-scan variations in storm structure, there was variation over time with respect to the exact location of the cell reflectivity core in relation to its mesocyclone. As a result, the mean reflectivity core location was used for each cell in the identification of the cells precipitation mode over its lifetime. While it is known that cells can evolve from one

precipitation mode to another, only the predominant precipitation mode will be used in the analysis of each storm for simplicity.

With all the storms identified as having a mean location for the reflectivity core over its lifetime, some guidelines had to be put in place for identifying which precipitation archetype a specific storm fell within. To do this, a subset of the tracked storms was chosen and subjectively identified as one of the precipitation classifications. Given the findings of Beatty et al. (2009) and the similarity of the present radar-identification algorithm to that study, storms were only identified as HP or CL/LP based on their low-level reflectivity echo. This step was completed using the previously acquired level II radar data. The data was displayed using GR2Analyst and a specific cell was identified using its respective latitude and longitude location. A total of 10 randomly chosen storms was subjectively analyzed using this method and identified as being either CL/LP (7) or HP (3). From here, an average displacement along the x and y directions were calculated for each of the archetype (HP or CL/LP) and a significant difference was found in the x direction between the two archetypes. While this difference was found using a small sample size, it is important to note that the visual difference between the two archetypes is striking (Fig. 24) and brings credence to the significance of the difference. In addition, the angle of the average reflectivity core location for each storm was calculated and averages were calculated for each archetype, again a significant difference was obtained. The angle of the reflectivity core location is simply the theta difference between the location of the reflectivity core with the storm motion vector. This can be easily calculated given the x and y coordinates of the reflectivity core location (Fig. 25). In Fig. 24, it is evident that the

better method to choose from here is the x-displacement as the overlap between the two boxplots isn't as much in this graph when compared to the core direction.

The displacement of the core was used to expand this information to the rest of the dataset. To do this, knowing the mean and standard deviation of each of the archetypes was a necessity so that an intersection point between the two distributions could be calculated. Estimating the distributions to be Gaussian gives two formulas with two unknowns and thus the intersection points could be calculated from the distributions. Given the complex nature of the formula for the Gaussian curve, the formula for the intersection points will not be shown. After applying the core displacement threshold determined from the random sample, the algorithm then identified a total of 38 HP storms and 66 LP/CL storms. An interesting note is that most of the storms identified for a specific event had the same archetype.

iii) Tracking Algorithm Sensitivity Testing

The objective identification of the precipitation mode, while following closely to the Beatty et. al (2009) method, does warrant further testing to identify sensitivities in how the storms were binned into their different categories, particularly given the small sample size of the subjectively identified storms. To test the sensitivity of the tracking algorithm, the intersection of the distributions regarding the x-direction of the core displacement needed to be identified and from there, it was varied by adding to or subtracting from that intersection point. Three variations to the intersection point were examined, including adding 2 km and subtracting both 1 and 2 km. Using these new intersection points, the storms were then re-classified. From there, the distributions of

environmental parameters were compared among the sub-groups to determine if the results were sensitive to small changes in the thresholds used for classifying the storms.

iv) Sounding Acquisition

The soundings were acquired using previously gathered model data. To do so, first the location of the tracked supercells had to be modified slightly such that the location of the storm at the "on the hour time" was acquired. For example, if the closest radar observation time was at 22:54 UTC, then the storm had to be progressed six minutes using its average motion vector to get the most accurate result for the storms location at the on the hour time. This is important so that the updraft location and thus the inflow region was 'known' to a relative degree of accuracy for the given storm for the proper acquisition of a sounding. The storm location as identified by the SCIT algorithm was used here as the storm location prior to adjusting it to the "on the hour time".

Once the storm's location is known as it relates to the model time, then the closest point in the model needed to be chosen. With some simple geometry, it is known that the largest discrepancy between the storms location and the model location is the central location between four adjacent grid points, which works out to be 14.14 km at a 20 km grid spacing and 9.19 km at a 13 km grid spacing; this is relevant to the inflow point chosen for the storm.

The inflow point was selected at a 90° angle to the right (clockwise) of the storms motion and a distance that falls within the 'goldilocks zone' (40-80 km) as described in Potvin et al. (2010; see Fig. 26). The right turn was utilized due to all the tracked storms being right-moving supercells; this means that the clockwise rotation would put the

sounding location into the warm sector and inflow of the storm. To combat the effects that localized perturbations in temperature, dew point, wind, etc. could have with grabbing a single sounding, the central location of the 'goldilocks zone' (60 km from the storms inflow location) was chosen and adjacent points were also initially acquired for potential inclusion in an area averaged sounding (Fig. 27), as suggested in Parker (2014). However, before including a vertical profile in the averaged sounding, a few additional steps were taken. First, a check for precipitation contamination was conducted. If the precipitation rate was a value other than zero, then that grid point was not used in the averaged sounding. Secondly, the distance of the grid point to the storm of interest was examined. A grid point was only used it if was not too close (< 40 km) or too far (> 80 km) from the storm. After these steps, an averaged sounding was computed. Based on the above criteria, an averaged sounding could be based on a minimum of one up to a maximum of nine locations. The minimum arose in a couple of situations, the first being the situation where there was precipitation at all of the grid points within the 'goldilocks zone', so the point with the lowest precipitation rate was chosen out of necessity for a sounding location. The other situation arose when all but one grid point within the 'goldilocks zone' recorded precipitation. This process was completed for each hour over each of the storm's lifetimes, thus creating multiple area-averaged soundings for each storm.

With the area averaged sounding acquired for each of the storms, the calculation of sounding related variables needed to be carried out. These include, but are not limited to, multiple forms of CAPE and CIN (i.e., surface-based, mixed-layer and most-unstable),

shear to/from multiple levels (i.e., 0-1 km, 0-3 km, 0-6 km), storm-relative helicity (i.e. 0-1 km, 0-3 km, 1-3 km) and precipitable water.

At this point, all the storms have been tracked via a tracking algorithm that was developed to partially relate to the Beatty et al. (2009) tracking algorithm. In addition, the storm mode identification was in close relation to that of Beatty et al. (2009) and similar to their findings, only two distinct modes were able to be identified with the tracking algorithm developed herein. Furthermore, with tracked storms identified as one of two distinct precipitation modes, soundings and other parameters could now be related to those specific storms for further analysis in the subsequent chapter.

v) Synoptic Environment

Given that the ERA5 dataset covered the globe, it needed to be trimmed to only include the point over the contiguous United States, effectively having the same domain as the RUC and RAP models. Then, since the datasets had different spatial resolutions, some with 13 km grid spacing, some with 20 km grid spacing and the ERA5 dataset with 0.25° grid spacing, accurate comparisons can only occur when the grid points line up with each other, so all of the datasets were re-gridded such that they all had the same number of data points and locations as the lower resolution 20-km RUC and RAP models. The re-gridding process was completed using an interpolation scheme from a module in python called SciPy (Oliphant 2007). The linear interpolator is used for estimating values at unknown locations.

With all of the dataset on the same grid, in order to appropriately identify shifts in the synoptic pattern from the ‘normal’ pattern, a base period for each of the days of

interest needed to be created. To do this, a mean and standard deviation needed to be acquired for each date of interest over the years from 1979 – 2007. Once these were calculated, they could be used against the environments specific to each of the supercell archetypes. The anomaly for each point of interest was calculated as:

$$Anomaly = \frac{X - \mu}{\sigma} \tag{3}$$

where X is the geopotential height at a given grid point, μ is the mean over the base and σ is the standard deviation over the base period, both at the same grid point. The anomalies were then calculated over the entire domain and for each of the pressure levels of interest (300 hPa, 500 hPa, 700 hPa and 850 hPa).

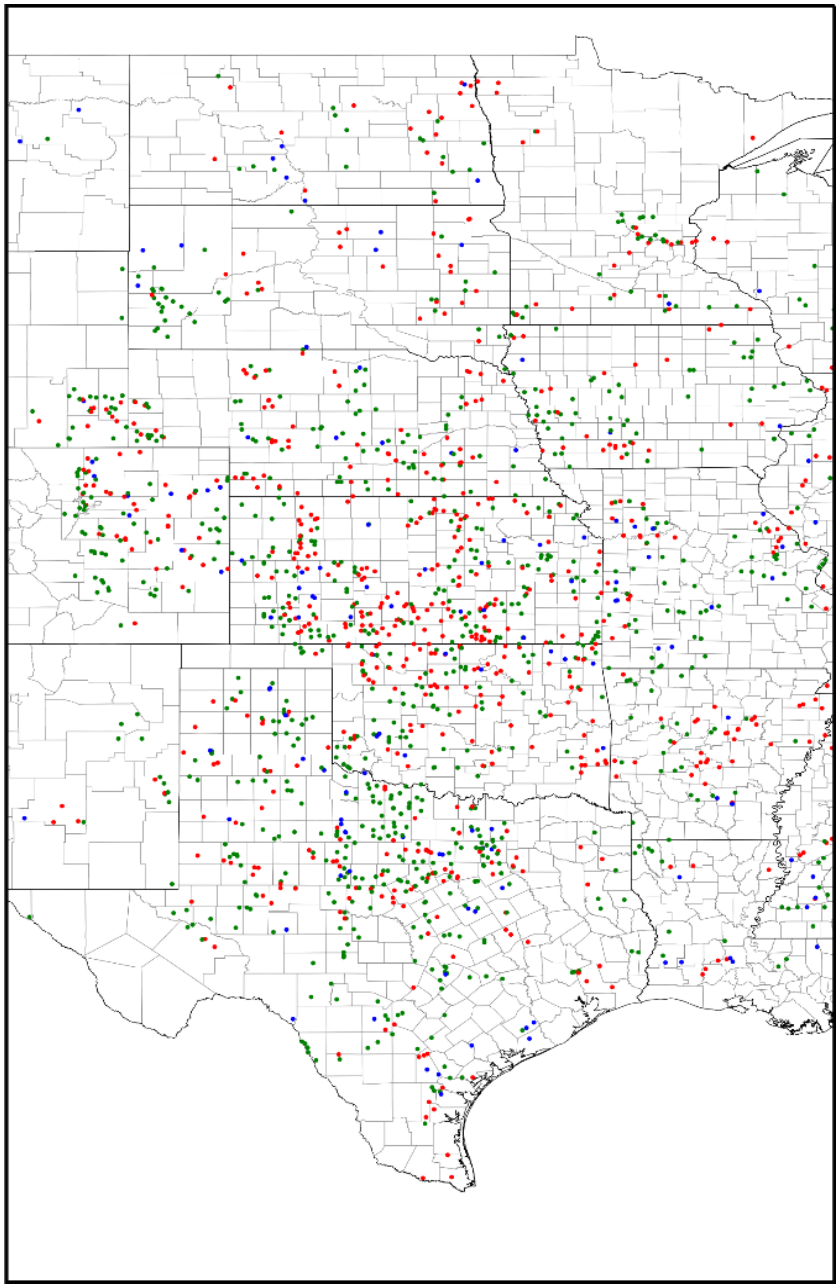

Figure 20 - Study area for the given research. All reports presented occurred from March - June. The study domain consists of latitudes from 24°N to 50°N and longitudes from 106.5°W to 90°W. Blue, green and red dots represent wind, hail and tornado reports reported to the SPC.

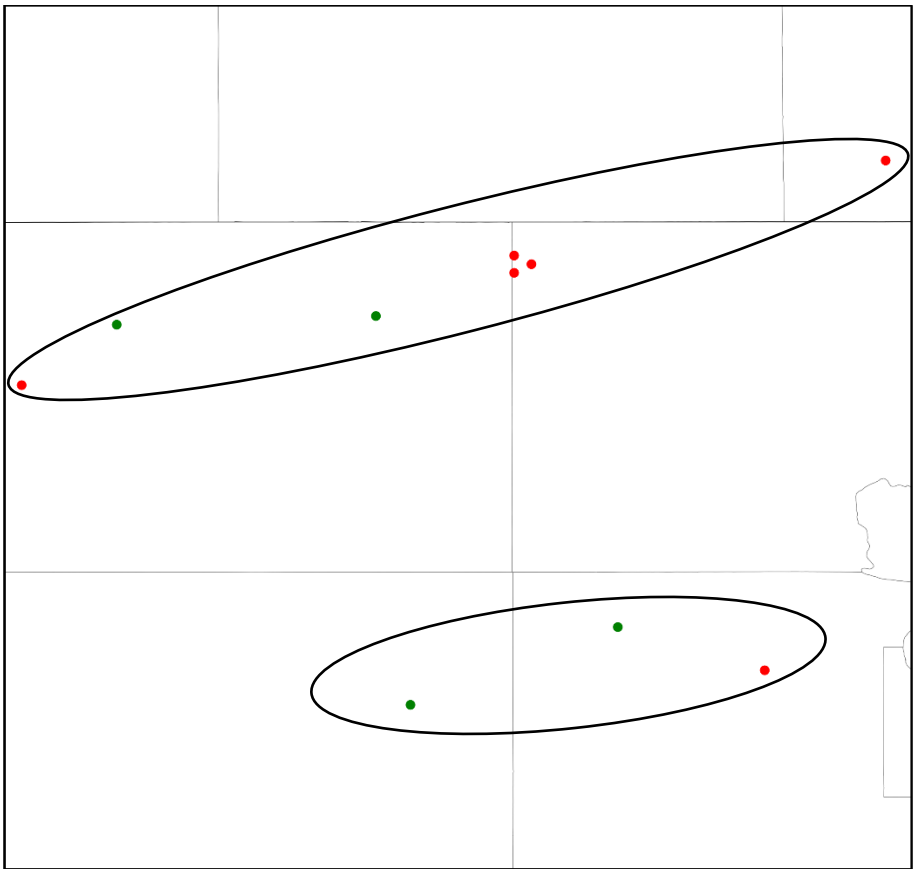

Figure 21 – Severe reports for Storm 287. Green and red dots represent hail and tornado reports, respectively. Although identified as one 'storm' clearly there are two apparent storm tracks here, one in the northern area of the frame and the other in the southern area of the frame.

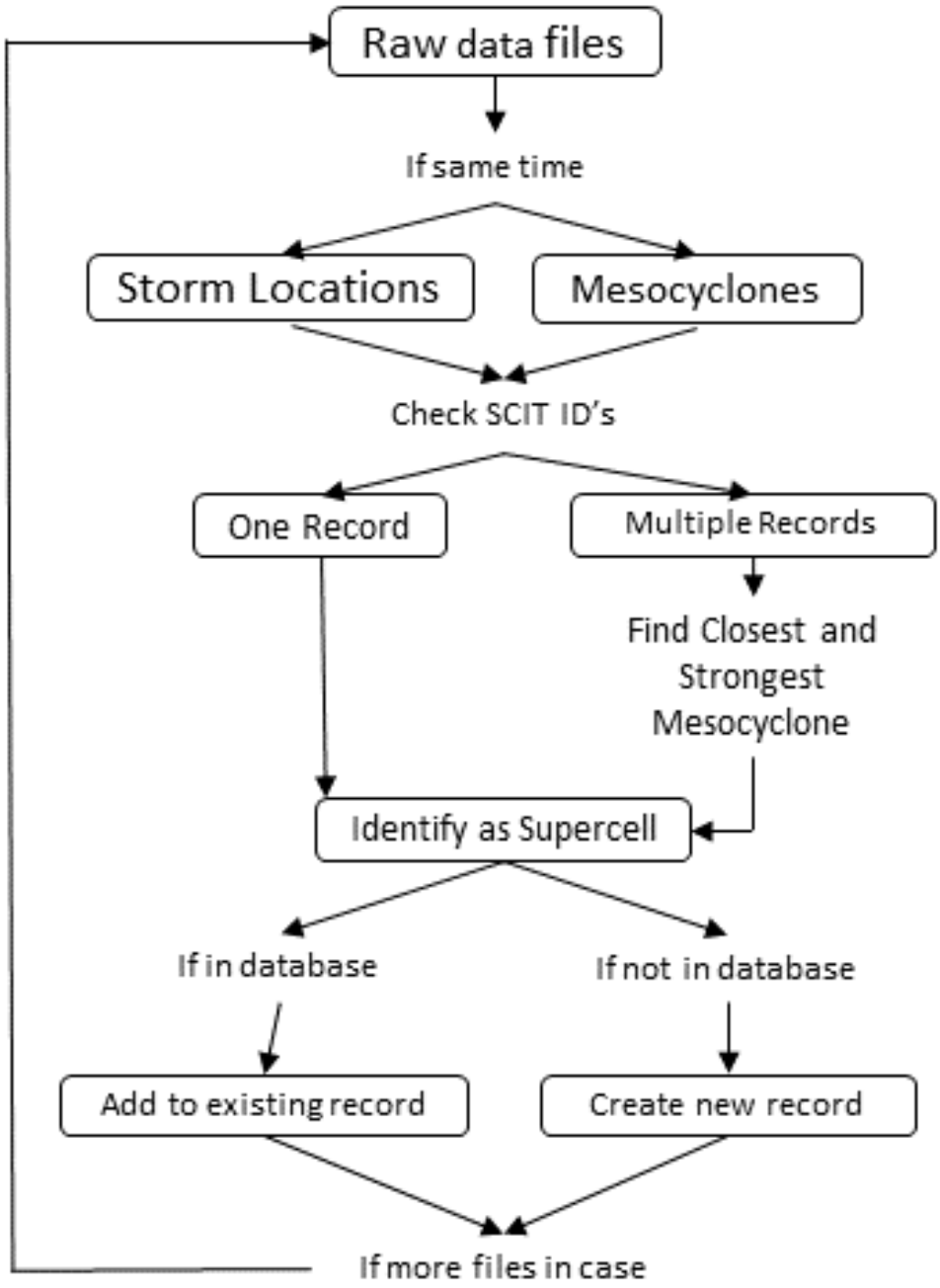

Figure 22 - A flowchart of the methodology used in tracking supercell using Level III radar data, specifically the NMD (labeled Mesocyclones) and the NSS (labeled Storm Locations) products.

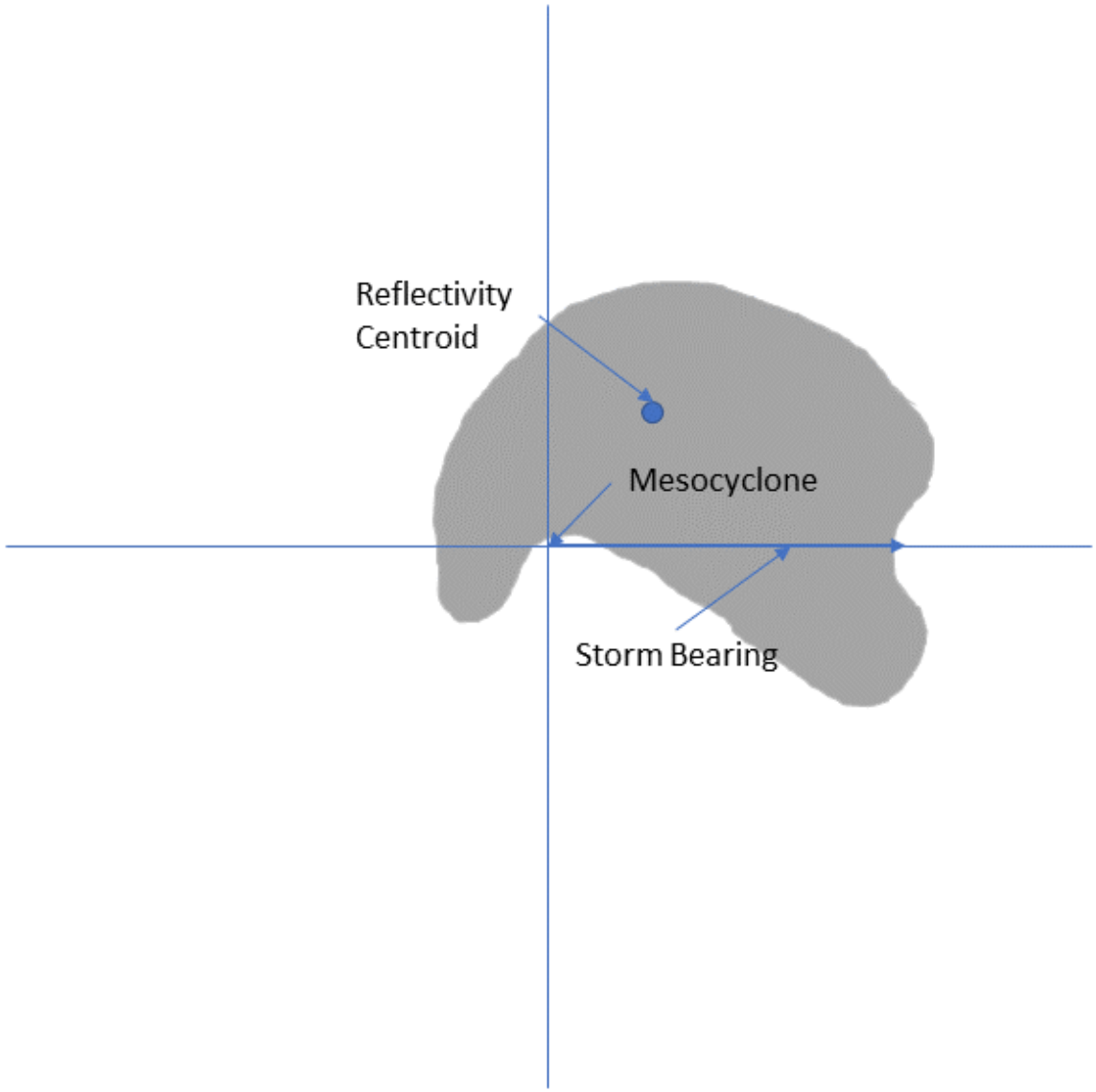

Figure 23 - A conceptual diagram of a supercell that is superimposed on a set of axes in which its propagation is labeled in the up direction. The center of the mesocyclone represents the origin, the reflectivity centroid as suggested by the SCIT algorithm is the blue dot and the gray polygon represents the low-level reflectivity echo boundaries of a supercell.

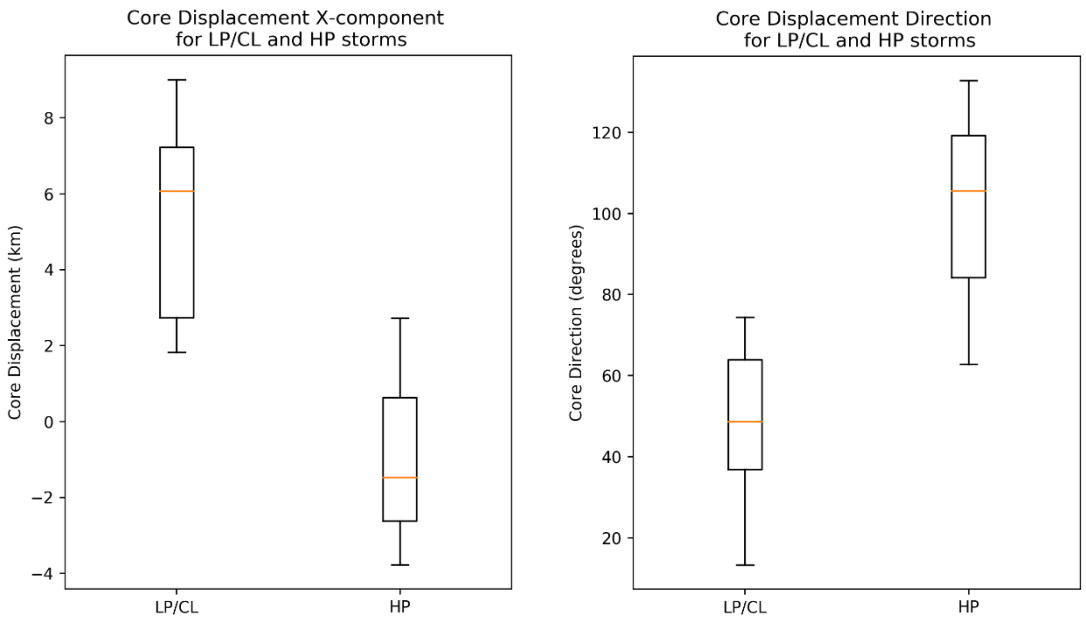

Figure 24 - The distribution of the core displacement for the HP and LP/CL storms which were subjectively identified. The x-component of the core displacement (left) shows a rather significant difference for each archetype. The core displacement direction (right) again shows a significant difference between the two archetypes.

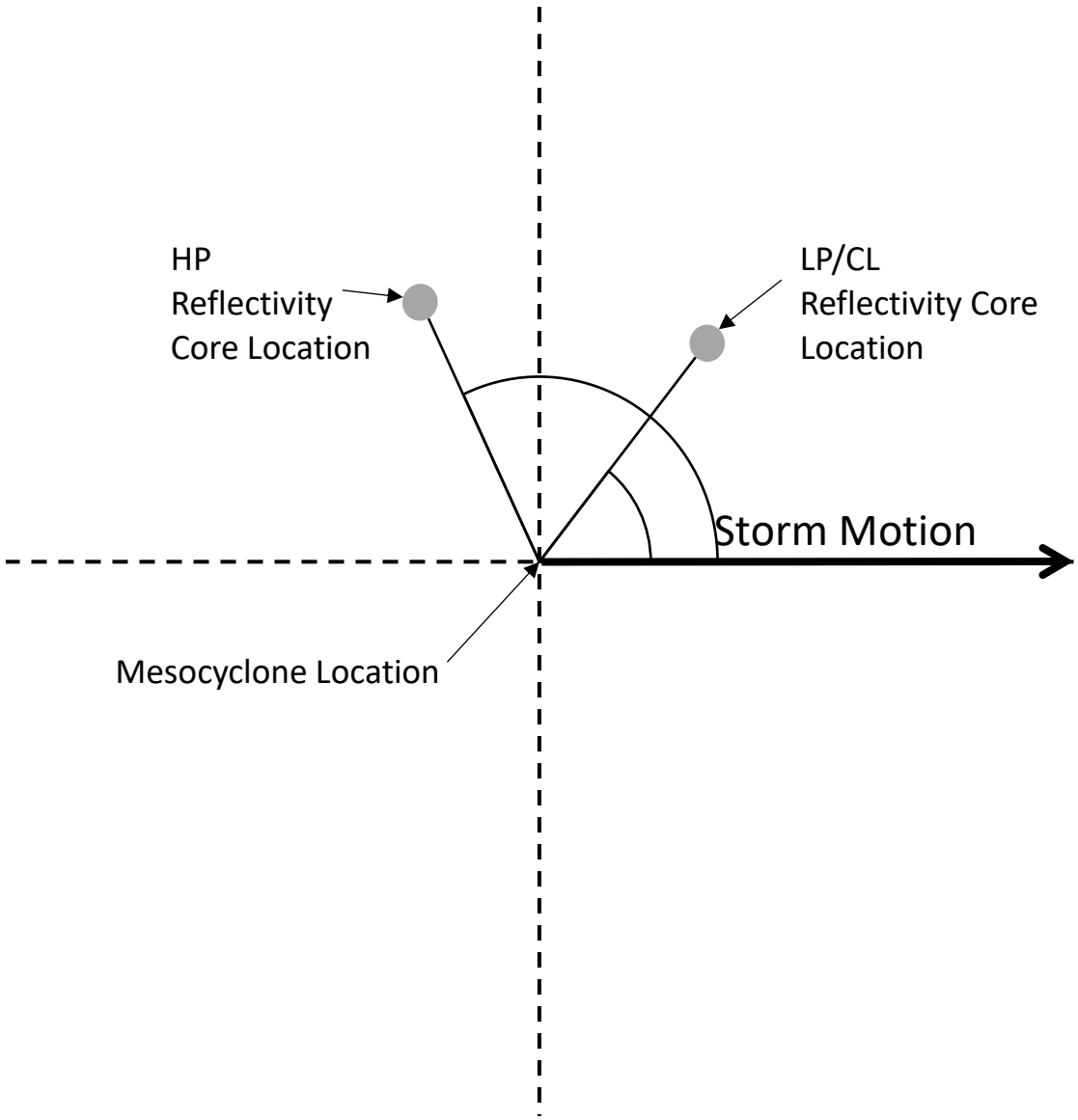

Figure 25 – A schematic diagram depicting how the angle of the reflectivity core location was calculated. The gray dots represent the approximate LP/CL and HP reflectivity core locations. The mesocyclone location is represented as the origin of the graph. The black solid line represents the direction of storm motion and finally, the arcs represent the angle the reflectivity core makes with storm motion vector. A larger angle would represent a more HP like appearing storm and vice versa.

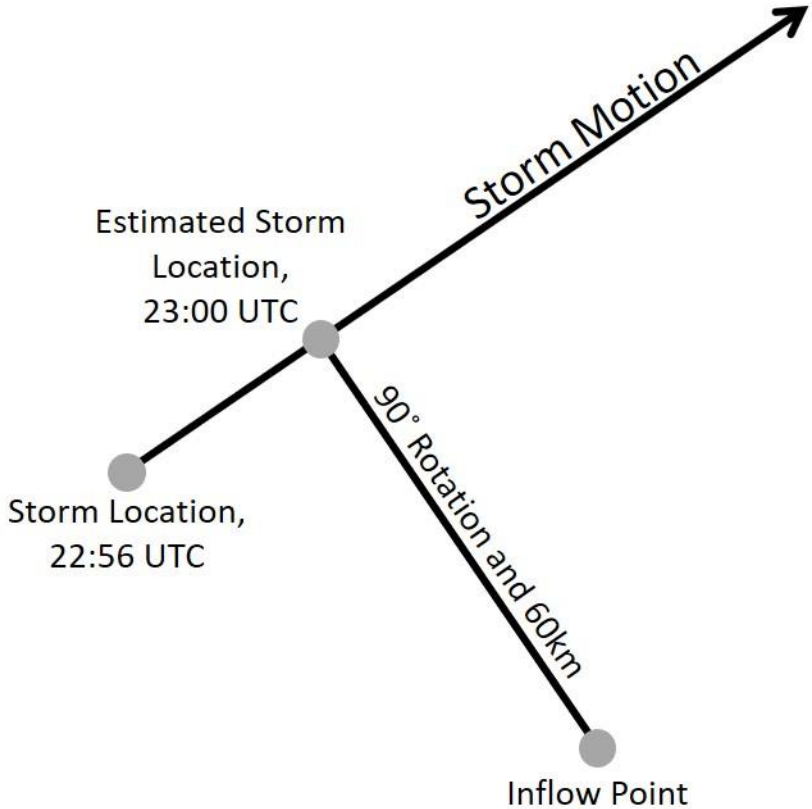

Figure 26 – A schematic diagram denoting the location of the inflow point in the model given the storm location that represents the storms location that is closest to an hourly observation. The estimated storm location is then rotated 90˚ clockwise and proceeded 60km out from the storm and the closest model point to this location is then labeled as the inflow point.

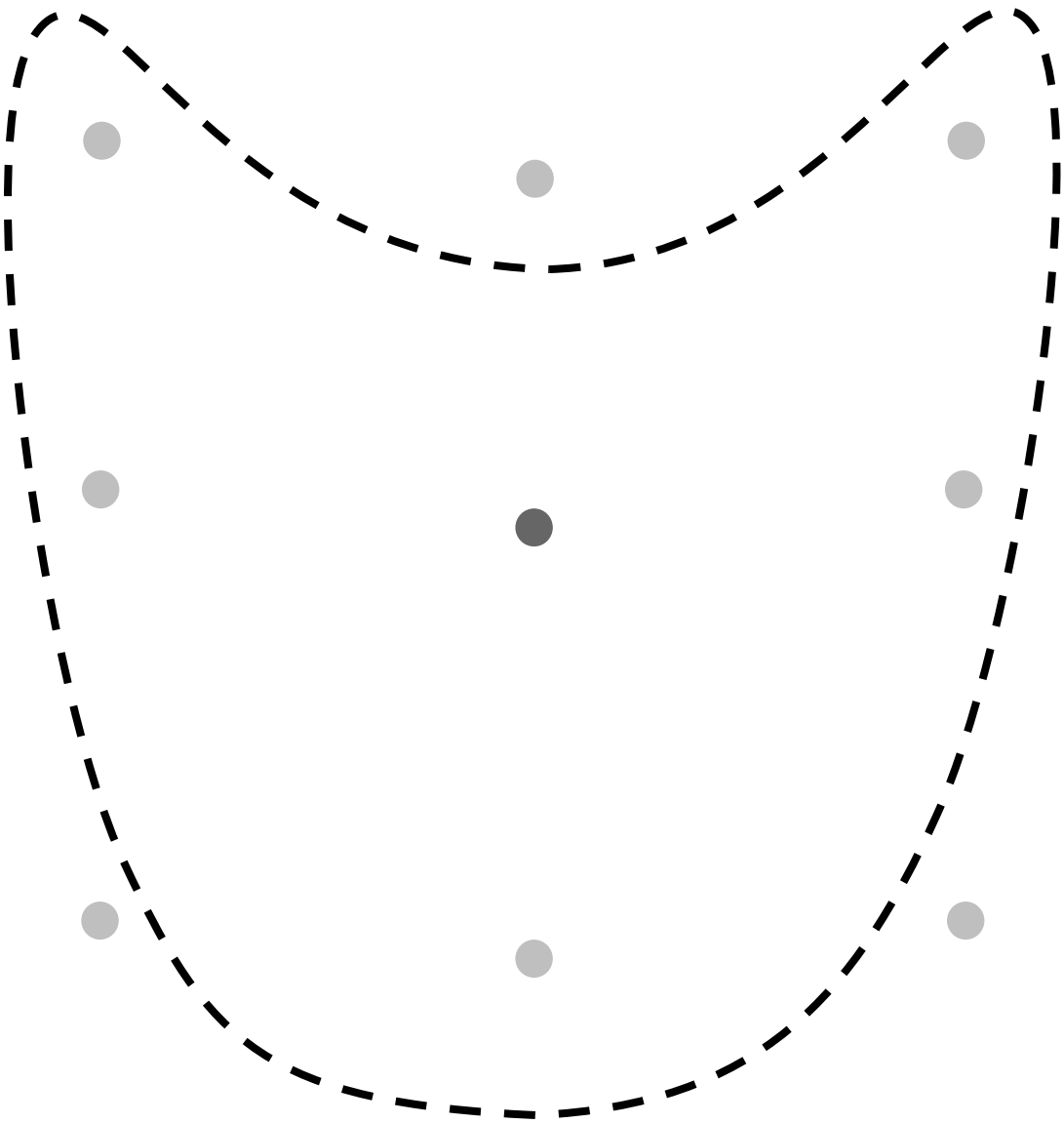

Figure 27 – A schematic diagram denoting how an area averaged sounding was acquired. The dark and light gray dots represent the inflow point and adjacent model points, respectively. In addition, the dashed polygon represents the 'goldilocks' zone and depicted in Potvin et al. (2010). The storms location is denoted as being directly above the figure. Only the points inside the polygon were considered for the area averaged sounding, assuming no precipitation was occurring at those locations.

Table 2 - An idealized representation of a case where one cell was identified as having more than one mesocyclone. The scit_id column proves this with all showing T7 as their parent storm.

wsrid	datetime	lat	lon	id	range_nm	azim_deg	str_rank	scit_id	tvs	motion_deg	motion_kts	msi
KDDC	5/24/2008 01:44	37.573	-99.207	76	38	107	8	T7	N	230	24	4978
KDDC	5/24/2008 01:44	37.683	-99.198	43	37	97	6L	T7	N	209	26	3874
KDDC	5/24/2008 01:44	37.593	-99.287	274	34	107	5	T7	N	150	15	3303

CHAPTER IV: RESULTS AND DISCUSSIONS

The results presented herein will address several components of this research: 1) Identify the similarities and differences between the semi- objective tracking algorithm as described in the previous chapter and the one developed in Beatty et al. (2009), along with the sensitivity of this tracking algorithm; 2) Highlight broad climatological differences between each of the supercell regimes (e.g., synoptic patterns, geographical locations); 3) Identify key environmental differences (both thermodynamic and kinematic) among the precipitation classification categories, and describe how these results compare to previous ones such as Bluestein and Parks (1983), Rasmussen and Straka (1998) and Warren et al. (2017); and 4) Identify physical explanations as to why the results present themselves as they do.

a) Comparing Tracking Algorithms

Tracking of cells was the most difficult part of putting this research together and the Beatty et al. (2009) method, while appealing, needed some variations to help with the automation of this method, thus allowing for analysis of a larger sample of supercells. In their algorithm, multiple radar elevation angles were used to help located the updraft as well as its tilt for extrapolation to the surface; in the algorithm developed herein, level III radar data were used to locate mesocyclone locations near the surface. These locations, along with the storm-based reflectivity centroid, was the basis for the present tracking algorithm (see Data and Methods for more information). Note that the Beatty et al. (2009) algorithm only leveraged the base scan of radar reflectivity, and boundaries for storms

were identified using the bounds of the reflectivity echo when the cell was isolated and was objectively scrutinized when the cell wasn't isolated.

Figure 28 represents a supercell identified via the algorithm developed in this study as being within the CL precipitation regime. Not only is the radar appearance subjectively consistent with the CL precipitation type, but after accounting for the motion of the storm, there is clearly a forward orientation to the reflectivity core location with respect to the position of the mesocyclone. In addition, there is clearly a rather significant tornado present at the time of the snapshot, which helped the algorithm establish the mesocyclone location. Figure 29, in contrast, illustrates a supercell within the HP regime. Given the phase space diagram in the figure, it is clear that the reflectivity core location is much more neutrally oriented with respect to the updraft location. In other HP storms examined in this study, which are not shown, the reflectivity core location was oriented behind the mesocyclone location, consistent with Beatty et al. (2009; cf. Fig. 19). The final precipitation mode, LP, is represented in Figure 30. Here, while the storm tracked isn't a classic LP due to higher values of reflectivity in the storm core, it is evident that the reflectivity core is completely displaced from the area of circulation. The resulting phase space diagram hints at something in between the CL and HP regimes identified in Figs. 28 and 29, respectively. Given the lack of distinction of LP from the CL precipitation mode, as well as prior results from Beatty et al. (2009), we chose to combine the precipitation modes of LP and CL.

In all, the algorithms produced very similar results to Beatty et al. (2009); namely, only two precipitation modes (LP/CL and HP) were identified. Regarding the phase space

diagrams where the reflectivity core was related to the storm center (mesocyclone location), again the results were relatively similar (Fig. 31). In both Fig. 31a and 31b, the storms' motion is oriented in the direction of the positive x-axis. It is important to note that in both diagrams, HP storms remain primarily in the rearward orientation for the reflectivity core location, a good gut check. Also note that the plotted points in Fig. 31a represent a storm's predominant mode over its lifetime.

Even with the differences in the tracking algorithms (e.g., the location of the mesocyclone, the location of the reflectivity centroid), there is still great consistency among the results produced from each of the tracking methods. Again, both algorithms were only able to identify regions where LP/CL and HP storms exist, and radar-based tracking of cells cannot determine the difference between LP and CL storm regimes as true LP storms have their mesocyclone well displaced from any precipitation. This makes it hard to identify areas of rotation on radar for the true LP storms.

The distribution of supercell precipitation modes in this study is more heavily weighted toward LP/CL storms, with 66 storms being identified as such and only 38 being identified in the HP regime (Fig. 32). Regarding this distribution of supercells related to previous studies, there are some differences. In the Bluestein and Parks (1983) paper, they used 13 LP supercells in their analysis, as well as 9 supercells that fell outside of the LP regime, what is being identified as CL and HP here. In Rasmussen and Straka's (1998) paper, they analyzed a more uniform distribution of supercells with having identified 17 CL, 13 HP and 12 LP storms for a total of 42 identified supercells. Regarding the Beatty et al. (2009) paper, they identified a more skewed number of supercells, leaning more

towards that of the LP/CL regime as apparent in Fig. 31b. This, as expected from the similarity between the tracking algorithms, the distribution of supercells in our study is most like Beatty et al. (2009), though grouping the LP and CL cases from Rasmussen and Straka (1998) would result in a relatively similar distribution. In addition, thanks to the automation of the tracking algorithm, the total number of supercells identified here is more than double what these previous studies have identified at 104 tracked supercells.

b) Climatology

Broad geographical trends, temporal occurrence, as well as synoptic-scale patterns and storm motion, were explored for each precipitation regime to help identify from a forecasting standpoint any key differences.

Beginning with the attributes of the specific supercell regimes, there were both similarities and differences that accrued across multiple factors. The geographical location of the tracked supercells indicates few notable differences among HP and LP/CL storms; as evident in Fig. 33, the storm tracks nearly overlap with each other, with only a few small pockets where one mode dominates over the other (e.g., central Texas, eastern New Mexico, South Dakota, Iowa). This eliminates the idea that location is a key factor in determining precipitation mode and suggests other factors are more important.

Next, regarding the hourly occurrence of these storms, the cumulative frequency of the occurrence was calculated over of the course of the day (Fig. 34). From this graphic, it is apparent that the timing of these storms is nearly identical with only small differences presenting themselves in the early- to mid-morning hours as a slightly higher occurrence of HP storms and in the late-evening to overnight hours for LP/CL storms. The months in

which these storms occurred demonstrates a peak of supercell activity in the month of May. LP/CL storms occur more frequently in April and May (when deep-layer shear tends to be larger), while HP storms are more frequent in June (when deep-layer shear tends to be weaker; Fig. 35). Correspondingly, the magnitude of the forward motion of the identified supercells show that LP/CL storms tend to move at a higher rate of speed when compared to HP storms (Fig. 36).

Consistent with differences noted above in storm motion and monthly occurrence, there are notable variations in the synoptic environment (including jet-level [300 hPa], 500 hPa, and sea-level) of the storm precipitation categories. Composite anomaly maps are shown here due to the significant seasonal shift in synoptic patterns between the months of March and June.

Broadly, the maps illustrate similar features, vastly different magnitudes as well as more subtle differences in location. The LP/CL storms are identified with a much stronger trough/ridge system over the mountain west and Ohio Valley regions, respectively, at both 300 and 500 hPa (Figs. 37 – 38), with correspondingly stronger upper-level winds present in LP/CL cases. Near the surface, a strong low in the lee of the Rocky Mountains is event, with well-defined kinks in pressure trailing southward, associated with a cold front (Fig. 39).

On the contrary, HP storms found themselves in much weaker, less distinguished patterns both in the upper levels (i.e., 300 hPa and 500 hPa) as well as at the surface. While a similar general pattern was evident, the strength of these patterns was much weaker. At 300 hPa, the trough and ridge were displaced slightly towards the west (Fig.

37), however the flow for HP storms was much more zonal and not as conducive to strong synoptic forcing hence the much weaker, less defined surface low-pressure which appears as merely an elongated trough along the lee of the Rockies (Fig. 39). Again the 500 hPa level for HP storms produced a very similar pattern to that of the 300 hPa level as was found with LP/CL storms (Fig. 38).

Looking explicitly at the composite synoptic environments that these LP/CL and HP supercells identify themselves with, there appear to be significant differences, specifically with the wind profiles, that will be associated with each archetype. In addition, given the magnitude and location of these trough/ridge systems, LP/CL will lend themselves to stronger storm-relative flow as well as forward propagation when compared to HP storms. The latter can already be confirmed with the violin plot which presents the forward motion of these storms (Fig. 36), where LP/CL storms are shown to move at a higher rate of speed than HP storms.

c) Inflow Environment Comparisons

To begin, broad similarities and differences are evident while examining the composite skew-T log-p diagrams. The composite skew-t doesn't support any significant thermodynamic differences across the supercell spectrums as both the temperature and moisture profiles are nearly identical exhibiting at most a 2˚C difference among the archetypes (Fig. 40). The kinematic profiles on the other hand present higher importance when dealing with these storms, especially in the lower levels (Fig. 40). The largest variation in the temperature profile occurs in the upper troposphere above about 400 hPa, which would help to limit the amount of CAPE in the associated profiles, thus leading

to a conclusion that HP storms should exhibit lower values of CAPE when compared to LP/CL storms (Fig. 40). In addition, this feature would lower the equilibrium level (EL) in the case of HP storms. Furthermore, the moisture profile exhibits a slightly drier profile in the mid-levels for HP storms (Fig. 40). This helps to increase entrainment of dry air into downdrafts, which enhances evaporative cooling, strengthens downdrafts and helps to explain the strong straight-line winds that are associated with these storms (e.g., Gilmore and Wicker 1998; James and Markowski 2010). While both Grant and van den Heever (2014) and Honda and Kawano (2015) experimented with mid-level dry air in their simulations, there was no note regarding downdraft intensities. They instead focused on the simulations compared to a moist mid-level profile and found decreased surface precipitation, leaning more toward LP/CL storms. The result found here does not agree with these two studies, however it is worth noting that many other variables play a role into the association of precipitation structure. Thus, the role of mid-level dry air, while not entirely clear as concluded by the contrasting results from both Gilmore and Wicker (1998) and James and Markowski (2010) when compared to both the Grant and van den Heever (2014) and Honda and Kawano (2015) studies, the presence of dry air in the mid-levels for HP storms is more consistent with Gilmore and Wicker (1998) and James and Markowski (2010).

To further explore how these composite similarities and differences manifest more broadly for LP/CL and HP storms, the distribution of various thermodynamic and kinematic parameters will be examined next. In most instances, the presence of statistically significant differences was tested using the Kolmogorov-Smirnov test, which

is a non-parametric test that determines if two distributes differ from each other by finding the largest difference in their cumulative distribution functions. However, if a distribution was normally distributed, then the student's-t test was used. Both types of statistical tests were leveraged to attain more accurate significance values; note that this choice largely did not impact the significance of the results. It is further noted that the soundings used for calculating each parameter value is based off a composite for each hour depending on the number of 'acceptable' grid points within the previously determined inflow region (see Data and Methods chapter).

i) Thermodynamic comparisons

In this subsection, precipitable water (PWAT), multiple forms of CAPE, LCL heights, LFC heights and low-level relative humidity will be tested for significant differences regarding the two supercell groupings (LP/CL and HP). In addition, physical explanations will be provided to develop a reasoning for any difference that was found.

Given some of the more apparent differences in mid-level moisture, the first parameter discussed is PWAT, which is integrated over the entire atmosphere. As shown in Fig. 41, on average, HP storms exhibit slightly lower values of PWAT when compared to LP/CL storms. Even so, there is large variability within the HP regime; this larger variability leads to a statistically significant difference (via the KS tests) between the LP/CL and HP distributions. Yet, a closer examination of the median, and inter-quartile range illustrates nearly identical values between LP/CL and HP storms. This physically makes sense because of how similar the moisture profiles were to each other. However, this finding of broadly similar PWAT distributions is inconsistent with prior studies, including Bluestein

and Parks (1983) and Rasmussen and Straka (1998), who both found that LP storms have lower PWAT values than HP storms. Even so, the present study combines CL and LP storms together, so the potential signal of smaller PWAT for LP storms may be obscured.

All varieties of CAPE, whether it be surface-based (SB), mixed-layer (ML) or most-unstable (MU), are significantly higher for LP/CL storms (Fig. 42). For example, SBCAPE of LP/CL storms exhibited a median value of 1450 J/kg, while HP storms saw a much lower median SBCAPE of 723 J/kg. This result is at odds with Bluestein and Parks (1983) which found no difference between archetypes yet is more consistent with Rasmussen and Straka (1998), since HP storms were found to have less CAPE than the CL counterpart. One can explain these differences in CAPE as merely the slight temporal differences that have been seen among the archetypes as there is generally less instability in the early morning hours when HP storms tend to occur a bit more frequently and more instability in the evening hours when LP/CL storms are more frequent.

Given that CL storms are much more likely to produce tornadoes (and violent ones) than HP storms (Doswell and Burgess 1993; Moller et al. 1994), this would suggest that LP/CL storms should exhibit lower LCL heights, which have been tied to tornado production (e.g., Rasmussen and Blanchard 1998; Thompson et al. 2003). Figure 43 provides further evidence of this connection, as LP/CL storms were found to have significantly lower LCL heights compared to HP storms, consistent with Rasmussen and Straka (1998). However, this result is somewhat at odds with Bluestein and Parks (1983), who found LP supercells to have significantly higher LCL heights. Yet, their results may be skewed compared to the present study; most of their LP storms occurred near drylines

where dewpoints are generally suppressed, thus leading to an increased height of the LCL. Given the composite profiles (Fig. 40), it may also follow that LP/CL storms would have lower LFC heights as well (Fig. 44). While the median LFC height for LP/CL storms is indeed lower than HP storms, the difference is not significant, which is in line with Bluestein and Parker (1983) yet differs from Rasmussen and Straka (1998).

To appeal more towards prior modeling studies of supercell precipitation types, a 1-3 km average relative humidity was calculated for each storm; this layer has been found to be impactful in producing LP storms (e.g., McCaul and Cohen 2002 ; Grant and Van Den Heever 2014). However, Fig. 45 demonstrates very similar distributions between both supercell archetypes. While it physically makes sense that if you lower the RH near the surface, then you are more prone to entrainment thus lowering the strength of the updraft and consequently the amount of air being advected upward, this is not consistent with the observations in this study. The modeling studies control for the CAPE and the wind profile, both of which were found herein to differ between the archetypes (see kinematic subsection for details regarding wind profile) and thus will affect the precipitation structure of a supercell.

The effective layer (i.e., Thompson et al. 2007), while generally associated with kinematic variables such as storm-relative helicity (SRH), can generally identify the inflow layer for a given environment (i.e., identify the layer with sufficient CAPE and minimal CIN). In this case, the effective layer has been married to the precipitable water to give an idea of how much moisture is actually being ingested by these storms. Notably, the depth of the effective layer is similar between LP/CL and HP storms (Fig. 46a). However,

as shown in Fig. 46b, the integration of PWAT over the depth of the effective layer illustrates that effective PWAT is higher in LP/CL storms than in HP storms. This finding can be tied to higher low-level moisture for LP/CL in the effective layer given that the depth of the effective layer is nearly identical for both groups.

ii) Kinematic Comparisons

The kinematic profiles have already been shown to be impactful in determining the precipitation structure of supercells (e.g., Rasmussen and Straka 1998); the present study also finds significant differences among storm types (i.e., Fig. 40; see also Fig. 47). For example, storm-relative flow near the surface, in the mid-levels, and near the outflow of the storm have shown their importance in identifying precipitation structure (e.g., Rasmussen and Straka 1998; Warren et al. 2017). In the comparisons described herein, the shear vectors were calculated from storm-relative winds which were then rotated to the 0-4 km bulk shear vector to facilitate more accurate comparisons among the wind profiles (i.e., as in Rasmussen and Straka 1998). Comparisons in this section include but are not limited to bulk shear vectors from and to multiple levels in the atmosphere as well as their individual components, storm-relative flow profiles throughout the depth of the atmosphere and composite hodographs.

Beginning with a highly contested result between the Warren et al. (2017) and Rasmussen and Straka (1998) study, the shape of the hodograph, there is a very distinct difference between the supercell archetypes (Fig. 47), consistent with the notable differences in the strength of corresponding synoptic scale systems (Figs. 37 – 39). In the lowest few kilometers of the atmosphere, there is a clear difference in the shear

magnitude, with LP/CL storms exhibiting much higher bulk shear as well as directional shear. Accordingly, storm-relative helicity is significantly higher for LP/CL storms over a variety of layers (Fig. 48). In addition, the composite hodograph also shows higher bulk shear magnitudes in the mid-levels (4-7 km AGL). Furthermore, LP/CL storms exhibit veering upper-level winds above 7 km, in strong contrast to Rasmussen and Straka (1998), which found backing winds aloft with LP/CL storms (Fig. 13). However, this result is consistent with the Warren et al. (2017) simulations; upper-level veering was shown to elongate both the updraft and precipitation shield towards the northwest, while backing upper-level winds were associated with a more circular updraft and precipitation falling more so in the rear-flank of the storm (i.e., HP archetype).

In addition to finding backing of upper-level winds in LP/CL storms, the Rasmussen and Straka (1998) study also found significantly higher shear vector magnitudes for LP/CL storms within the BL to 9 km and 4-10 km layers (Fig. 12). In the present study, the BL-9 km shear vector magnitude is significantly higher for LP/CL (Fig. 49a), but not for 4-10 km (Fig. 49b). Over the larger depth, this makes sense given the much longer hodograph for LP/CL storms relative to HP storms. However, for the 4 – 10 km layer, the distinction becomes much less clear as the composite hodographs (Fig. 47) show that most of the shear, especially for LP/CL storms occurs in the low-levels, below 4 km AGL and that the 4 – 10 km layer exhibits very similar shear, consistent with Fig. 49b. While the upper level wind speed for LP/CL storms is clearly higher, the increased storm motion for this archetype helps to eliminate any significant difference in shear magnitudes throughout the 4 – 10 km layer.

While the identifying the magnitude of the shear vectors is of common practice, they don't tell the full story of how the winds are changing with height. Thus, identifying the u and v components of the shear vector will help to get a better idea of how the winds are changing over the depth of a layer. Taking the 4 – 10 km shear vector, which was not found to be significant via the magnitude and breaking it into its components will help to show why it may have not been significant. Figure 50a, which denotes the u-component of this shear vector helps to explain that LP/CL storms exhibit stronger zonal shear. In addition, the v-component (Fig. 50b) helps to explain that LP/CL storms demonstrate larger meridional shear though this layer. This helps to justify the veering profile which has previously be associated with LP/CL storms both herein as well as in Warren et al. (2017).

Brooks et al. (1993) also suggested that the magnitude of the winds at 7 km AGL, as well as the 3 – 7 km AGL shear normalized by height could be influential for supercell precipitation type by altering the low-level vorticity structure. The alteration of the low-level vorticity structure is described by a change in the storms forward motion due to changes in the mid-level wind structure; however the authors did not provide a physical explanation as to how the precipitation structure may be altered as a result. However, Rasmussen and Straka (1998) suggest that stronger outflow aloft helps to advect hydrometeors further from the updraft, so this may be a contributing factor when examining winds closer to the mid-levels near 7 km. In this study, the 7 km AGL winds are significantly stronger for LP/CL storms (Fig. 51a), consistent with the hypothesis from Rasmussen and Straka (1998). Further examination of the normalized 3 – 7 km AGL shear

vector also illustrates a statistically significant difference (stronger shear for LP/CL storms), though there is a notable amount of overlap of the distributions as well (Fig. 51b). Thus, while the mid- and upper-level winds near 7 km are significantly different, the Brooks et al. (1993) hypothesis suggesting that the mid-level shear magnitude impacts the precipitation structure of supercells does not hold up to additional observations. This may be explained by the fact that LP/CL storms propagate faster than HP storms, thus negating any affect that the stronger environmental winds would have in the mid-levels in a storm-relative sense.

Shear vectors originating from the surface, such as the 0 – 1, 0 – 3 or 0 – 4 km layers (Fig. 52), exhibit significant differences among the two groups. In the low levels, the increased storm motion should allow for stronger storm-relative flow; indeed, the results in the 0 – 1 km and 0 – 3 km layers match the results found in 0-1 and 0-3 km SRH. The 0 – 4 km shear vector would also suggest an increase from as you go from HP to LP/CL and again this is the case. This information can be deduced from the composite hodograph (Fig. 47). The increased shear in the low levels for the LP/CL group is explained nicely by the stronger surface low that is generally associated with these storms.

Focusing on storm-relative wind profiles (Fig. 53), there are some distinct differences between the LP/CL and HP groups. Broadly speaking, the magnitude of storm-relative flow tends to be larger for LP/CL storms. The storm-relative flow magnitude for both LP/CL and HP storms appears to peak around 1 km AGL; this maximum is largely due to the v-component, particularly for LP/CL storms (average peak around 20 m/s). This strong v-component suggests that LP/CL storms are likely associated with a stronger low-

level jet than HP storms, which is broadly consistent with the synoptic differences pointed out earlier (Figs. 37 – 39). Figure 53 also demonstrates that the storm-relative flow minimum occurs at a lower height in LP/CL storms (3 km) than HP storms (3.75 km). This minimum is more a function of the u-component of the wind, since both storm types have nearly identical v-wind profiles above 2 km AGL. In the upper-levels, stronger storm-relative flow is evident, and consistent with findings from Rasmussen and Straka (1998), suggesting that their hypothesis of stronger upper-level outflow leads precipitation away from the updraft. However, this differs from the findings of Warren et al. (2017), who demonstrated that stronger storm-relative flow in the upper-levels led to stronger inflow, a wider updraft, and more precipitation. Notably, however, the Warren et al. (2017) study used a fixed thermodynamic profile, while the present study includes a variety of thermodynamic environments, which likely accounts for the differing results.

d) Sensitivity Testing

To determine how sensitive the above results were to the thresholds chosen in the tracking algorithm to demarcate LP/CL from HP storms, additional testing was conducted. While our results are consistent with Beatty et al. (2009) in terms of identifying LP/CL and HP storms (Fig. 31), further work is needed. Here, the sensitivity of the tracking algorithm was tested by altering the threshold between where LP/CL and HP storms by 1-2 km (see more details in Data and Methods). These shifts in the threshold ultimately changed the number of storms that fell into each group and the negative shifts worked to lower the number of HP storms (specifically the minus 2 km shift), to a point where statistical testing would not be accurate as the sample size dropped below the

common threshold of 30 (Fig. 54). In addition, shifts in the threshold also veered the distribution of the LP/CL to HP storms away from the ratio that can be loosely seen in Beatty et al. (2009). After re-identification using these new thresholds, new comparisons of LP/CL and HP inflow environments resulted in a few differences in terms of significant parameters. These include SBCAPE, MUCAPE, 0 – 3 km SRH, and the magnitude of the 7 km AGL wind.

Looking at the phase space diagrams for each of the shifts in the thresholds (Fig. 54), there it is clear that shifting the threshold too far to the right will begin identifying true HP storms into the LP/CL category. For example, the supercell depicted in Fig. 29 would be identified as LP/CL in both the minus 1 km and minus 2 km shifts in the threshold. Additionally, a shift in the negative direction indicates precipitation more so in the rear-flank of the storm, a distinguishing feature of HP storms.

Overall, it can be said that a leftward shift in the boundary between LP/CL and HP storms is associated with higher variability of the results than a rightward shift. In all the variables tested, a shift of minus 1 and a shift of plus 2 was not associated with any significant variations in the significance testing or the shape of the associated violin plots. This concludes that a ± 1 km shift to the boundary will not significantly alter the results described herein thus explaining that the tracking algorithm is not very sensitive to large shifts in the diagnosed boundary.

e) Summary

The development of a supercell tracking algorithm in the same manner as Beatty et al. (2009) has produced largely consistent results (Fig. 31). Thus, only two categories of supercells were identified, those falling in either the LP/CL category or the HP category.

While there were no significant differences in terms of geographic or temporal distributions of LP/CL versus HP supercells (Figs. 33 – 34), pronounced differences were evident in the synoptic patterns; LP/CL storms were associated with strong large-scale forcing and notable meridional flow, while HP storms tend to be associated with weaker flow patterns and more zonal flow. These synoptic-scale characteristics underly many of the variations among parameters that were later deemed significant.

Key thermodynamic parameters include all forms of CAPE (MU, ML and SB) as well as total PWAT and effective layer PWAT and LCL height. All these factors are to some degree realized by the synoptic environment supporting them. In addition, the CAPE found itself a function of time of day were LP/CL storms tended to exist more frequently in the evening hours where HP storms occurred more often overnight and into the early morning hours when instability is generally lower, especially SBCAPE.

Regarding kinematic parameters, the shape and intensity of the wind profile both in the upper levels and as well as near the surface proved to be important in determination of supercell precipitation structure; many of these differences were explained by the synoptic pattern that each group predominately found themselves in. Stronger synoptically forced environments such as those found with LP/CL storms tend to

support higher values of shear than the weaker, more zonal flow that was associated with HP storms.

Finally, it is important to note that the above findings were largely insensitive to the choice of threshold separating LP/CL versus HP storms in the automated tracking algorithm. Changes up to about 1 km in either direction exhibited no change to the significance of any testing. This result provides insight that the tracking algorithm is not very sensitive to changes/shifts to the boundary between LP/CL and HP storms.

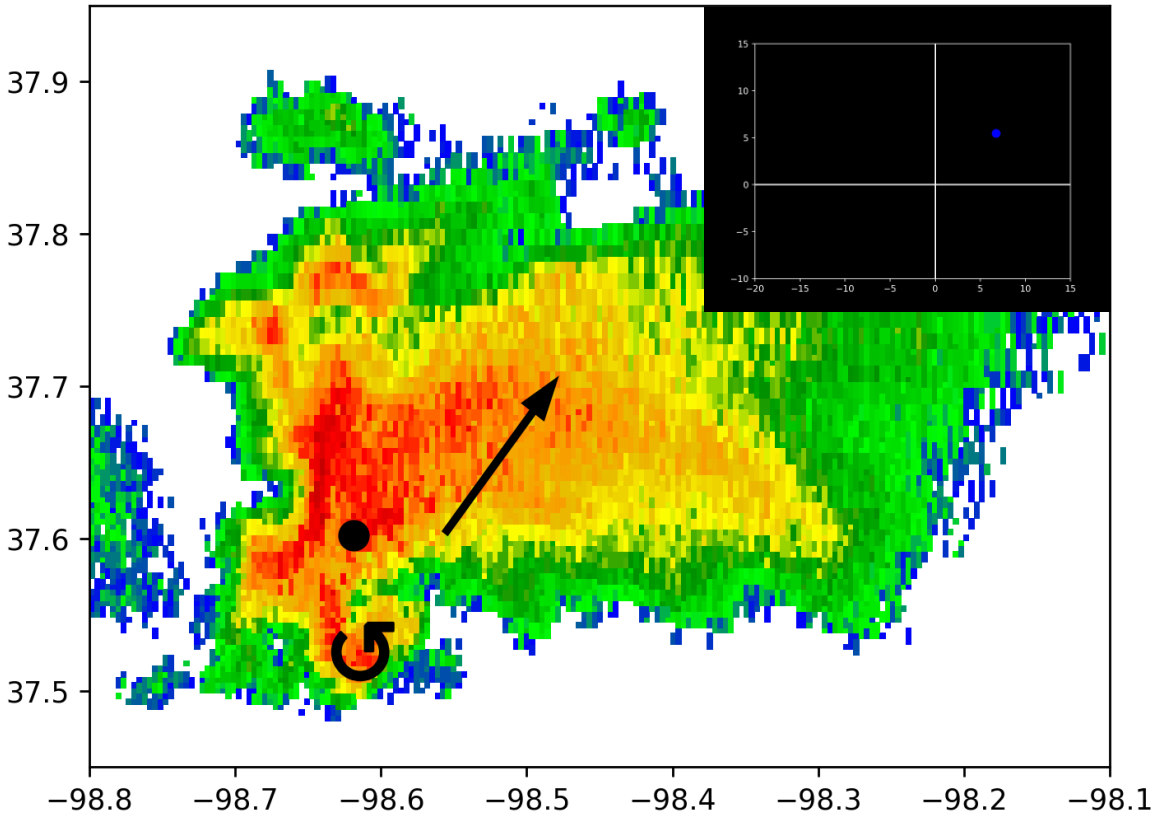

Figure 28 – A representation of what was identified as being within the CL precipitation regime as analyzed by the tracking algorithm developed herein. The filled circle and counterclockwise arrow on the map represent the reflectivity core and the mesocyclone locations, respectively. The black arrow is pointing in the direction of the storms motion. In the top right panel, the phase space diagram for this given timeframe is presented with (0,0) representing the storms mesocyclone location and the positive x-axis pointing in the direction of the storms motion. The blue dot on the inset graph represents the displacement of the reflectivity core location relative to the mesocyclone location.

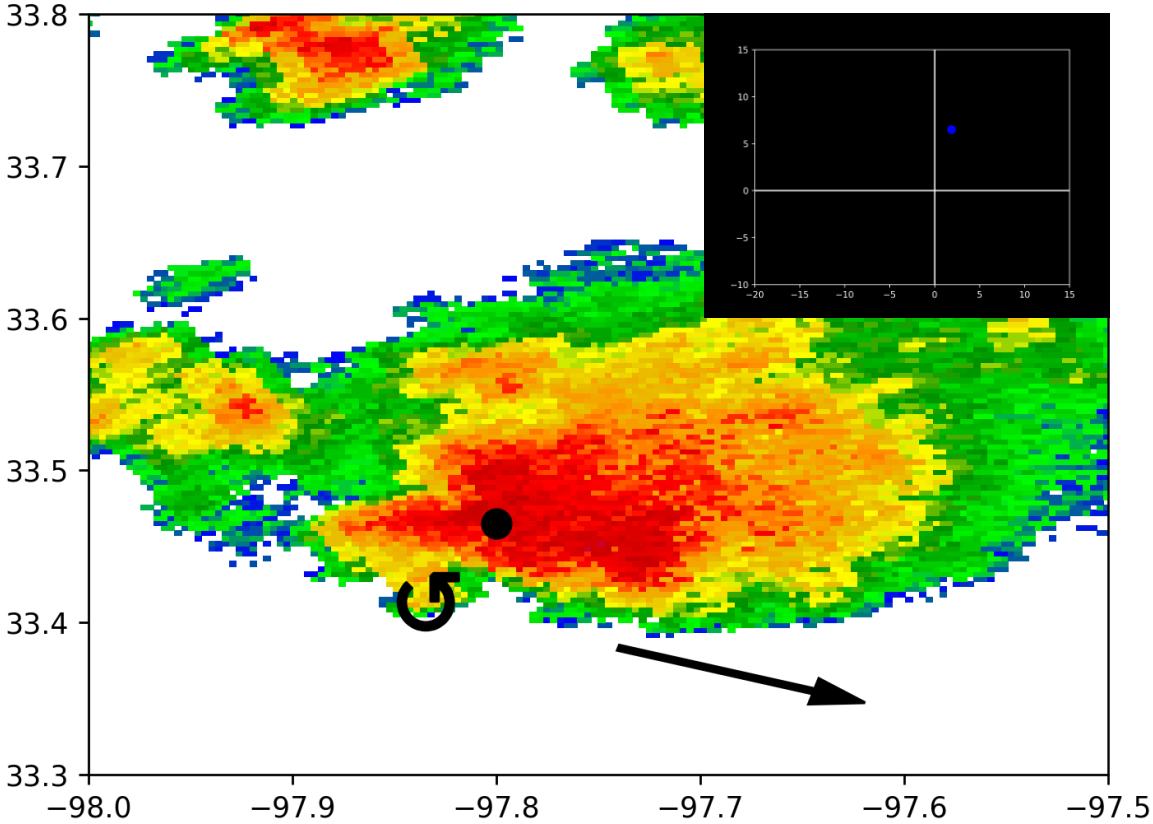

Figure 29 – Same as in figure 28 but representing an HP supercell.

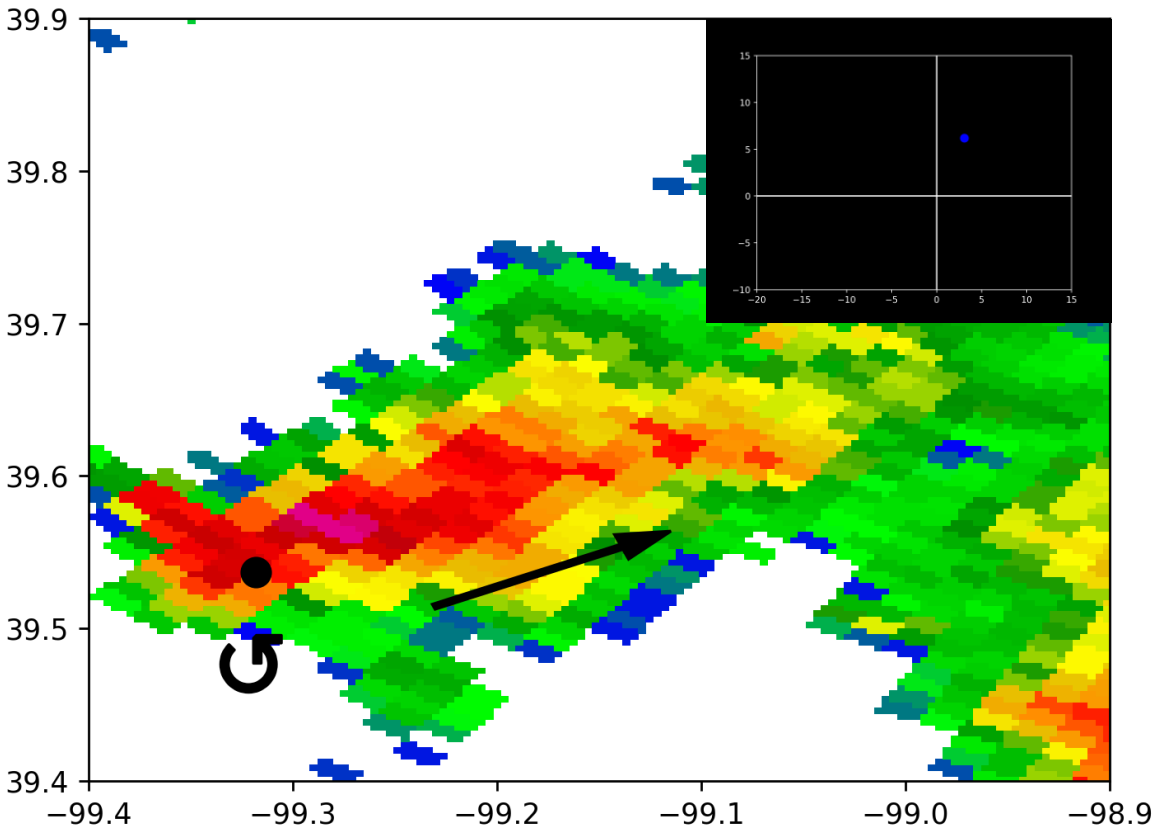

Figure 30 – Same as in figure 28 but representing an LP supercell.

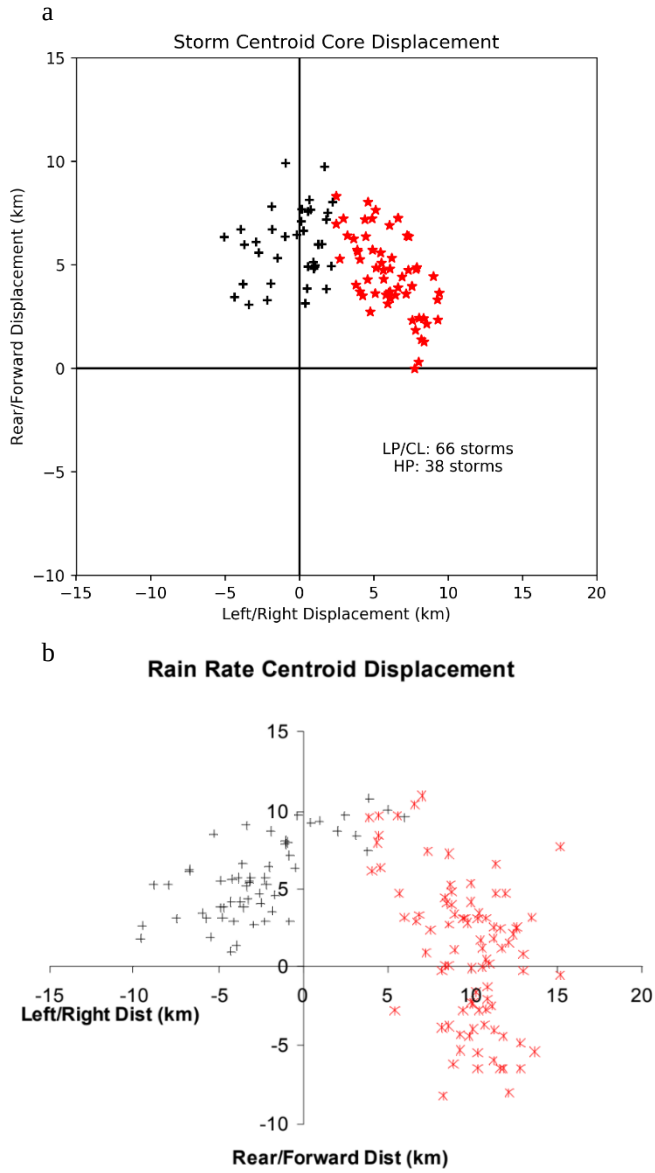

Figure 31 – The core displacement for each storm mode identified by the tracking algorithm in a) the one developed herein and b) the one developed by Beatty et al. (2009), where b) was adopted from. The red '*' in both diagrams represent the LP/CL storm whereas the black '+' in each diagram represents the HP storms.

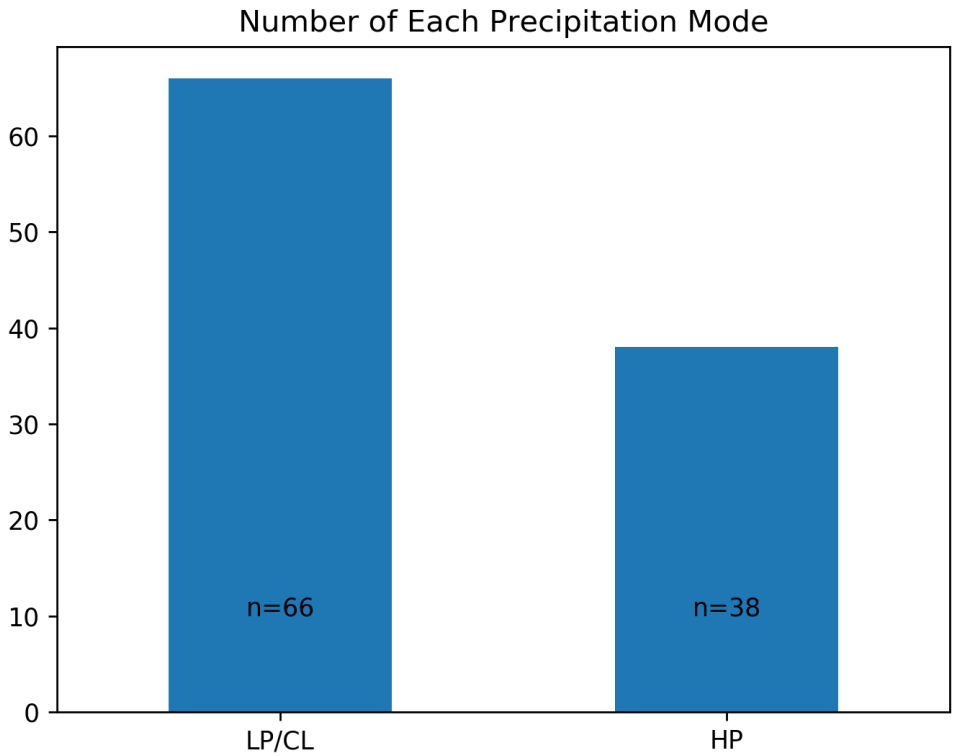

Figure 32 – The number of each supercell precipitation archetype with LP/CL storms amalgamated due to their lacking discrepancies within the tracking algorithm. The exact numbers for each are labeled with the bar.

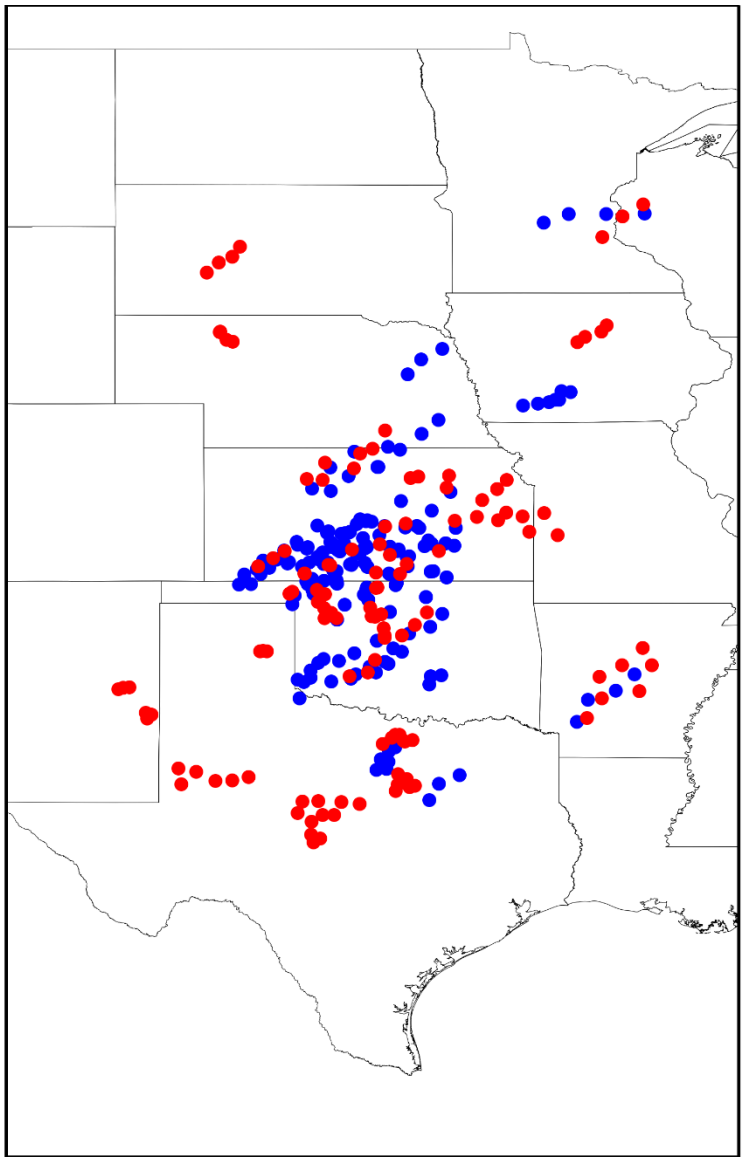

Figure 33 – The spatial distribution of supercells that fall into the LP/CL regime (blue) and the HP regime (red). Each hourly observation of the storm is plotted to reduce clutter.

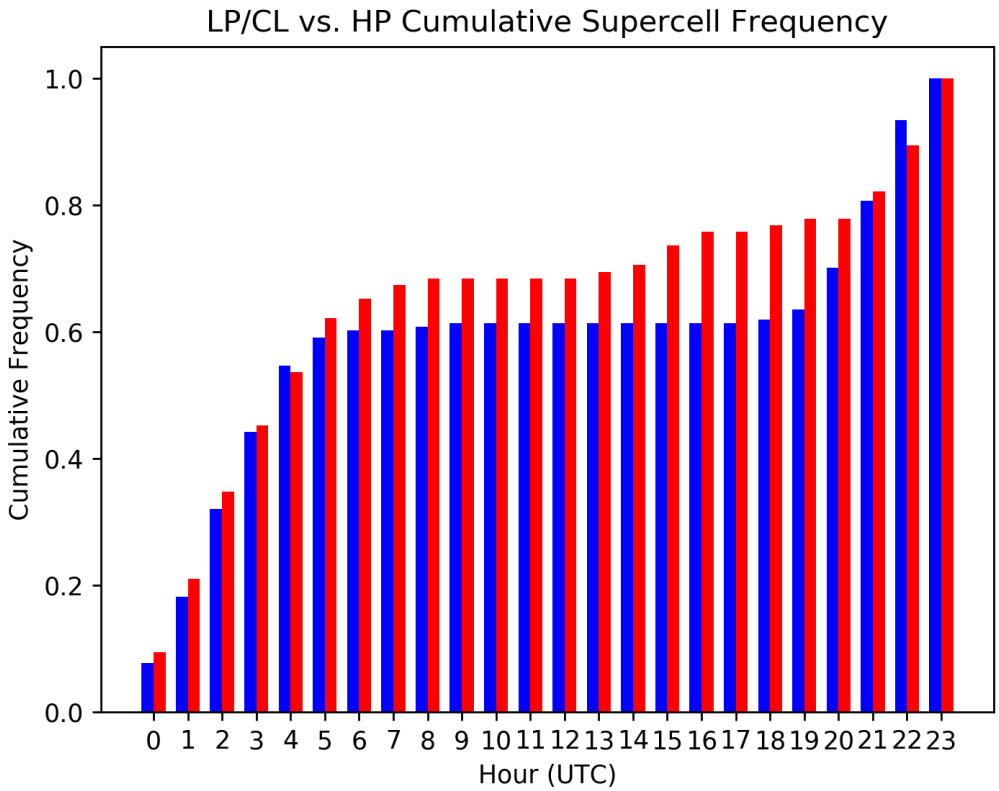

Figure 34 – Cumulative frequency graph representing the relative frequency occurrence of LP/CL and HP storms in blue and red, respectively. The hours listed are in UTC.

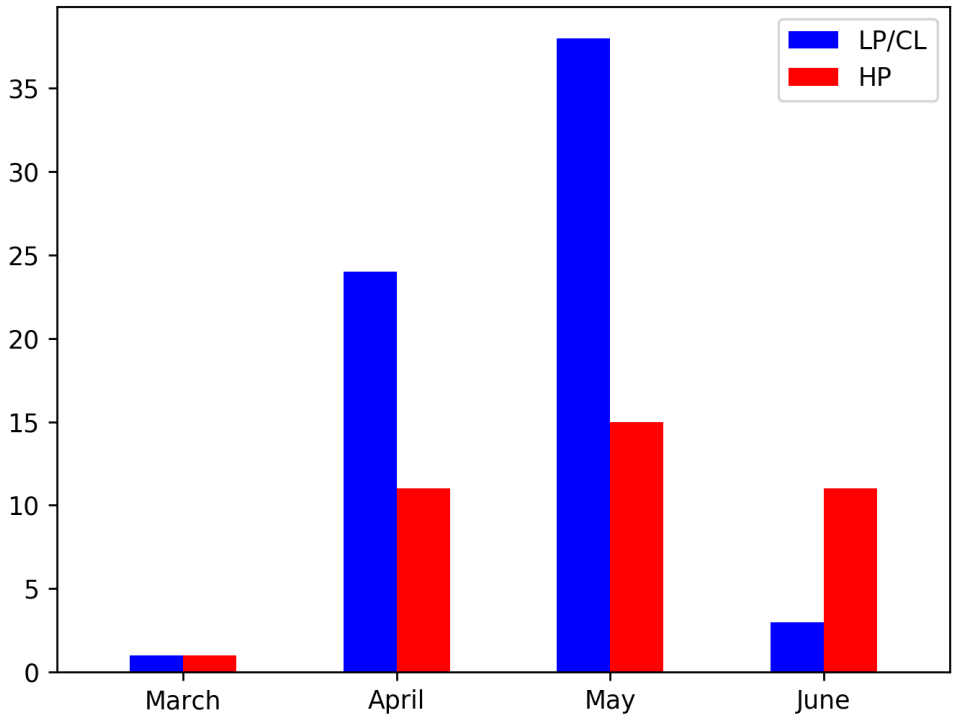

Figure 35 – The distribution of supercells within the period of interest for this study (March – May). The red bars represent the number of HP supercells tracked were the LP/CL storms are represented by the blue bar. Peak activity is in May with more HP supercells occurring in June than LP/CL supercells.

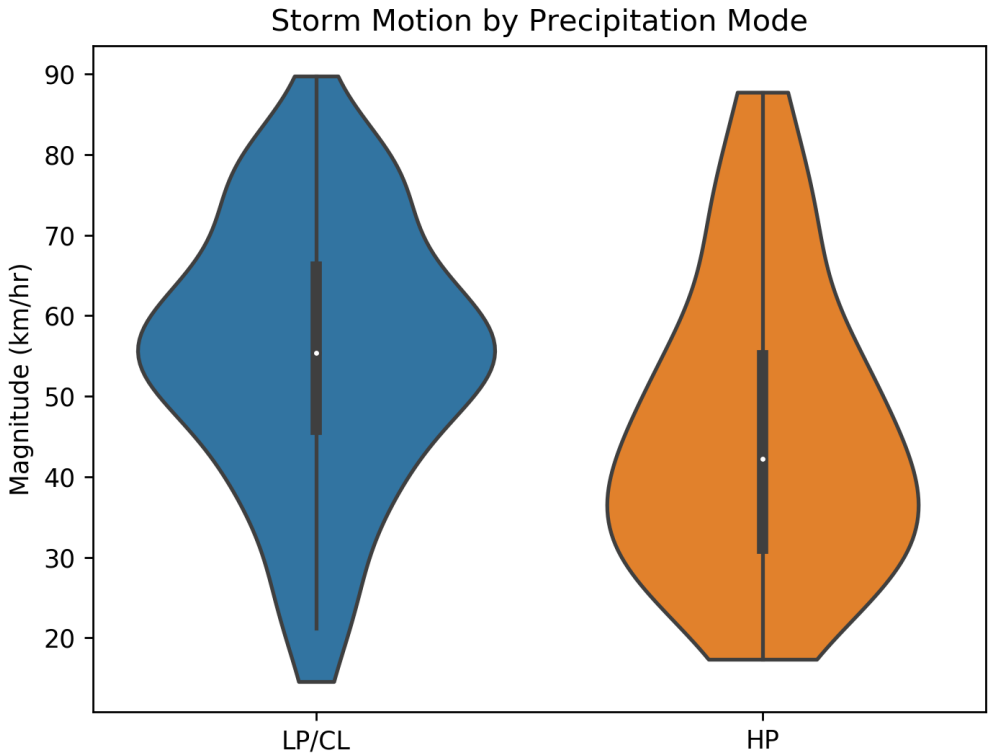

Figure 36 – Represented here is the average forward motion of each supercell regime as a violin plot. The distribution of the forward motion is shown by the blue and orange curves for LP/CL and HP storms, respectively. In addition, a boxplot is overlaid on the distribution with the endpoints representing the 10th and 90th percentile towards the bottom and top of the figure, respectively. The rectangle represents the inter-quartile range (IQR) and the white dot represents the median value for each distribution. The abrupt cut-off regarding the distributions represent the minimum and maximum values within the datasets.

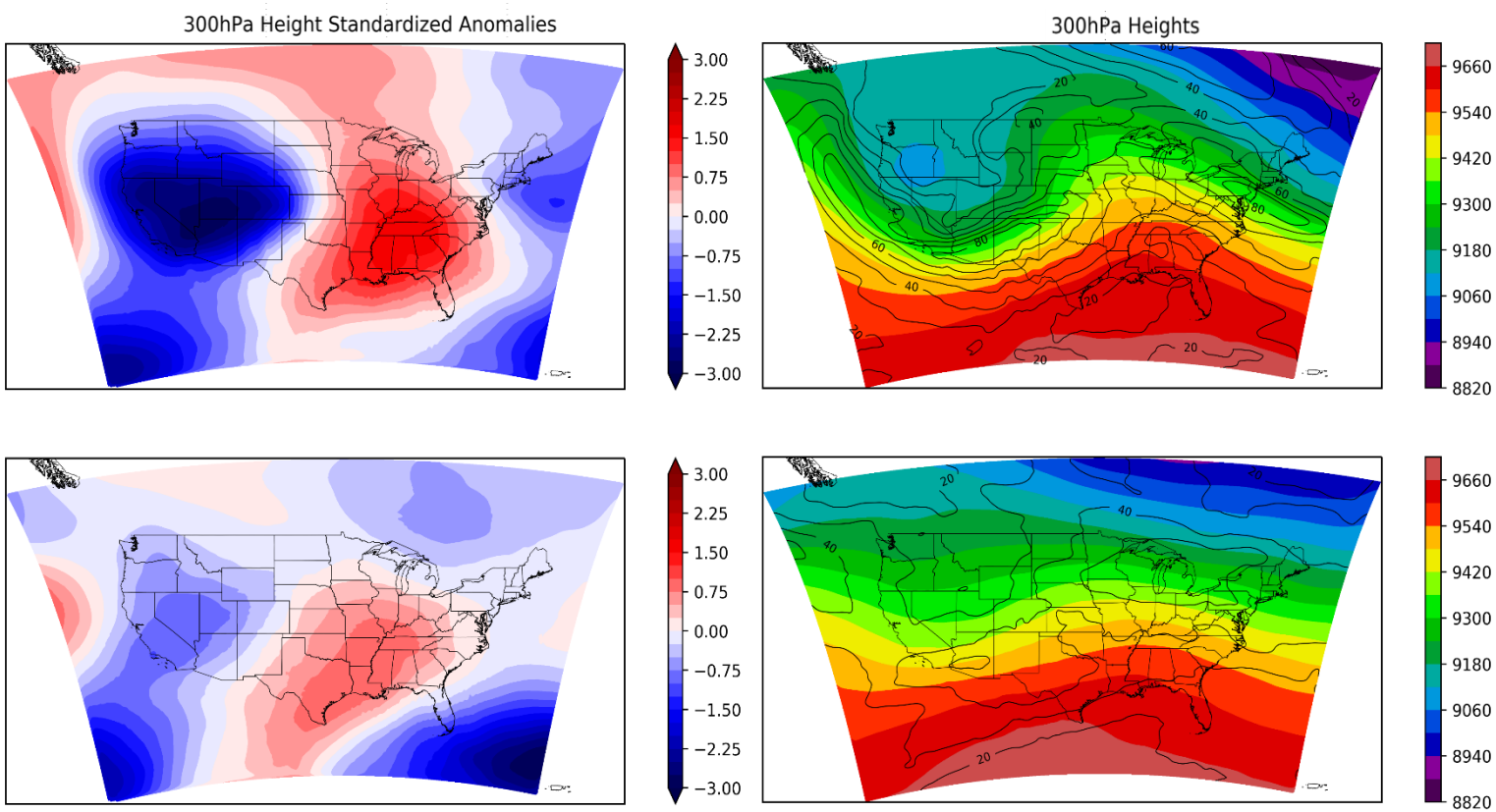

Figure 37 – Composite synoptic map at 300hPa over the contiguous United States. The top graphics represent LP/CL storms and the bottom graphics represent HP storms. On the left, standardized anomalies are presented whereas on the right, the geopotential height and wind speed are presented.

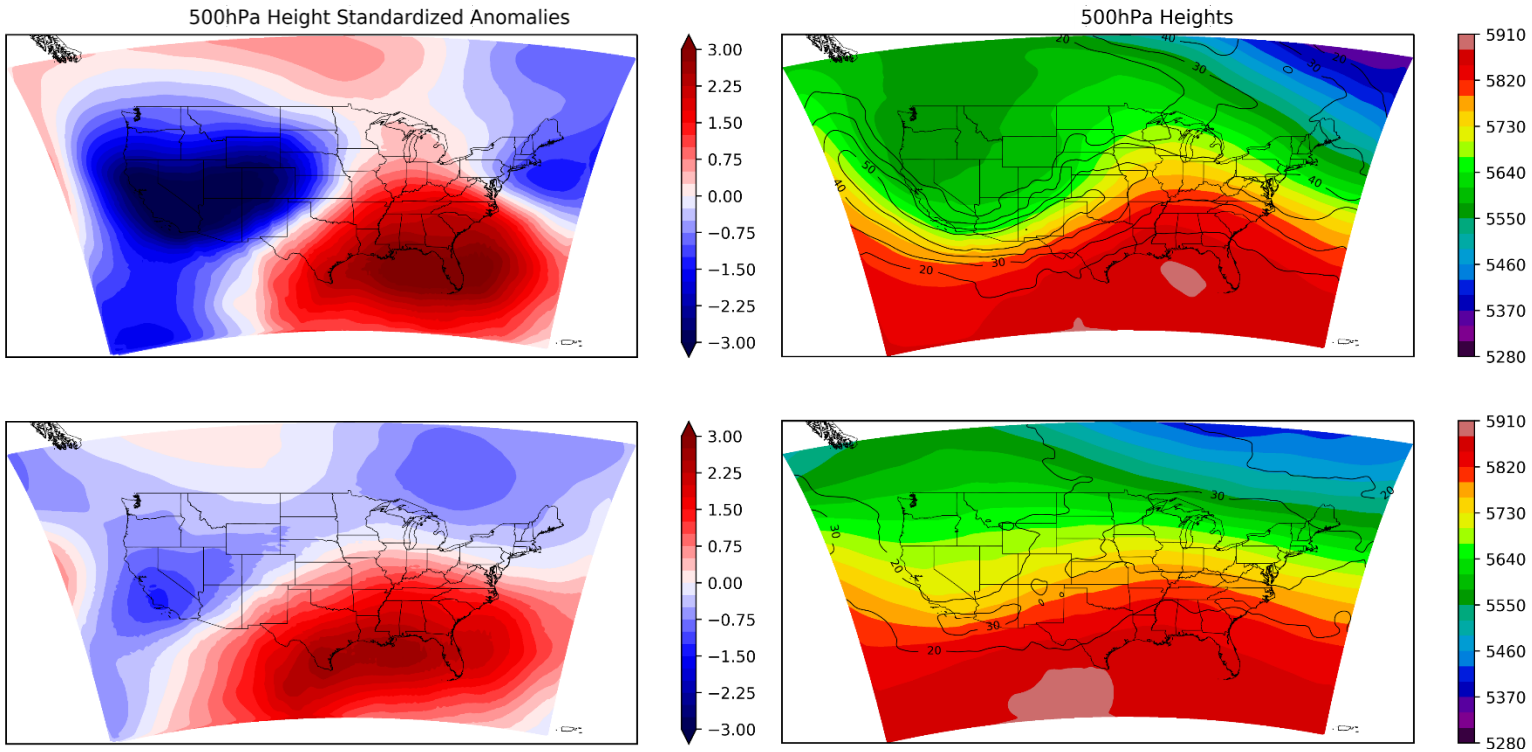

Figure 38 – Same as in figure 37, but for the 500hPa surface.

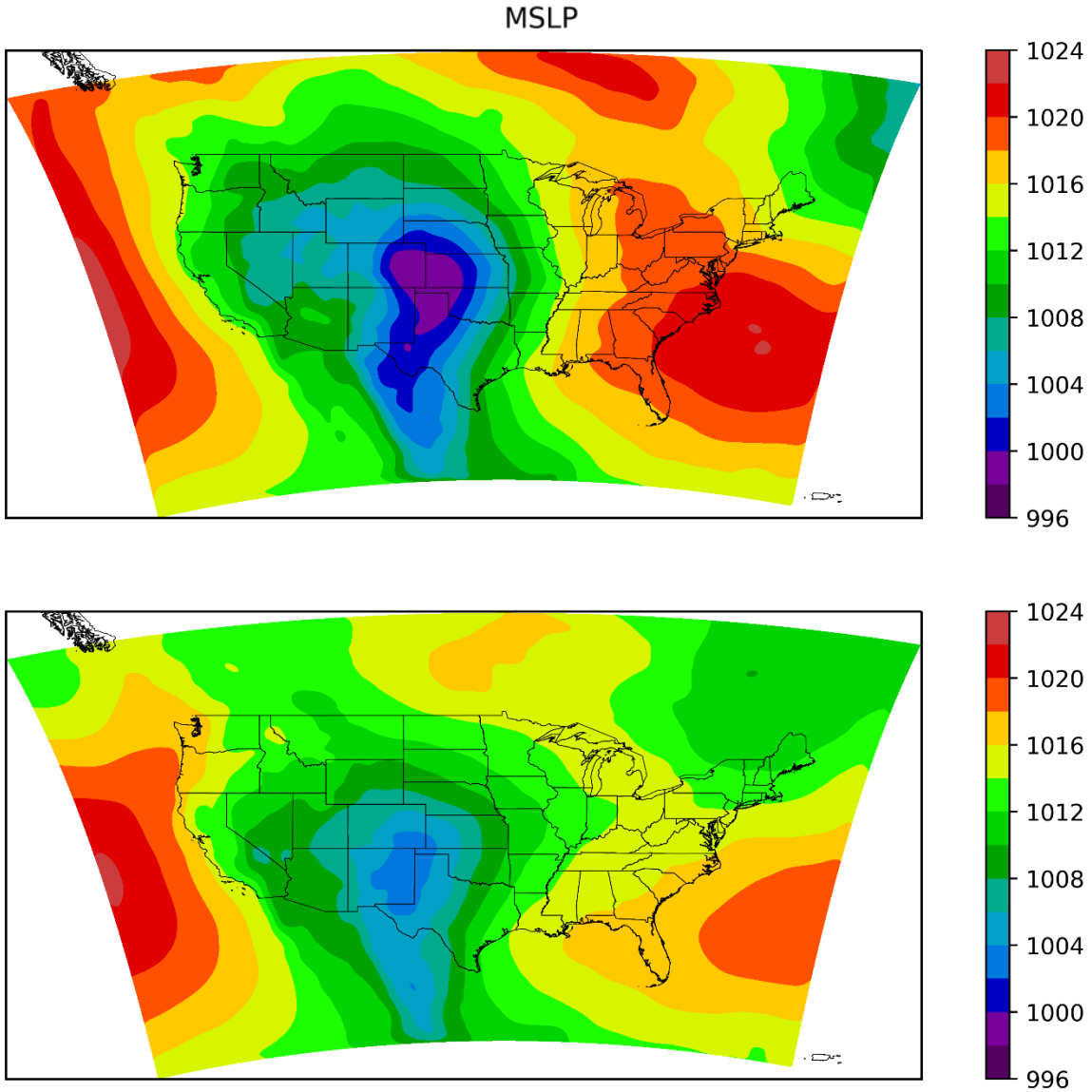

Figure 39 – As in the right half of figure 37, but regarding the mean sea-level pressure.

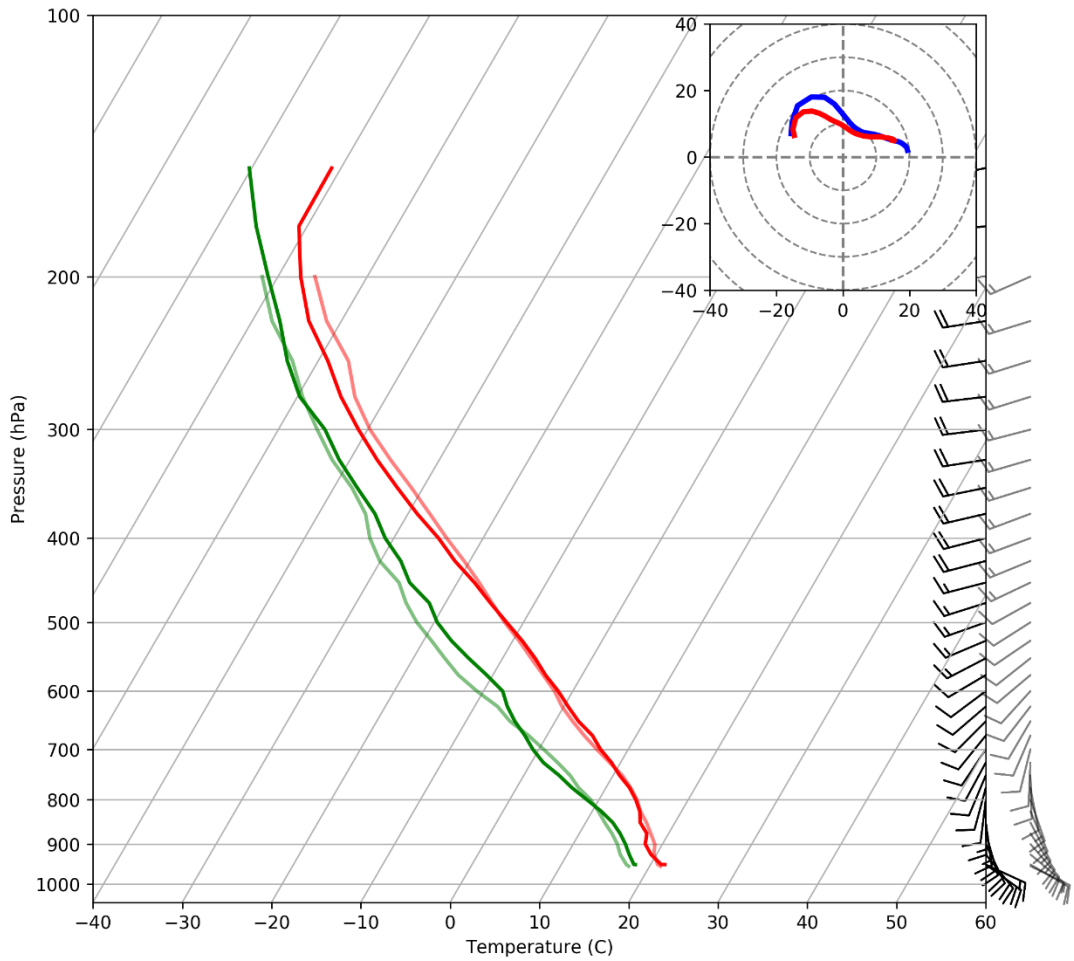

Figure 40 – Composite sounding for both supercell groups. The more opiate lines and wind barbs represent that of the LP/CL group and the more transparent ones represent the HP archetype. The red lines and green lines represent the temperature and dew point profiles, respectively. Inset in the top-right of the figure is the composite hodographs for each group with the blue and red lines representing the LP/CL and HP archetypes, respectively. All the winds on this graph are in m/s and are the storm-relative winds rotated to the 0-4 km bulk shear vector.

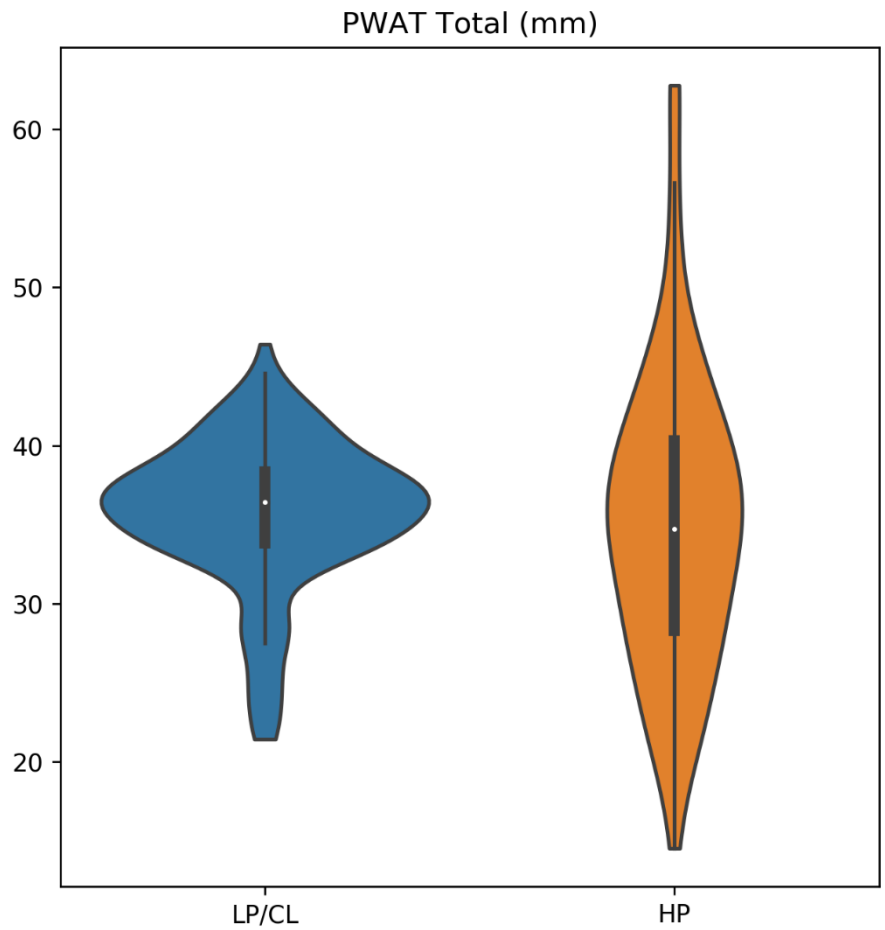

T-Statistic: 0.966, P-Value: 0.335
KS-Statistic: 0.252, P-Value: 7.82e-05
CL Normality T-Stat: 33.6, P-Value: 5.03e-08
HP Normality T-Stat: 0.2, P-Value: 0.905
LP/CL --> Median: 36.4, 25th: 33.9, 75th: 38.4, IQR: 4.51
HP --> Median: 34.7, 25th: 28.3, 75th: 40.3, IQR: 12.0

Figure 41 – Total precipitable water within the sounding for LP/CL storms and HP storms. Beneath the graph are the respective student t-statistic and p-value, KS-statistic and p-value, LP/CL normality test, HP normality test and spread of the data for each of the violin plots, specifically, the 25th, 50th and 75th percentiles as well as the range of the 25th-75th percentiles (IQR). The bolded text represents the test that is most appropriate given the distribution of the data. The general nature of the violin plot is the same as that in figure 6, please refer to it for further details.

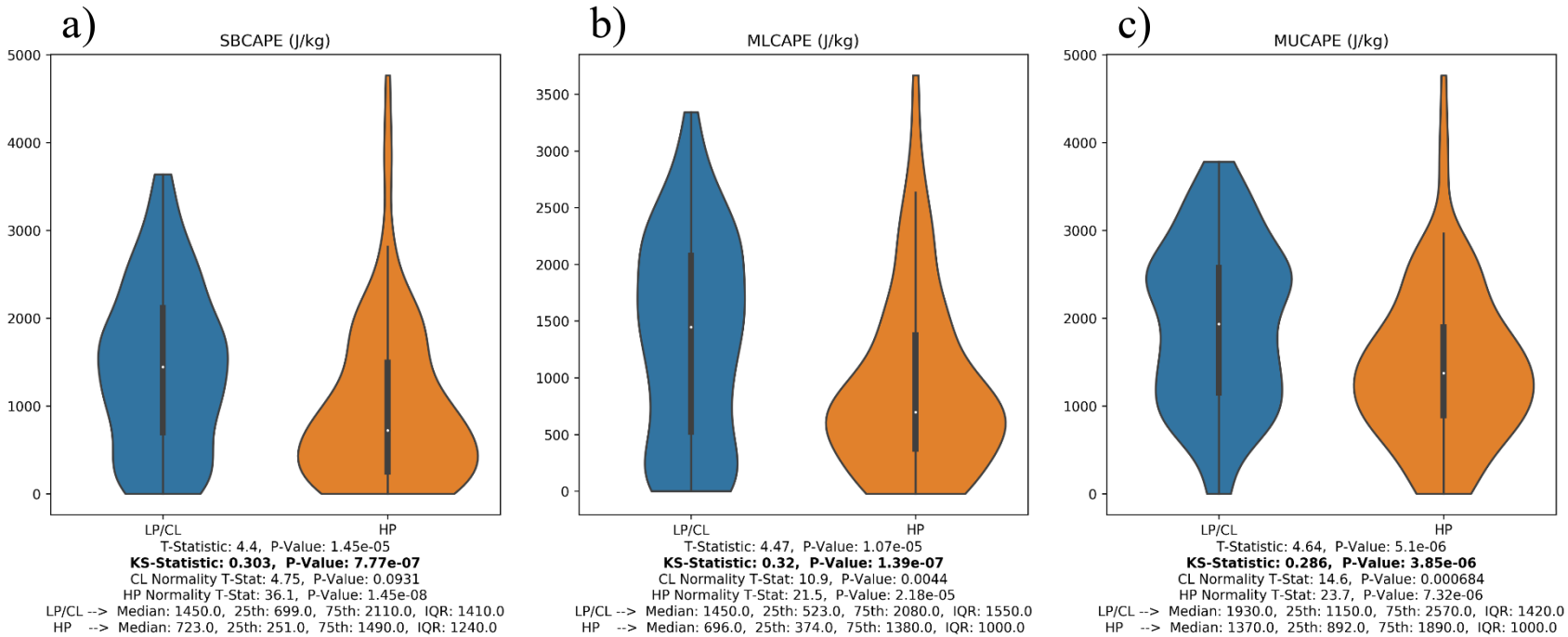

Figure 42 – Same as in figure 41, but for SBCAPE (a), MLCAPE (b) and MUCAPE (c).

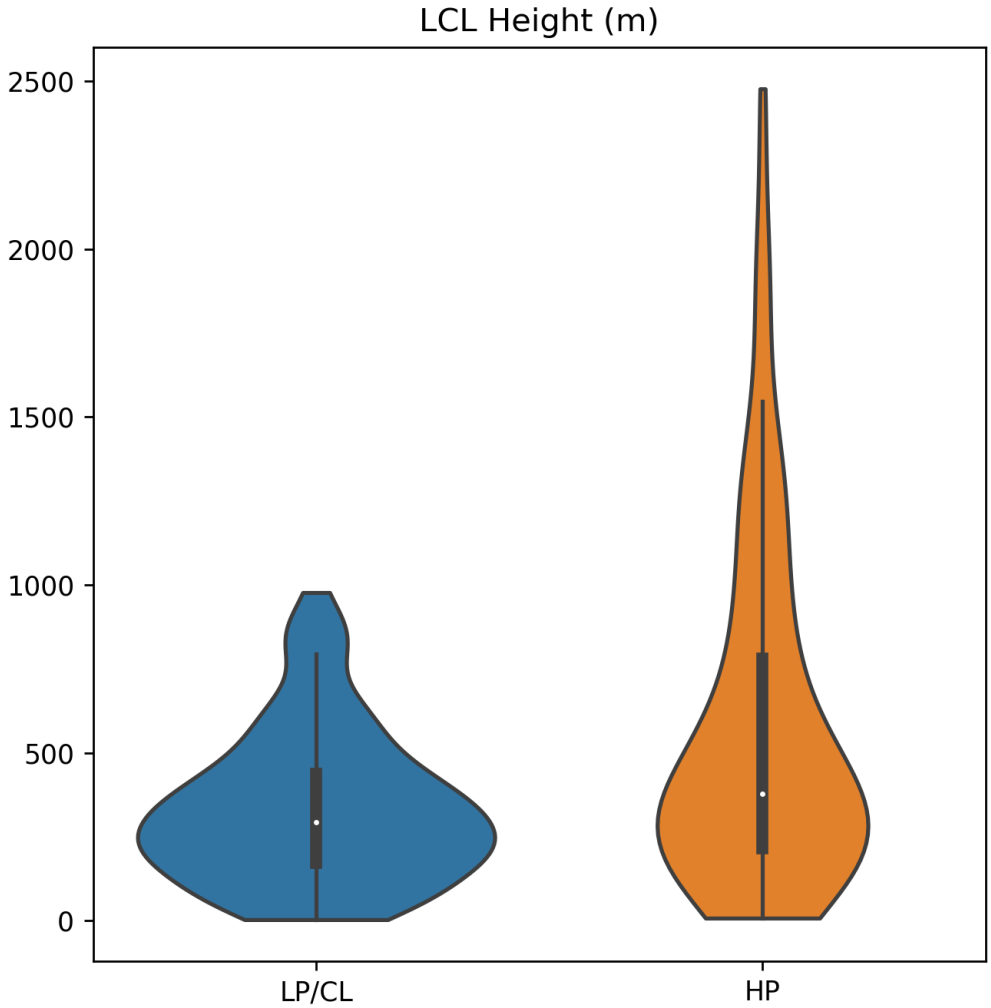

T-Statistic: -5.94, P-Value: 7.41e-09
KS-Statistic: 0.223, P-Value: 0.000682
CL Normality T-Stat: 19.2, P-Value: 6.92e-05
HP Normality T-Stat: 25.2, P-Value: 3.41e-06
LP/CL --> Median: 294.0, 25th: 171.0, 75th: 438.0, IQR: 267.0
HP --> Median: 379.0, 25th: 215.0, 75th: 780.0, IQR: 566.0

Figure 43 – Same as in figure 41, but for LCL Height.

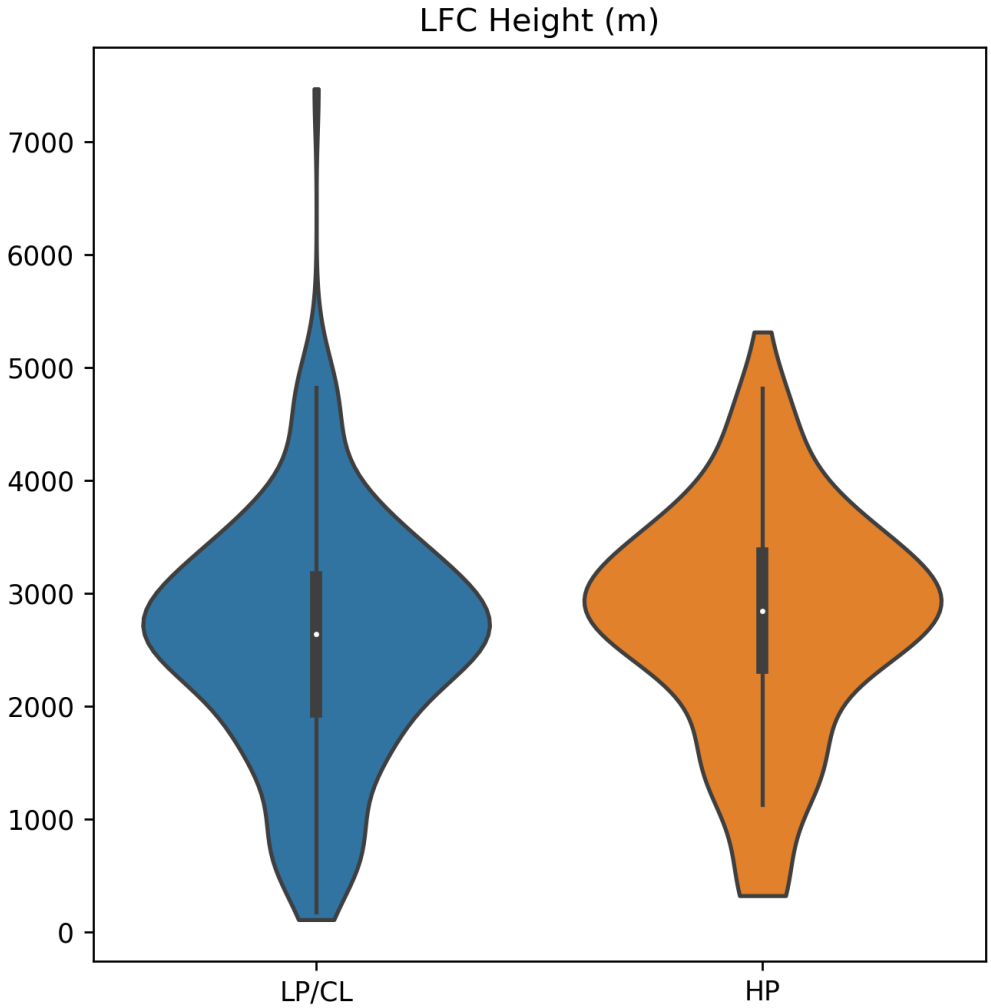

T-Statistic: -1.4, P-Value: 0.162
KS-Statistic: 0.137, P-Value: 0.094
CL Normality T-Stat: 3.91, P-Value: 0.142
HP Normality T-Stat: 0.765, P-Value: 0.682
LP/CL --> Median: 2640.0, 25th: 1950.0, 75th: 3140.0, IQR: 1190.0
HP --> Median: 2840.0, 25th: 2340.0, 75th: 3350.0, IQR: 1010.0

Figure 44 – Same as in figure 41, but for LFC Height.

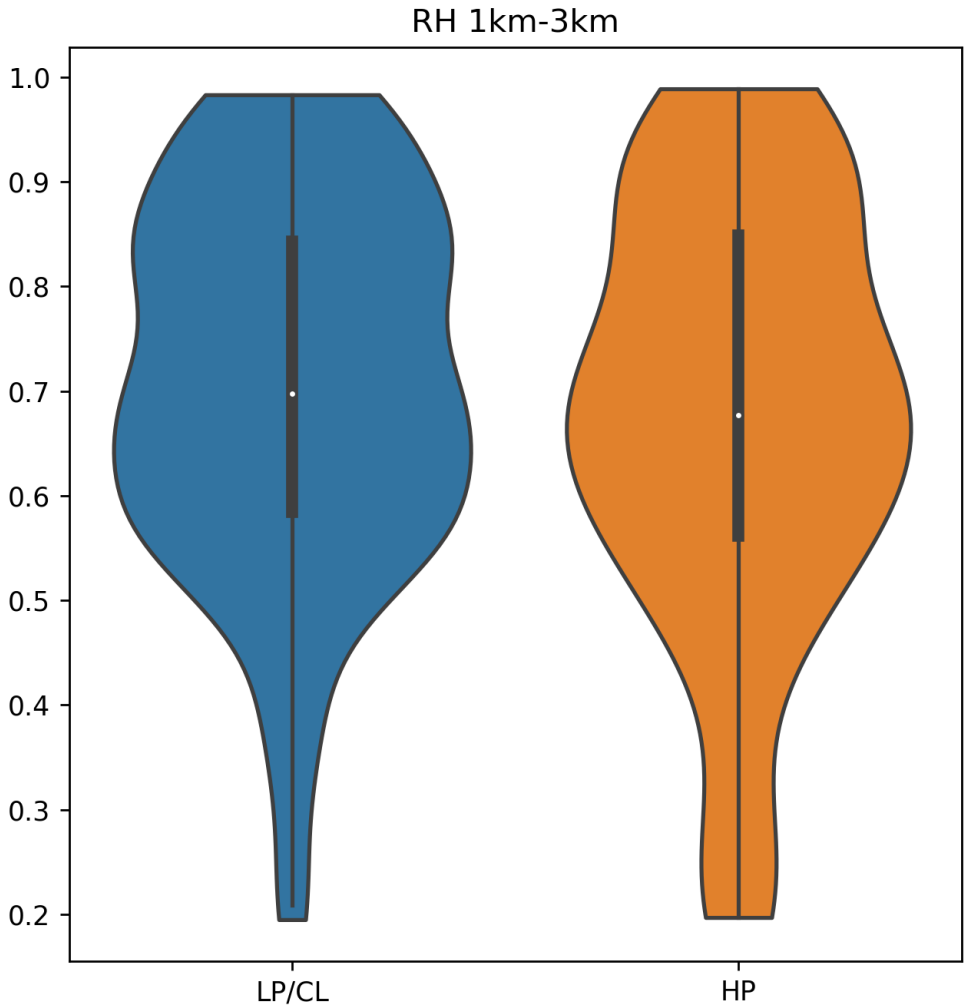

T-Statistic: 1.46, P-Value: 0.145
KS-Statistic: 0.0924, P-Value: 0.484
CL Normality T-Stat: 2.11, P-Value: 0.348
HP Normality T-Stat: 2.48, P-Value: 0.29
LP/CL --> Median: 0.697, 25th: 0.585, 75th: 0.843, IQR: 0.258
HP --> Median: 0.677, 25th: 0.561, 75th: 0.849, IQR: 0.287

Figure 45 – Same as in figure 41, but for 1 – 3 km RH.

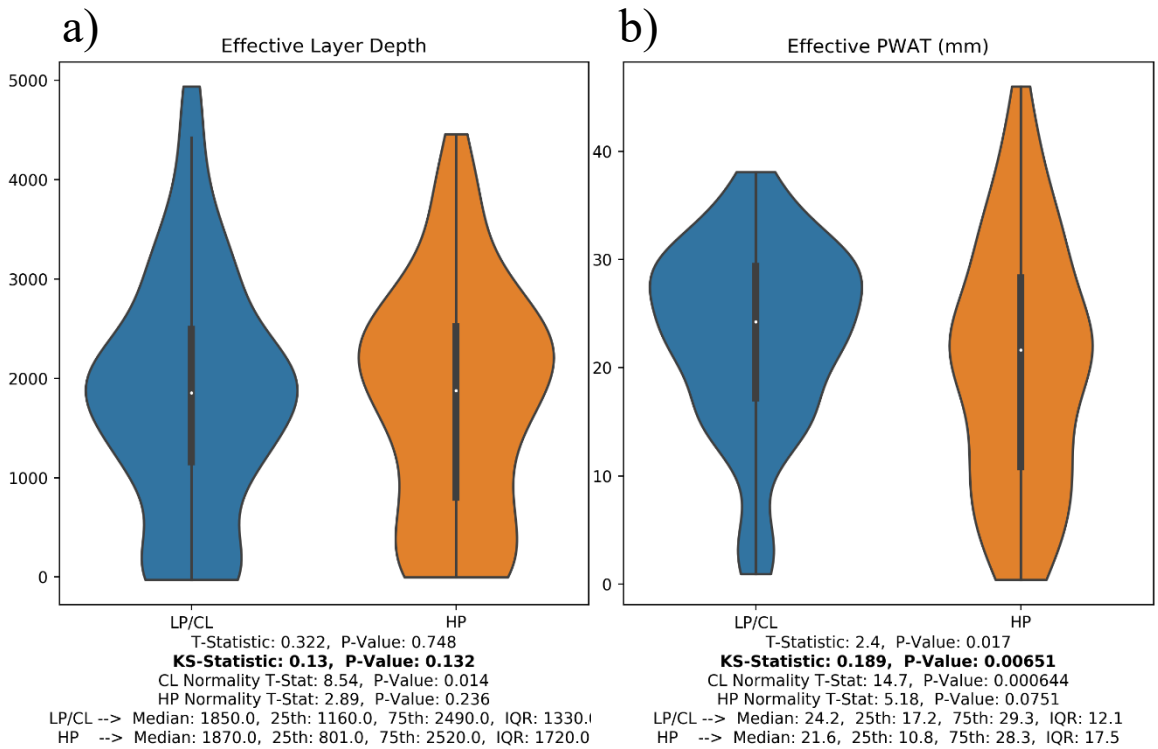

Figure 46 – Same as in figure 41, but for the effective layer depth (a) and the effective layer PWAT (b).

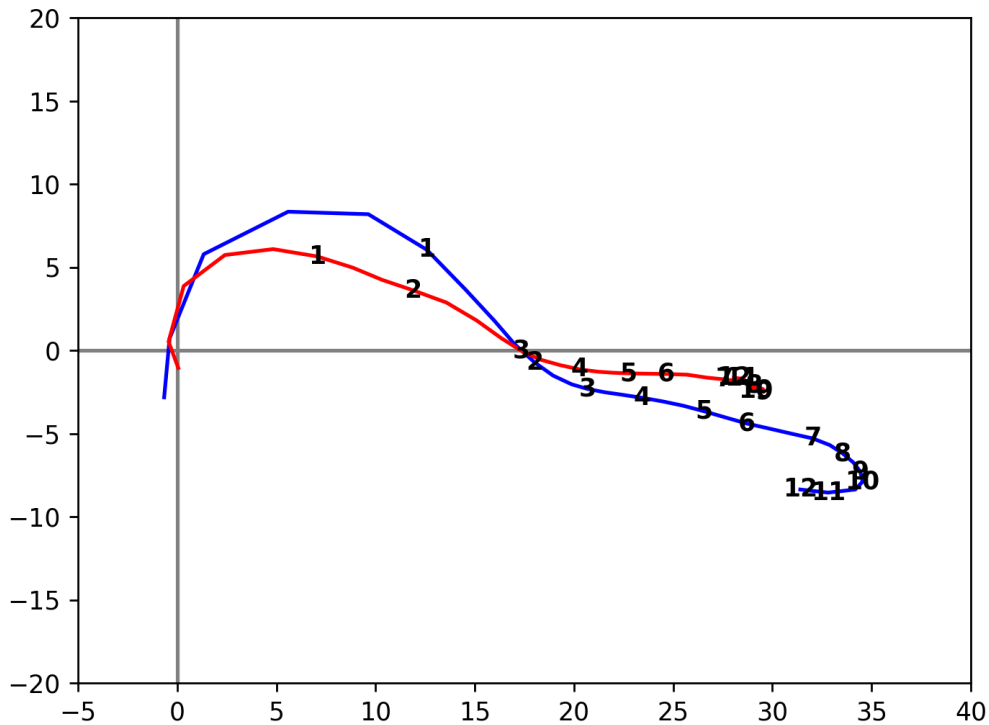

Figure 47 – Composite hodograph for LP/CL and HP storms, in blue and red, respectively. The numbers on the lines themselves represent the height of the observation AGL in kilometers. The x- and y-axes represent the u- and v-components of the storm relative winds rotated to the 0-4 km bulk shear vector, respectively and the winds have been shifted such that the average boundary layer wind is centered at the origin. This makes for a consistent comparison with Rasmussen and Straka (1998), their figure 9.

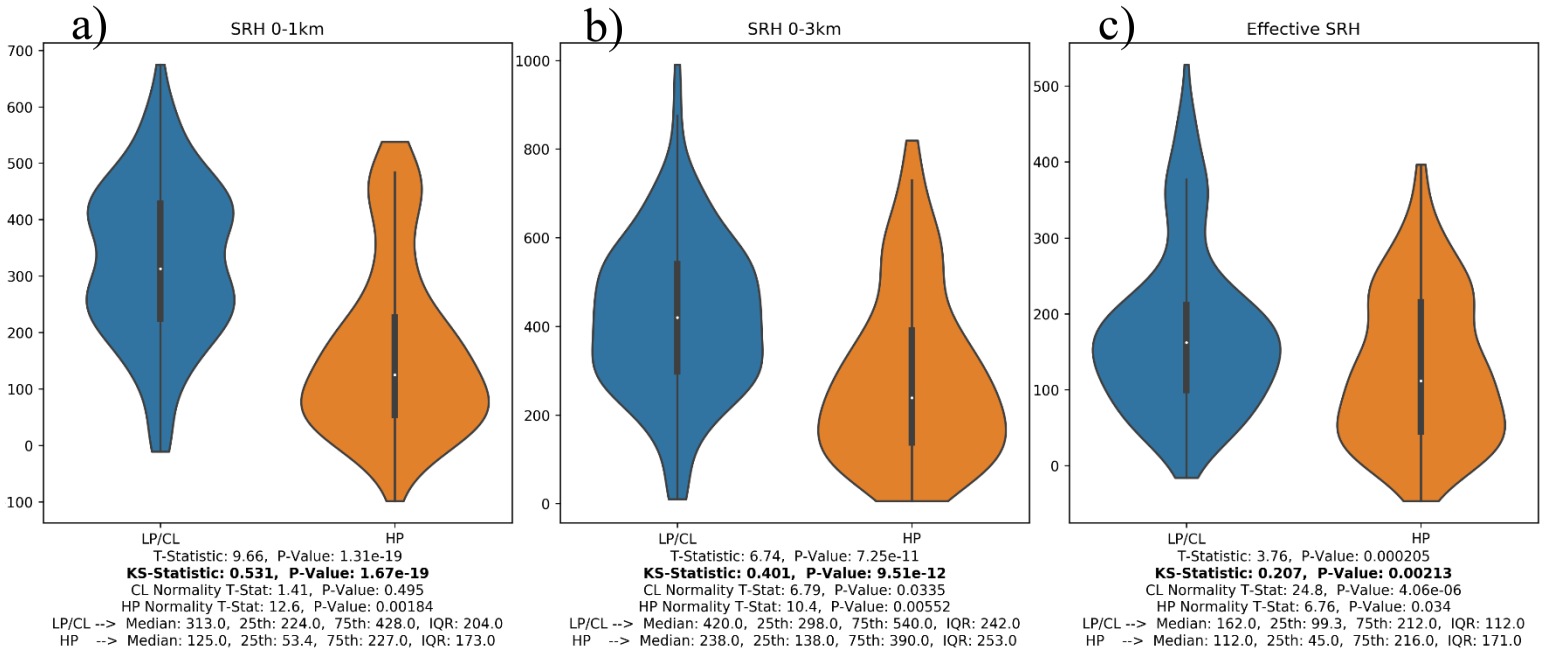

Figure 48 – Same as in figure 41, but for 0 – 1 km SRH (a), 0 – 3 km SRH (b) and effective layer SRH (c).

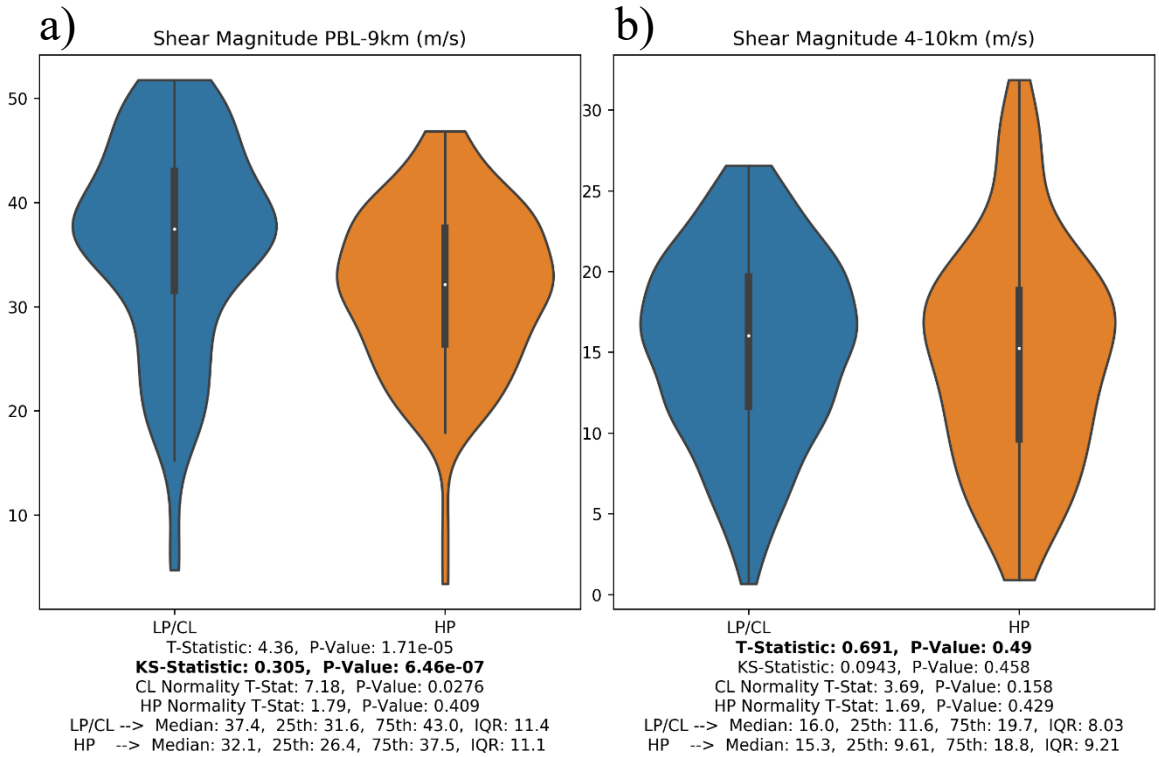

Figure 49 – Same as in figure 41, but for the bulk shear magnitude from the boundary layer to 9 km AGL (a) and the bulk shear magnitude from 4 km to 10 km AGL (b).

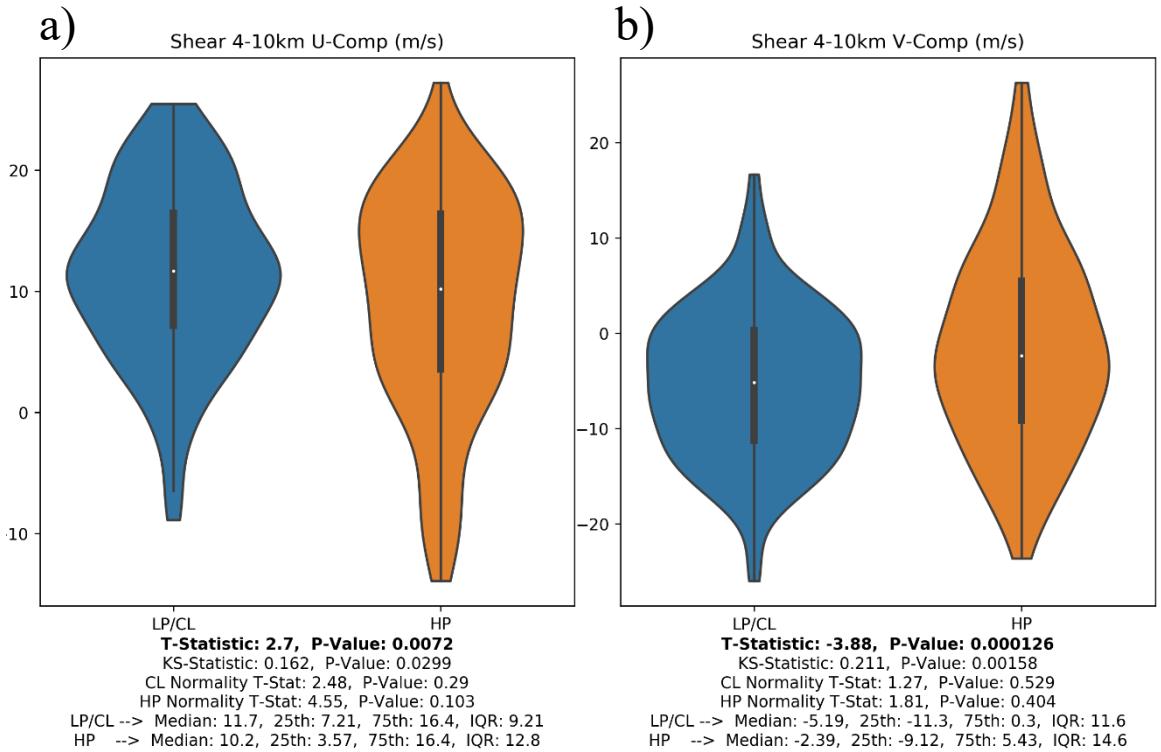

Figure 50 – Same as in figure 41, but for the u-component of the 4 – 10 km bulk shear vector (a) and the v--component of the 4 – 10 km bulk shear vector (b).

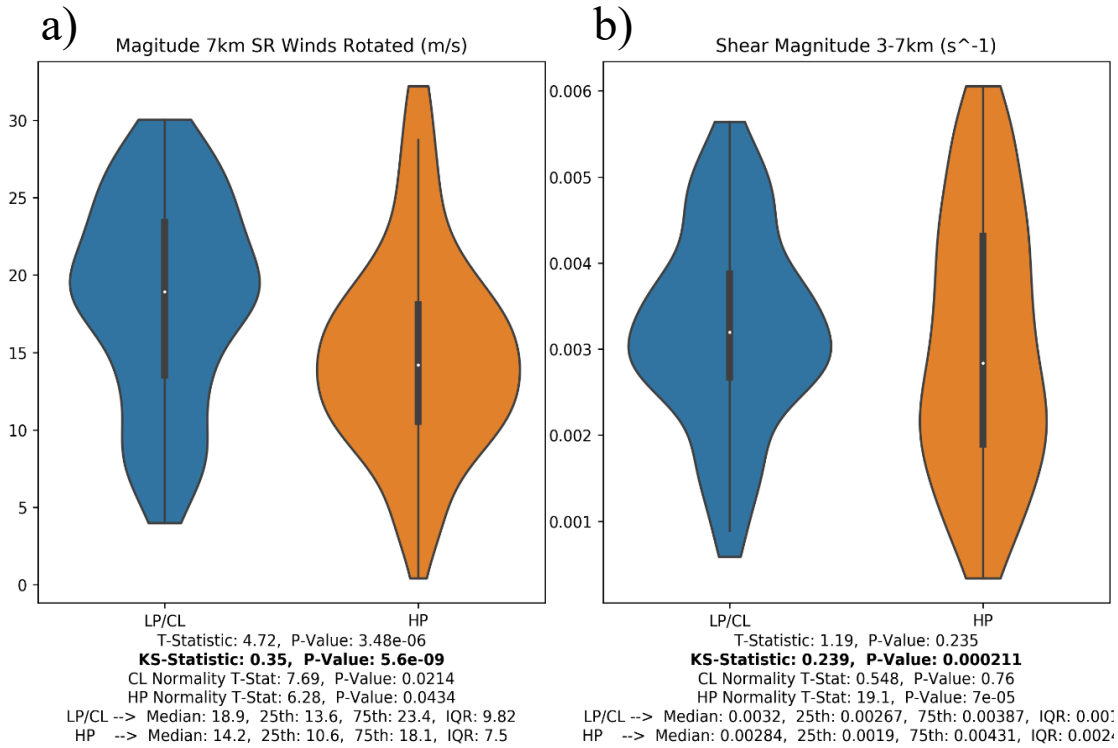

Figure 51 – Same as in figure 41, but for the storm relative winds at 7 km AGL (a) and the normalized bulk shear from 3 km – 7 km AGL (b).

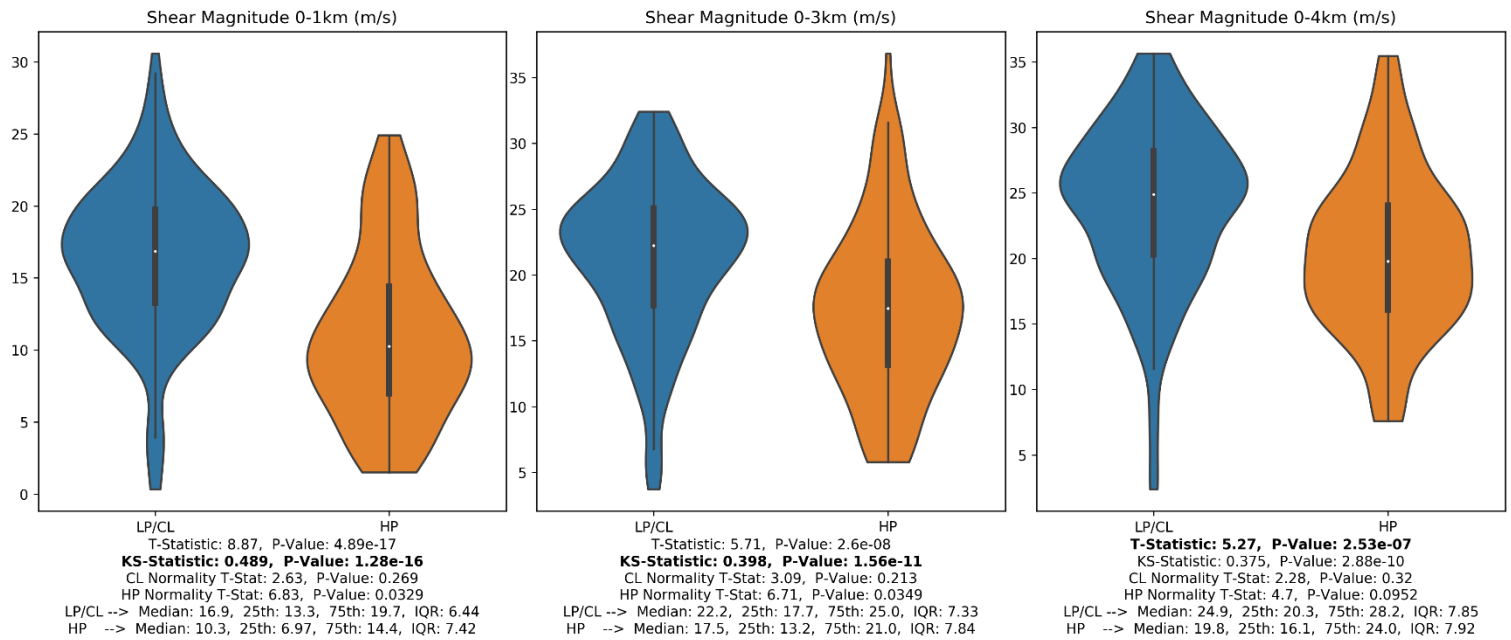

Figure 52 – Same as in figure 41, but (a) the 0 – 1 km bulk shear magnitude, (b) the 0 – 3 km bulk shear magnitude and (c) the 0 – 4 km bulk shear magnitude.

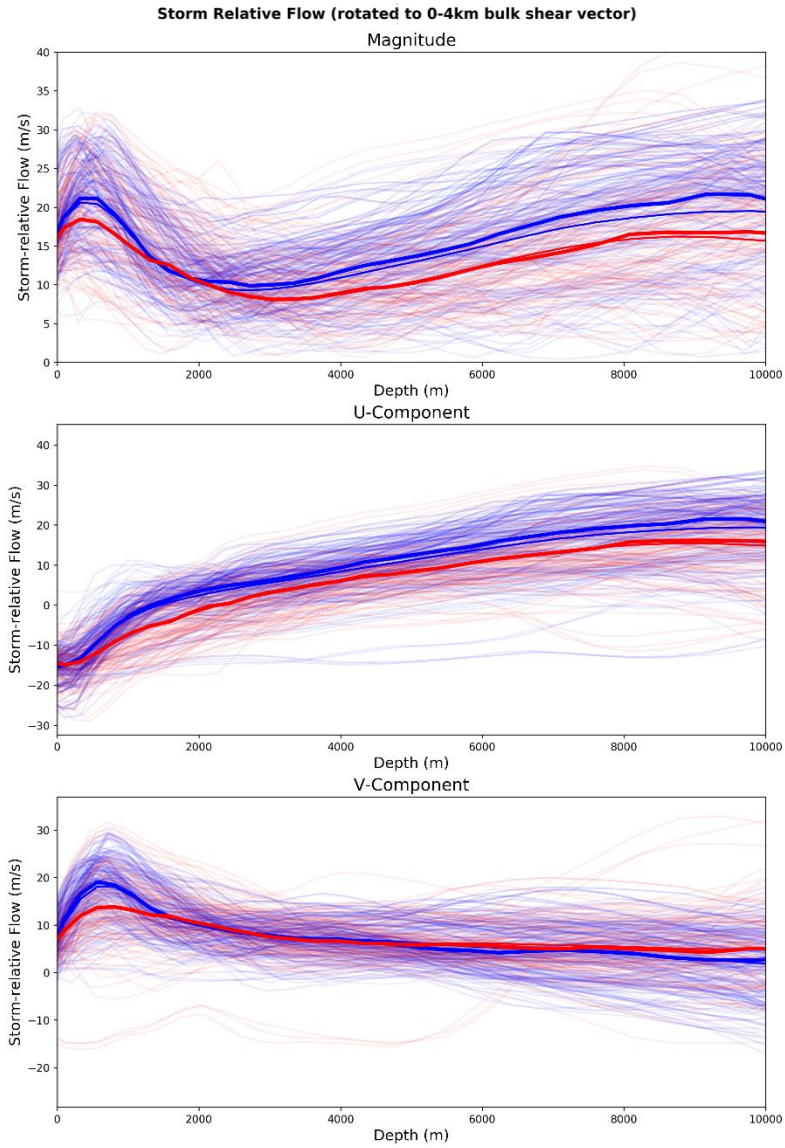

Figure 53 – The magnitude (top), u-component (middle) and v-component (bottom) of the storm relative flow, all of which have been rotated to the 0-4 km bulk shear vector. The x and y axes present the height (m) and wind speed (m/s), respectively. The blue lines represent the LP/CL archetypes and the red lines represent those of the HP archetype. The thinner and thicker bold lines represent the mean and median lines, respectively, for each group. The mean and median lines overlap with each other significantly making them hard to differentiate. The thin, semi-transparent lines represent each case.

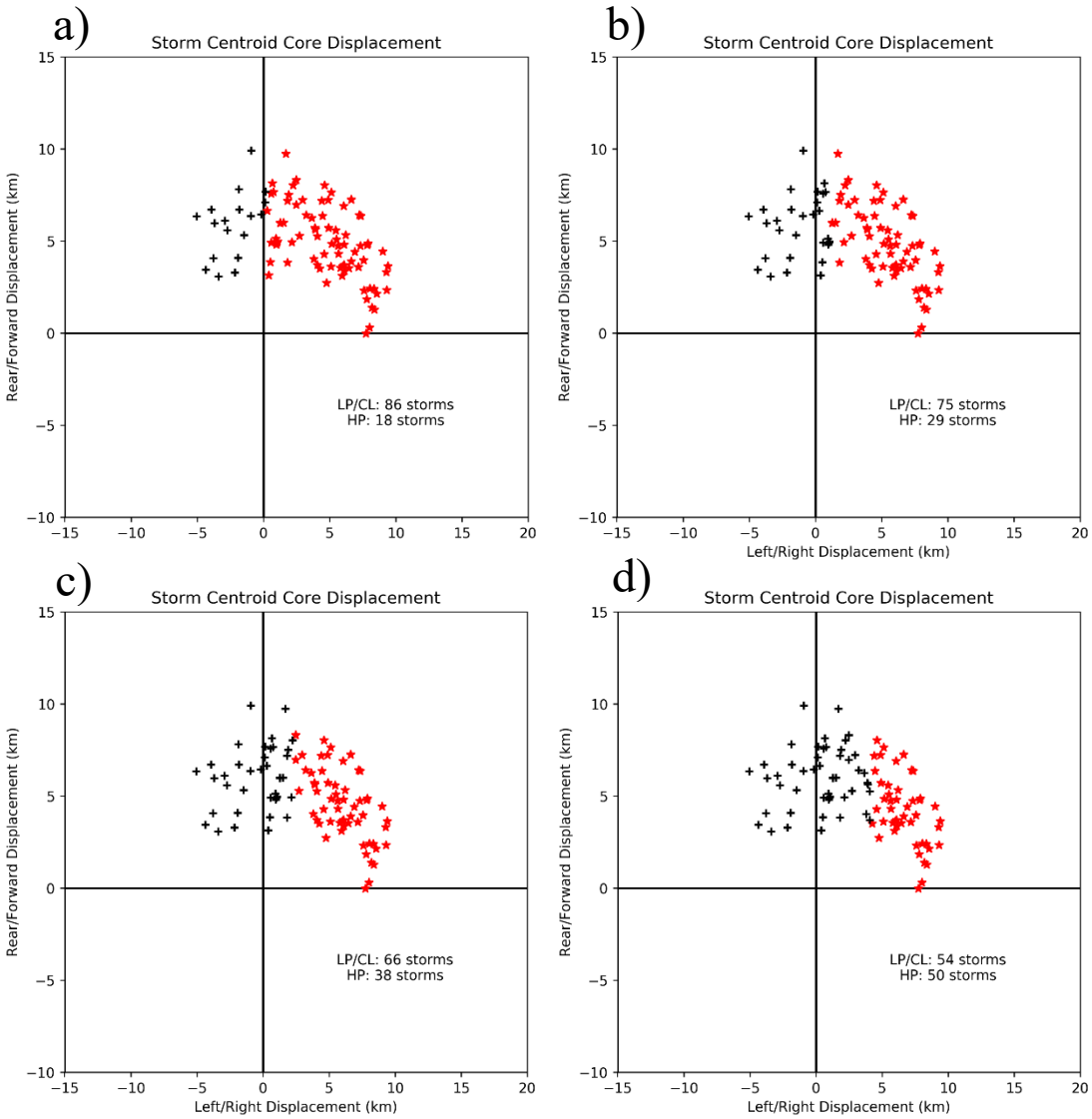

Figure 54 – The phase space diagrams for each of the shifts of in the threshold between LP/CL and HP storms as compared to the current threshold (c). The minus 2 (a), minus 1 (b) and plus 2 (d) graphics are shown for comparison. In addition, the sample size for each grouping is annotated on each graphic.

CHAPTER V: SUMMARY AND FUTURE WORK

The primary goal of this study is to provide additional observations of supercell environments across the precipitation spectrum with the aid of a new identification algorithm to determine observational differences among LP, CL and HP supercells. In addition, this study also moved towards adding more unique features of LP/CL and HP storms with some unique comparisons of its own (e.g., inflow layer PWAT, components of 4-10 km shear vector). Through a similar method to that of Beatty et al.'s (2009) tracking of supercells, this study was able to be completed semi-objectively with the only subjectivity being represented in training the algorithm as to which storms fell in which precipitation category (LP/CL or HP). Even though there were some unique differences in the two tracking algorithms, they ultimately produced consistent results. In addition, the sensitivity of the tracking algorithm was examined and no significant difference in the results was found within 1 km of the threshold used for analysis. The synoptic environment for each precipitation category was also scrutinized, with significant differences present that helped to provide context for the inflow environment results. Accordingly, there were notable variations in thermodynamic and kinematic aspects of LP/CL and HP supercell environment and will be summarized below.

a) Synoptic Environment and Climatology

The synoptic environment held the key to describing many of the differences that accrued in the inflow environments for each of the supercell groups. It was evident that LP/CL storms generally found themselves in much stronger synoptically forced environments when compared to HP storms that generally lacked strong synoptic forcing.

In addition, LP/CL storms were identified with strong trough/ridge systems and meridional flow whereas HP storms preferred a more zonal flow pattern. The identification of these distinct differences will help in the forecasting world in determining not only which type of supercell is generally favored but what the primary hazards for a given day will be.

b) Thermodynamic Comparisons

As shown in the previous chapter, tested was the total PWAT, multiple forms of CAPE (i.e., MUCAPE, MLCAPE, SBCAPE), the LCL and LFC heights, low-level RH and the inflow layer PWAT (Figs. 41 – 46). While all but the LFC height and low-level RH were found to vary significantly among the different archetypes, the results in the present study were at times at odds with previous studies.

For the total PWAT (Fig. 41), the KS-test indicated that the distributions were significantly different; however, further examination of the lower, middle and upper quartile suggested that PWAT does not vary much between the archetypes. This physically made sense looking at the similarity in the moisture profiles of the composite skew-t diagrams. This finding, however, differed from both Bluestein and Parks (1983) and Rasmussen and Straka (1998). Bluestein and Parks (1983) found LP storms to have significantly lower PWAT than other supercells and Rasmussen and Straka (1998) found only HP storms to have significantly higher PWAT than both LP and CL storms. Since both Bluestein and Parks (1983) and Rasmussen and Straka (1998) used similar conventions to determine an appropriate sounding for the given storm, this could explain the lack of consistency here. These studies used the closest observed sounding that fell within 3

hours of the mature phase of the supercell and they altered the surface observation to fit that of a nearby environment, both of which were in the same airmass as the given supercell. Even with this constraint, there can still be changes to the moisture, temperature and kinematic profiles over this timeframe (e.g., Parker 2014), resulting in the profiles being less representative.

The multiple forms of CAPE (Fig. 42) tested all suggested that LP/CL storms exhibit significant higher CAPE than HP storms. It was identified that temporal differences in the occurrence of LP/CL and HP storms can help explain the difference found among archetypes. This result was at odds with the Bluestein and Parks (1983) study but was consistent with Rasmussen and Straka (1998).

Regarding the LCL and LFC height (Figs. 43 – 44), they were found to have significant and insignificant differences, respectively. Given the fact that CL storms in particular are more prolific in the production of tornadoes, it makes sense that the LP/CL grouping here lent itself to significantly lower LCL heights. The nearly similar LFC heights between LP/CL and HP storms generally lacked a physical explanation. As a result, the finding with LCL height found relative consistency with Rasmussen and Straka (1998) and the finding with the LFC height lack consistency with Rasmussen and Straka's (1998) study. Again the lack of consistency could relate to sounding selection methods from Rasmussen and Straka (1998) who used hourly surface observations that were in the same airmass of the storm to compute variables such as the LCL and LFC heights, which defines a very different method that what was adhered to in this study.

RH between 1 and 3 km (Fig. 45) was calculated to compare to the McCaul and Cohen (2002) and Grant and Van Den Heever (2014) studies. However, the distributions of low-level RH were statistically similar among the two supercell groups. While it physically makes sense that a drier environment near the surface would increase entrainment and thus lower the upward mass flux, it was concluded that other variables, which were held constant in both of the above studies could help to mask and affects that would have been caused by a change in low-level moisture.

Finally, the effective layer PWAT (Fig. 46) was calculated and suggested that LP/CL storms had exhibited higher values throughout this layer than HP storms. Even though the depth of the effective layer was nearly the same for each archetype, an effective layer that began closer to the ground would likely result in higher PWAT values than say the convection was elevated as is generally the case for nocturnal storms.

c) Kinematic Comparisons

As evident in the composite hodographs (Fig. 47), there were significant differences between LP/CL and HP supercells, which translated to numerous significantly different shear and SRH parameters.

One of the first clear differences in the composite hodographs illustrated that LP/CL storms were associated with veering above 7 km, in line with the Warren et al. (2017) modeling study, but in contrast to Rasmussen and Straka (1998). It was shown in Warren et al. (2017) that veering winds aloft were associated with an elongation of the updraft and thus the precipitation shield towards the northwest in their simulation. Backing winds on the other hand showed a more circular updraft with heavy precipitation

concentrated in the rear-flank of the storm (e.g., HP supercell). These differing results here can be attributed to the fact that Warren et al. (2017) only used a single thermodynamic profile, which was shown to have differed between precipitation archetypes, especially the mid-level moisture as shown in Fig. 40. In addition, the Rasmussen and Straka (1998) study only used 0000 UTC soundings that were within 3 hours of the mature stage of the storm of interest. Although one could argue that the upper-levels don't vastly change over this timeframe, the upper-level flow relative to the storm can indeed differ vastly over the timeframe of 3 hours.

In the low-levels (i.e. 0 – 1 km, 0 – 3 km, 0 – 4 km), bulk shear vectors and SRH (Figs. 52, 48, respectively) of LP/CL storms were significantly higher than HP storms. Since SRH accounts for storm motion, the faster storm motion observed in LP/CL supercells is physically consistent with this result. Furthermore, this result is consistent with the stronger synoptic scale forcing present for LP/CL supercells (Figs. 37 – 39).

Deep-layer (i.e., PBL – 9 km, 4 – 10 km) shear vector magnitudes (Fig. 49) were key in differentiating supercell precipitation archetypes; for example, Rasmussen and Straka (1998) found a significant inverse relationship, where a decrease in surface precipitation was directly related to larger magnitudes of deep layer shear. The present study had a similar finding for the PBL – 9 km layer. However, for the 4 – 10 km bulk shear magnitude, it was deduced from the composite hodograph (Fig. 47) that most of the shear accrued in the low-levels, generally below 4 km AGL (Fig. 52c) and that shear in the 4 – 10 km range was generally similar between the archetypes (Fig. 49b).

The Brooks et al. (1993) modeling study identified the importance of both the magnitude of the 7 km AGL wind as well as the 3 – 7 km shear (Fig. 51). The 7 km AGL wind was found to be significantly higher among LP/CL storms in this study, consistent with the stronger synoptic scale forcing. This supports the hypothesis drawn in the Rasmussen and Straka (1998) study that increased upper level flow lends itself to more transportation of hydrometeors downstream and away from the updraft. However, the 3 – 7 km shear was not found to have a significant effect on the precipitation structure of supercells.

Lastly, examining the storm-relative wind profile (Fig. 53) demonstrates that LP/CL storms tend to have a stronger flow magnitude. In addition, the weakest storm relative winds occur closer to the surface for LP/CL storms and the maximum in meridional flow, while occurring at the same altitude for both groups, is much higher for LP/CL storms. Additionally, stronger storm-relative flow in the upper-levels is associated with LP/CL storms making this finding consistent with Rasmussen and Straka (1998).

As shown, both thermodynamic and kinematic profiles are important in the determination of supercell precipitation structure. Thermodynamic variables such as CAPE, LCL height and the moisture profile help to explain which storms are more likely to form. Lower CAPE suggests a more HP-like storm, which could be attributed to time of day distinctions between the groups. The lower LCL height for the LP/CL group helps to provide insight as to why particularly CL storms are more likely to produce tornadoes. The slightly drier mid-level moisture profile associated with HP storms helps to explain their most prevalent severe attribute, strong straight-line winds. Kinematic variables such as

the low-level shear as well as the upper tropospheric flow helped to define significant differences between the archetypes. Stronger low-level shear associated itself with LP/CL storms mainly due to the stronger synoptic environment that was associated with these storms. The backing vs. veering discussion deduced from Rasmussen and Straka (1998) and Warren et al. (2017) in determining supercell archetype leaned towards the Warren et al. (2017) modeling study as it was determined here that a veering profile in the upper troposphere was associated with LP/CL storms. Overall there are many distinguishing factors between LP, CL and HP storms, but understanding the right combination of these factors in crucial in determining not only the precipitation structure of these storms, but also the associated hazards that are likely to follow suit with the expected storms.

d) Future Work

Although the dataset used herein has doubled that of any other prior studies thanks to the use of a semi-objective tracking algorithm, it can still be further expanded. The nature tracking algorithm makes it easy to expand on the dataset. Thus, increasing the number of storms tracked will further add to the robustness of the results.

Another goal for future work is to consider each hour of the supercell's life separately as the evolution of supercells has been documented. Looking into the supercells in more of an evolutionary standpoint will help to open environmental characteristics that may play a role into how a storm may have evolved. The current standpoint on this is that the supercell had a predominate structure over its lifetime and was analyzed as such.

This study has also only taken minor steps in mitigating convective contamination associated with near-storm inflow environments. The current measure in place includes looking for precipitation in the model at the specified grid point. Other measures such as looking for a cold pool or seeing if the entire or majority of the profile is saturated, indicating a thick layer of clouds, etc.

Finally, it would also be useful to conduct additional modeling studies to further understand the processes leading to the differences between precipitation archetypes. For example, testing a wider variety of thermodynamic environments and microphysics schemes would be a logical path forward to expand the work of Warren et al. (2017) and determine if that approach would produce results more consistent with the observations.

REFERENCES

Achtemeier, G. L., 1969: Some observations of splitting thunderstorms over Iowa on August 25-26, 1965. Department of Meteorology, Florida State University.

Beatty, K., E. Rasmussen, and J. Straka, 2008: The supercell spectrum. Part I: A review of research related to supercell precipitation morphology. E-Journal of Severe Storms Meteorology, 3.

Beatty, K., E. Rasmussen, J. Straka, and L. Lemon, 2009: The supercell spectrum. Part II: A semi-objective method for radar classification of supercell type. E-Journal of Severe Storms Meteorology, 4.

Bluestein, H. B., and C. R. Parks, 1983: A synoptic and photographic climatology of low-precipitation severe thunderstorms in the southern plains. Monthly weather review, 111, 2034-2046.

Bluestein, H. B., and G. R. Woodall, 1990: Doppler-radar analysis of a low-precipitation severe storm. Monthly weather review, 118, 1640-1665.

Bothwell, P., J. Hart, and R. Thompson, 2002: An integrated three-dimensional objective analysis scheme in use at the Storm Prediction Center. CONFERENCE ON WEATHER ANALYSIS AND FORECASTING, AMS, J117-J120.

Brandes, E. A., 1978: Mesocyclone evolution and tornadogenesis: Some observations. Monthly Weather Review, 106, 995-1011.

Brooks, H. E., C. A. D. III, and R. B. Wilhelmson, 1994: The Role of Midtropospheric Winds in the Evolution and Maintenance of Low-Level Mesocyclones. Monthly Weather Review, 122, 126-136.

Browning, K. A., 1964: Airflow and precipitation trajectories within severe local storms which travel to the right of the winds. Journal of the Atmospheric Sciences, 21, 634-639.

Browning, K., 1977: The structure and mechanisms of hailstorms. Hail: A review of hail science and hail suppression, Springer, 1-47.

Burgess, D., and R. Davies-Jones, 1979: Unusual tornadic storms in eastern Oklahoma on 5 December 1975. Monthly Weather Review, 107, 451-457.

Burgess, D. W., V. T. Wood, and R. A. Brown, 1982: Mesocyclone evolution statistics. Preprints, 12th Conf. on Severe Local Storms, San Antonio, TX, Amer. Meteor. Soc., 422–424

Copernicus Climate Change Service (C3S) (2017): ERA5: Fifth generation of ECMWF atmospheric reanalyses of the global climate. Copernicus Climate Change Service Climate Data Store (CDS), January 2020. https://cds.climate.copernicus.eu/cdsapp#!/home

Cohen, C., 2000: A quantitative investigation of entrainment and detrainment in numerically simulated cumulonimbus clouds. Journal of the atmospheric sciences, 57, 1657-1674.

Davies-Jones, R., 1984: Streamwise Vorticity: The Origin of Updraft Rotation in Supercell Storms. Journal of the Atmospheric Sciences, 41, 2991-3006.

Doswell III, C., A. Moller, and R. Przybylinski, 1990: A unified set of conceptual models for variations on the supercell theme. Preprints, 16th Conf. on Severe Local Storms, Kananaskis Park, AB, Canada, Amer. Meteor. Soc, 40-45.

Doswell, C. A., and D. W. Burgess, 1993: Tornadoes and tornadic storms: A review of conceptual models. Geophysical Monograph-American Geophysical Union, 79, 161-161.

Fankhauser, J. C., 1971: Thunderstorm-environment interactions determined from aircraft and radar observations. Mon. Wea. Rev, 99, 171-192.

Foote, G., and J. Fankhauser, 1973: Airflow and moisture budget beneath a northeast Colorado hailstorm. Journal of Applied Meteorology, 12, 1330-1353.

Fujita, T., and H. Grandoso, 1968: Split of a thunderstorm into anticyclonic and cyclonic storms and their motion as determined from numerical model experiments. Journal of the Atmospheric Sciences, 25, 416-439.

Gallus Jr, W. A., N. A. Snook, and E. V. Johnson, 2008: Spring and summer severe weather reports over the Midwest as a function of convective mode: A preliminary study. Weather and Forecasting, 23, 101-113.

Gilmore, M.S. and L.J. Wicker, 1998: The Influence of Midtropospheric Dryness on Supercell Morphology and Evolution. Mon. Wea. Rev., 126, 943–958.

Grant, L. D., and S. C. Van Den Heever, 2014: Microphysical and dynamical characteristics of low-precipitation and classic supercells. Journal of the Atmospheric Sciences, 71, 2604-2624.

Hersbach, H., and D. Dee, 2016: ERA5 reanalysis is in production. *ECMWF newsletter*, **147,** 5-6.

Honda, T., and T. Kawano, 2015: How does mid-tropospheric dry air affect the evolution of supercellular convection? Atmospheric Research, 157, 1-16.

James, R.P. and P.M. Markowski, 2010: A Numerical Investigation of the Effects of Dry Air Aloft on Deep Convection. Mon. Wea. Rev., 138, 140–161.

Johnson, J., P. L. MacKeen, A. Witt, E. D. W. Mitchell, G. J. Stumpf, M. D. Eilts, and K. W. Thomas, 1998: The storm cell identification and tracking algorithm: An enhanced WSR-88D algorithm. Weather and forecasting, 13, 263-276.

Klemp, J. B., 1987: Dynamics of tornadic thunderstorms. Annual review of fluid mechanics, 19, 369-402.

Knight, C. A., and L. Miller, 1993: First radar echoes from cumulus clouds. Bulletin of the American Meteorological Society, 74, 179-188.

Lemon, L. R., 1977: New Severe Thunderstorm Radar Identification Techniques and Warning Criteria.

Lemon, L. R., and C. A. Doswell III, 1979: Severe thunderstorm evolution and mesocyclone structure as related to tornadogenesis. Monthly Weather Review, 107, 1184-1197.

Lemon, L., and D. Burgess, 1993: Supercell associated deep convergence zone revealed by a WSR-88D. Preprints, 26th International Conf. on Radar Meteorology, Norman, OK, Amer. Meteor. Soc, 206-208.

Lemon, L. R., S. Parker, and N. North Platte, 1996: P1. 6 THE LAHOMA STORM DEEP CONVERGENCE ZONE: ITS CHARACTERISTICS AND ROLE IN STORM DYNAMICS AND SEVERITY.

McCaul Jr, E. W., and C. Cohen, 2002: The impact on simulated storm structure and intensity of variations in the mixed layer and moist layer depths. Monthly weather review, 130, 1722-1748.

Moller, A. R., C. A. Doswell III, M. P. Foster, and G. R. Woodall, 1994: The operational recognition of supercell thunderstorm environments and storm structures. Weather and Forecasting, 9, 327-347.

MunichRe, 2017: TOPICS Geo Natural catastrophes 2017.

Newton, C. W., and S. Katz, 1958: Movement of large convective rainstorms in relation to winds aloft. Bulletin of the American Meteorological Society, 39, 129-136.

NOAA National Weather Service (NWS) Radar Operations Center (1991): NOAA Next Generation Radar (NEXRAD) Level 2 Base Data. NOAA National Centers for Environmental Information. doi:10.7289/V5W9574V.

Oliphant, T. E., 2007: Python for Scientific Computing. *Computing in Science & Engineering*, **9,** 10-20.

Parker, M. D., 2014: Composite VORTEX2 Supercell Environments from Near-Storm Soundings. Monthly Weather Review, 142, 508-529.

Potvin, C. K., K. L. Elmore, and S. J. Weiss, 2010: Assessing the Impacts of Proximity Sounding Criteria on the Climatology of Significant Tornado Environments. Weather and Forecasting, 25, 921-930.

Rasmussen, E.N., and D.O. Blanchard, 1998: A Baseline Climatology of Sounding-Derived Supercell and Tornado Forecast Parameters. Wea. Forecasting, 13, 1148–1164

Rasmussen, E. N., and J. M. Straka, 1998: Variations in supercell morphology. Part I: Observations of the role of upper-level storm-relative flow. Monthly weather review, 126, 2406-2421.

Rotunno, R., and J. Klemp, 1985: On the rotation and propagation of simulated supercell thunderstorms. Journal of the Atmospheric Sciences, 42, 271-292.

Stumpf, G. J., and Coauthors, 1998: The National Severe Storms Laboratory mesocyclone detection algorithm for the WSR-88D. Weather and Forecasting, 13, 304-326.

Thompson, R. L., R. Edwards, J. A. Hart, K. L. Elmore, and P. M. Markowski, 2003: Close proximity soundings within supercell environments obtained from the Rapid Update Cycle. Wea. Forecasting, 18, 1243–1261

Thompson, R. L., B. T. Smith, J. S. Grams, A. R. Dean, and C. Broyles, 2012: Convective modes for significant severe thunderstorms in the contiguous United States. Part

II: Supercell and QLCS tornado environments. Weather and forecasting, 27, 1136-1154.

Vieux, B. E., and P. B. Bedient, 1998: Estimation of rainfall for flood prediction from WSR-88D reflectivity: A case study, 17–18 October 1994. Weather and Forecasting, 13, 407-415.

Warren, R. A., H. Richter, H. A. Ramsay, S. T. Siems, and M. J. Manton, 2017: Impact of variations in upper-level shear on simulated supercells. Monthly Weather Review, 145, 2659-2681.

Wilhelmson, R., 1974: The life cycle of a thunderstorm in three dimensions. Journal of the Atmospheric Sciences, 31, 1629-1651.